The Pennsylvania State University

The Graduate School

# IMAGING ELASTODYNAMIC AND HYDRAULIC PROPERTIES OF FRACTURED ROCK: EXPLORING EFFECTS OF DYNAMIC STRESSING, SHEARING, FRACTURE APERTURE, AND ROUGHNESS

A Dissertation in

Geosciences

by

Clay Emerson Wood

© 2024 Clay Emerson Wood

Submitted in Partial Fulfillment
of the Requirements
for the Degree of

Doctor of Philosophy

May 2024

The dissertation of Clay Emerson Wood was reviewed and approved by the following:

Chris Marone

Professor of Geosciences

Thesis Advisor

Chair of Committee

Parisa Shokouhi

Professor of Engineering Science and Mechanics

Thesis Co-Advisor

Derek Elsworth

Professor of Energy and Mineral Engineering

Tieyuan Zhu

Professor of Geosciences

Donald Fisher

Professor of Geosciences

Program Head

# Abstract

Dynamic perturbations in the subsurface, originating from natural or industrial sources, are associated with observations of changes in poro-elastic properties that have far-ranging effects. Broadly, there are "strain-induced" and "fluid-induced" sources of these subsurface perturbations and, importantly, they produce coupled phenomenological observations. Many experimental and numerical studies that quantify elastic and hydraulic properties of rock, fractured (or "intact") under static stress conditions, however these measures are not necessarily indicative of their response during dynamic stress conditions. Motivated by these field observations, I use simultaneous continuous fluid flow and ultrasonic monitoring to quantify the elastic and permeability changes of natural and rough fractures. Furthermore, I incorporate measures of fracture topology and contact area to connect to the spatially variable ultrasonic monitoring and as inputs for multiphysics modeling of a single planar fracture.

In this dissertation, I ask fundamental questions surrounding the connection between fracture specific stiffness and fluid transport under a range of loading conditions and dynamic stressing. Moreover, I do so by performing complex experiments under triaxial stresses and use simultaneous continuous active-source ultrasonic monitoring and fluid flux measurements to measure the static and dynamic elastic and hydraulic properties of fractures. These unique experiments are also complemented by post-surface and topography characterization using pressure registering films and profilometry.

I begin this dissertation by introducing the problem statement broadly and providing some context for field-scale observations of dynamic stress-induced changes in the subsurface and lay out the limitation of linear elastic work within this context. In Chap-

ter 2, I use ultrasonic monitoring to image the spatial and elastic variability across an in-situ fractured rock specimen and relate these to fluid flow. These experiments produced complex results which highlights the variable nature of sheared fractured rock. In Chapters 3 and 4, I extend the work of Chapter 1 by focusing on the effect of stress state on dynamic stress-induced changes in flow and elasticity. Chapter 3 demonstrates the systematic reduction in nonlinear elasticity and permeability enhancement with increasing stress state, simulating depths. I additionally relate the real contact area from pressure sensitive films to the documented elastodynamic changes. Chapter 4 leverages the experimental results from Chapter 3 and utilizes high-resolution profilometry of the tensile fracture specimen as an input for multiphysics modeling. I demonstrate that perfectly matched fracture surfaces can reproduce some of the static fluid flow properties and that misalignment is highly influential on overall poro-elastic properties. Chapter 5 represents a focused study on the relation between roughness and granular in-fill of planar fractures and their influence on elastodynamic and hydraulic changes.

# Table of Contents

**List of Figures** viii

**List of Tables** xiii

**Acknowledgments** xiv

**Chapter 1**
**Introduction** 1

**Chapter 2**
**Imaging elastodynamic and hydraulic properties of in-situ fractured rock: An experimental investigation exploring effects of dynamic stressing and shearing** 5

2.1 Abstract . . . 5
2.2 Introduction . . . 6
2.3 Experimental Setup . . . 7
2.3.1 Experimental Procedure . . . 9
2.3.2 Permeability Measurements . . . 11
2.3.3 Ultrasonic Measurements: Active Source . . . 11
2.4 Results . . . 12
2.4.1 Nonlinear elastodynamic and hydraulic responses . . . 12
2.4.2 Dynamic Stress-induced Changes in Permeability and Wave Velocity 15
2.4.3 Spatial Variations of the Nonlinear Elastodynamic Response . . . 17
2.4.4 Wave Velocity Modulation . . . 18
2.4.5 Permeability and Wave Velocity Recovery from Dynamic Stressing 19
2.5 Discussion . . . 20
2.6 Conclusions . . . 23

**Chapter 3**
**Relating hydro-mechanical and elastodynamic properties of dynamically-stressed tensile-fractured rock in relation to applied normal stress, fracture aperture, and contact area** 40

3.1 Abstract . . . 40
3.2 Introduction . . . 41
3.3 Experimental Setup . . . 43
3.3.1 Experimental Procedure . . . 45
3.3.2 Steady-state Permeability Measurements . . . 46
3.3.3 Dynamic Permeability Measurements . . . 46

3.4 Active Source Ultrasonic Measurements . . . 47
3.4.1 Fresnel Zone Imaging . . . 48
3.5 Fracture Contact Characterization . . . 50
3.6 Results . . . 51
3.6.1 Static Hydraulic and Elastic Responses . . . 51
3.6.2 Connecting Sensor Footprint and Contact Area . . . 52
3.6.3 Hydraulic and Nonlinear Elastodynamic Responses . . . 53
3.6.4 Dynamic Stress-induced Changes in Permeability . . . 54
3.6.5 Dynamic Stress-induced Changes in P-wave Velocity . . . 55
3.6.6 Measurements During Loading vs. Unloading Phase . . . 56
3.6.7 Permeability Recovery and Slow Dynamics . . . 58
3.7 Discussion . . . 59
3.7.1 Elastic Deformation of Fracture and Bulk . . . 59
3.7.2 Linking Stress-Induced Elastodynamic and Hydraulic Changes . . . 61
3.7.3 Relating Contact Area to Elastodynamic Properties . . . 62
3.7.4 Broader Impacts and Insights . . . 64
3.8 Conclusion . . . 65

**Chapter 4**
**Multiphysics modeling of rough fracture deformation to constrain the connection between fracture stiffness, permeability, and acoustic transmission 84**
4.1 Abstract . . . 84
4.2 Introduction . . . 85
4.3 Methods . . . 86
4.3.1 Experiment . . . 86
4.3.2 Surface profilometry and digital alignment . . . 87
4.3.3 Elastic contact simulation . . . 88
4.3.4 Energy-based tilt refinement . . . 89
4.3.5 Fluid flow simulation . . . 90
4.4 Results . . . 91
4.4.1 Elastic deformation . . . 91
4.4.2 Fluid flow . . . 92
4.4.3 Comparing numerical and experimental fluid flow results . . . 92
4.4.4 Fracture Interface Stiffness and Contact Acoustic Nonlinearity . . . 93
4.5 Discussion . . . 96
4.5.1 Sensitivity to surface alignment/mating . . . 96
4.5.2 Effect of bulk elastic modulus . . . 97
4.5.3 Hydro-mechanical properties dependence on roughness . . . 98
4.6 Conclusion . . . 99

**Chapter 5**
**Poromechanics of particle remobilization and interface stiffness of dynamically stressed fractured rock** **110**
5.1 Abstract . . . 110
5.2 Introduction . . . 111
5.3 Experimental Setup . . . 113
5.3.1 Permeability Measurements . . . 115
5.4 Active Source Ultrasonic Measurements . . . 116
5.5 Results . . . 116
5.5.1 Hydraulic and Nonlinear Elastodynamic Responses . . . 117
5.5.2 Dynamic Stress-induced Changes . . . 118
5.5.3 Linking Static and Dynamic Poromechanical Measures . . . 119
5.6 Discussion . . . 120
5.7 Conclusion . . . 123

**Chapter 6**
**Conclusions and Future Work** **130**
6.1 Research Summary . . . 130

**Appendix A**
**Supplementary Information for Chapter 2** **134**

**Appendix B**
**Supplementary Information for Chapter 3** **146**

**Appendix C**
**Supplementary Information for Chapter 5** **151**

**Bibliography** **153**

# Chapter 1

## Introduction

## Introduction and Motivation

Dynamic perturbations in the subsurface, originating from natural or industrial sources, are associated with observations of changes in poro-elastic properties that have far-ranging effects. Broadly, there are "strain-induced" and "fluid-induced" sources of these subsurface perturbations and, importantly, they produce coupled phenomenological observations.

Injecting wastewater, carbon sequestration, and hydrocarbon recovery are critical activities that can perturb the local subsurface stress state and lead to damaged reservoir seals, accelerated deformation, fault reactivation (induced seismicity) [42, 70, 71, 88, 110, 111, 119]. A cascading effect of elastic waves propagating from earthquakes perturbing fault stability [9, 54, 99] and triggering seismicity [15, 117] may also manifest. These empirical observations are characterized by "elastic softening", or co-seismic velocity variation in the shallow crust [12–14, 25, 33, 46, 62, 63, 77, 122, 127]. This co-seismic softening, an instantaneous and transient wave speed change, is followed by a post-seismic recovery (in log-time) of the fractured rock elastic properties [12, 26, 48, 78].

These effects have been studied experimentally as well, and typically under shearing conditions [57]. Some of the experimental works are summarized by the following findings of the relation between acoustic transmission (wave speed and amplitude) and: gouge

layer dilation [56, 103], degree of surrounding bulk damage [108], evolution of contact area [133], and stress state [78]. In the work of [78], it was demonstrated that elastic stresses in bulk rock exert significant control on transmitted wave velocity and near-fault properties strongly influenced transmitted wave attenuation. All these experiments provide rich information about near- and far-fault elastic properties under different static loads or shear conditions, but this may not fully capture the dynamic strains (magnitude and frequency) observed on the field scale. Dynamic acousto-elastic testing (DAET) has recently been used to study the nonlinear *elastodynamic* response of different rock types and granular packs subject to various loading and saturation conditions. In these studies, a nonlinear elastic responses is induced with dynamic strains on the order of $10^{-6}$ [41, 93]. During such perturbations, the relationship between stress and strain is nonlinear. This nonlinear behavior of rock, intact or fractured, is modulated by and sensitive to minute features such as apertures (governing flow transport, asperity compliance), grain boundaries, and higher-order effects (impacted by rate and state-dependent friction and healing). Laboratory experiments implementing DAET [37, 41, 55,67,106,125,126], show a transient decrease in transmitted wave velocity in response to stress oscillations followed by a time logarithmic recovery, similar to the aforementioned field observations, especially [26, 48].

In the context of subsurface storage and energy recovery, dynamic perturbations in the subsurface manifest permeability changes, enhancement or reduction. Oscillations is pore pressure that are sufficiently large enough to change permeability can be induced by elastic waves from earthquakes [15, 66]. The underlying mechanism dominating empirical observations of permeability enhancement (and reduction) is postulated to be: (1) mobilizing and arresting of particles in porous media [20,21,30,64,95,96], (2) fracture geometry evolution (roughness, contact area, etc.) [1, 137], and (3) fracture orientation relative to flow direction [73]. The similar poro-elastic responses (permeability enhance-

ment and elastic softening) of faults and fractured rock to dynamic stressing sources demonstrate that these mechanisms – interface stiffness and fluid transport – are correlated [5–7, 17, 28, 35, 40, 47, 86, 124, 128, 137], much like the connection under static conditions [69, 75, 81, 84].

The important parameters to consider for the observations are the following: fracture contact area, roughness, and aperture [82]. These all modulate mechanical properties of fractures/faults via the stress distribution [19] and fluid transport through pores and voids [36]. Fracture/fault geometry has been measured on many scales ($10^{-5}$–$10^{4}$ m) and thus allows for possible scaling of laboratory and numerical findings to the field.

## Key questions and dissertation layout

This dissertation addresses fundamental questions surrounding the connection between fracture specific stiffness and fluid transport under a range of loading conditions and dynamic stressing. Moreover, I do so by performing complex experiments under triaxial stresses and use simultaneous continuous active-source ultrasonic monitoring and fluid flux measurements to measure the static and dynamic elastic and hydraulic properties of fractures. These unique experiments are also complemented by post-surface and topography characterization using pressure registering films and profilometry.

To address these fundamental questions regarding fracture stiffness and fluid transport, I ask the following questions: 1. Chapter 2: How does permeability enhancement and nonlinear elastic changes of an in-situ fracture evolve with shear? 2. Chapter 3: How do fracture aperture and contact area evolve with stress state and effect hydraulic and elastodynamic changes in response to dynamic stressing? 3. Chapter 4: What is the role of fracture roughness in modulating elastic properties, deformation, and fluid transport? Additionally, to what extent can fracture roughness properties be scaled beyond laboratory observations? 4. Chapter 5: How does the interplay between granular

layers and fracture roughness influence static elastic and fluid flow properties? What is the role of dynamic stressing on modulating the hydraulic and elastic responses of granular-filled fractures?

My key contributions in this dissertation are characterizing how fracture properties (roughness, aperture, granular in-fill, interface stiffness) affect nonlinear elasticity and fluid transport under loading conditions that simulate shallow depths and dynamic stressing sources.

# Chapter 2

## Imaging elastodynamic and hydraulic properties of in-situ fractured rock: An experimental investigation exploring effects of dynamic stressing and shearing

### 2.1 Abstract

We describe laboratory experiments to elucidate the relationship between nonlinear elasticity and permeability evolution in fractured media subjected to local stress perturbations. This study is part of an effort to measure fluid pathways and fracture properties using active-source acoustic monitoring during fluid injection and shear of rough fractures. Experiments were conducted with L-shaped samples of Westerly granite fractured in-situ under tri-axial conditions with deionized water subsequently circulated through the resulting fractures. After in-situ fracturing, we separately imposed oscillations of the applied normal stress and pore pressure with amplitudes ranging from 0.2 to 1 MPa and frequencies from 0.1 to 40 Hz. In response to normal stress and pore pressure oscillations, fractured Westerly granite samples exhibit characteristic transient softening, acoustic velocity fluctuations, and slow recovery, together with permeability enhancement or decay, informing us about the coupled nonlinear elastodynamic and poromechanical rock properties. Fracture interface properties (contact asperity stiffness, aperture), are then altered in-situ by shearing, which generally decreases the measured elastic nonlinearity

and permeability change for both normal stress and pore pressure oscillations.

## 2.2 Introduction

Dynamic stresses associated with energy production and waste water sequestration (injection, pumping, and transport of supercritical $H_2O$–$CO_2$ fluids) are a potentially important contributor to injection-induced seismicity [42, 70, 71, 88, 110, 111, 119]. These perturbations can cause significant changes in the local stress field and poromechanical properties in the subsurface and therefore act as a diagnostic for impending fault reactivation and prospective changes in permeability - among other utilities. Therefore, it is crucial to understand how fluid injection influences the hydromechanical properties of rocks and, in particular, associated fractures. Natural and anthropogenic sources of dynamic perturbation each impact poromechanical properties through similar mechanisms and in similar ways, suggesting uniform controls relating nonlinear stiffness to poromechanical properties. We characterize these dependencies to define the potential to link nonlinear acoustic properties to the evolution of reservoir state and behavior.

Empirical evidence from the field and laboratory show that earthquakes and subsequent seismic waves cause transient changes in rock stiffness in the proximity of faults. Specifically, field observations document a sudden reduction in elastic wave velocity associated with co-seismic softening and a post-seismic recovery of rock stiffness that is logarithmic in time e.g., [12]. Similar observations have been made in the laboratory [30]. Moreover, lab studies using dynamic acousto-elastic testing [106], show that ultrasonic wave velocity decreases during dynamic stressing and then recovers with the logarithm of time. These studies show that dynamic strains on the order of $10^{-6}$ are sufficient to cause the nonlinear elastic effects [41, 93].

The nonlinear behavior of rocks is sensitive to both fine-scale features and second-order constitutive effects, such as fracture apertures (impacting flow pathways, asper-

ity stiffness) and nonlinear stiffness (impacted by rate-dependent friction and healing). In order to fully understand the ramifications of dynamic stressing in the subsurface, we need to elucidate the relationship between the elastodynamic and hydromechanical properties of fractured rocks. Currently, the literature characterizing relationships between elastodynamic and poromechanical response and subsequent recovery is limited [105]. We present results from sophisticated and highly-constrained laboratory experiments in which we combine the analysis of nonlinear elastodynamic and hydraulic data.

In this paper we briefly revisit experimental results from [105], but expand the focus with additional measurements of imaging acoustic nonlinearity across a fracture using multiple P-polarized lead-zirconate (PZT) transmitter-receiver pairs. Also, we relate the average nonlinear acoustic response to fracture permeability as an averaged hydraulic measurement. Another important parameter that we analyze is how the fracture recovers from dynamic stressing. Most importantly, we investigate the effect of shearing on elastodynamic and hydraulic properties of fractures. This is central to this work in that shearing considerably modulates the fracture interface, generating wear material (gouge, breccia) and changing contact asperities, respectively in qualitative terms, which has the objective of simulating conditions found in the subsurface.

## 2.3 Experimental Setup

We conducted laboratory experiments in a true triaxial configuration using fractured granite samples in-situ while simultaneously measuring flow rate and nonlinear elastic properties. Samples of Westerly granite were cut into L-shape blocks (69 x 45 x 50 x 26 mm, Figure 2.1) with 3 mm deep notches on the top and base to guide the evolution of planar fractures driven by shear loading to failure. The L-shape is used for maintaining constant nominal contact area during both initial fracture then shear. Our samples

were saturated with deionized water (submerged in water for 24 hours) and then placed between steel loading platens with embedded piezoelectric transducers. The PZTs from APC International Ltd. are 6.5 mm in diameter, with a center frequency of 500 kHz and are epoxied in blind holes 4 mm from the rock sample (Figure 2.1). The loading platens contain internal conduits to provide a line source of fluid at either end of the fracture plane. Fluid access at both ends of the fracture was via a narrow channel (45 x 1 mm) fitted with sintered porous fits (permeability $\approx 10^{-14}\ m^2$) and fed by five 1.6-mm diameter holes, as shown in Figure 2.1e. Deionized water was pumped through the fracture at constant pressure drop using independent high speed servo-controllers for both inlet and outlet pressure (Figure 2.1).

The experimental apparatus consists of a stiff load frame and two hydraulic pistons capable of applying force in either displacement- or load-control mode and a pressure vessel with independent control of pore and confining pressures. Applied forces are measured using custom-built, beryllium-copper strain-gauge load cells mounted on each loading piston. The load cells have an amplified output of $\pm 5$ V with an accuracy of $\pm 5$ N and are calibrated with a Morehouse proving-ring. Displacements are measured with direct-current displacement transducers (DCDT), with an accuracy of $\pm$ 0.1 $\mu m$. Confining pressure was created using a food-grade heat transfer oil (XCELTHERM 600, Radco Industries). A linear variable differential transformer (LVDT) was attached to the sample inside the pressure vessel to accurately ($\pm 0.1\ \mu m$) measure changes in fracture dilation/closure. Pressure intensifiers fitted with LVDTs and pressure transducers were used to control the confining pressure and the internal upstream and downstream fluid pressures.

Each axis of loading is independently servo-controlled and all stresses, strains, fluid pressures and fluid volumes were recorded with a $\pm 10$ V, 16-channel 24-bit analog-to-digital converter at 10 kHz and averaged to sampling rates of 100 Hz or 1 kHz, see Figure

2.2 for schematic of data acquisition system. Fluid flow across the fracture was measured using upstream and downstream pore-pressure intensifiers and the permeability was subsequently calculated. Active ultrasonic data were recorded using a Vantage$^{TM}$ Research Ultrasound (Verasonics) system. We use broadband ($\sim$0.02-2 MHz) PZTs (APC International Ltd. 6.35 mm diameter compressional crystals), which were successively pulsed every 1 ms on the transmitting side and recorded at the receiver side with a sampling rate of 25 MHz. The input signal is a half sine with a frequency of 500 kHz. Also, external triggers sent at regular intervals (of order 1 s) by the Verasonics system were recorded by the 24-bit analog-to-digital data acquisition system. This provided a means for synchronizing the fast-sampled "ultrasonic" and lower sampled "poro-mechanical" data. We used these data to measure changes in the permeability and elasticity of the fractured rock samples.

### 2.3.1 Experimental Procedure

Each experiment commenced with extensive sample preparation in which the Westerly granite was cut and notched, sealed in a latex jacket, and then placed inside the pressure vessel. The latter was filled with confining fluid before a horizontal stress of 20 MPa was applied. We chose this confining stress such that our results can be compared with previous experimental work [20, 21]. Confining fluid pressure was slowly increased to 15 MPa afterwards. We then applied pore pressure: inlet ($P_{pA}$ = 4 MPa) and outlet ($P_{pB}$ = 2 MPa). At this state there was no flow because the Westerly granite matrix permeability is very low ($< 10^{-20}$ $m^2$) and the confining fluid pressure (around the jacketed sample) is greater than the pore pressure, preventing the short-circuiting flow of water around the sample.

A shear load was then applied with the vertical piston in displacement mode at a constant rate of 10 $\mu m/s$ for a total of approximately 4 - 5 mm. Samples fractured

in-situ after reaching a critical stress of ≈55 MPa (see inset of Figure 2.3c and Figure S2 Appendix A), after which we locked the vertical piston. Fluid flow and acoustic emissions were measured during fracture, but here we focus on dynamic stressing which was implemented via oscillations of the effective normal stress.

Oscillations of the applied normal stress were applied with the horizontal loading piston at prescribed amplitudes (0.2 to 1 MPa) and frequencies (0.1, 1, 10, 40 Hz). Pore pressure oscillations were achieved by oscillating $P_{PA}$ at amplitudes of 0.2 to 1 MPa and frequencies of 0.1, 1, 10 Hz while holding $P_{PB}$ constant. Multiple sets of normal stress and pore pressure oscillations of varying amplitudes and frequencies were applied to investigate: (1) repeatability and direct comparison between the two modulated stresses (normal stress and pore pressure) and (2) amplitude and frequency dependencies of the measured response. Post-fracture dynamic stressing is plotted in Figure 2.3d and shows the normal stress (red) and pore pressure (blue) oscillations. To investigate the effect of shearing and resulting changes in fracture properties (heterogeneous aperture, flow pathways, contact asperities) and generated wear material on elastic nonlinearity and permeability, the sample was sheared in two 4 mm (held at $\sigma_{NS} = 20$ MPa), stages, which are shown for experiment p4975 in Figures S3-S4 (Appendix A). After each shearing stage the oscillation protocol was applied to the sample. Initially, the in-situ fracture was quite rough with fines throughout, but the effect of shear reduces and changes this roughness; the old contacts were broken and new contacts formed, changing the extent to which the two halves of the fracture were mated. Throughout shear the size, shape, and amount of wear products, or fines, continuously evolves and likely has a complicated effect on fluid flow, see Figure S1 (Appendix A) for qualitative evidence of wear material generated during experiment p4975. These measurements allow investigation of how fracture properties are related to the elastodyamic and hydromechanical properties.

### 2.3.2 Permeability Measurements

We measured flow rates independently at the fracture inlet ($Q_A$) and outlet ($Q_B$) using the outputs of LVDTs on the pressure intensifiers, see Figure S3 (Appendix A). After verifying the steady state flow condition ($Q_A - Q_B \leq 5\%$), Darcy's law was used to calculate permeability $k$:

$$k = \frac{\mu L}{S} \frac{Q}{\Delta P_P} \tag{2.1}$$

where $Q = \frac{1}{2}(Q_A + Q_B)$ is the average flow rate ($\frac{m^3}{s}$), $\mu$ is the fluid viscosity ($10^{-3}$ Pa $\cdot$ s) at 20 °C, $L$ is the flow path given by the length of the sample (50 mm) and $S$ is the cross-sectional area perpendicular to the flow path (45 x 26 mm$^2$). Specifically, $k$ is the bulk permeability, that is, the permeability of the surrounding rock matrix (on order of $10^{-21}$ m$^2$) and of the fracture. Alternative calculations of permeability are valid [50,134], however we are interested in relative changes in permeability in response to dynamic stressing, rather than the absolute value of fracture permeability.

### 2.3.3 Ultrasonic Measurements: Active Source

Ultrasonic waves transmitted through the fracture were recorded continuously in each experiment. Half-cycle sinusoidal pulses with an amplitude of 40 V and center frequency of 500 kHz were emitted consecutively from each transmitting transducer (9 piezoelectric discs arranged in a 3 x 3 matrix embedded within the right-hand loading platen in Figure 1c) with a pulse repetition frequency of 100 Hz or 1000 Hz during the low and high frequency ($\geq$ 10 Hz) stress oscillations, respectively. The waveforms were amplified ($\sim$ 40 dB) and recorded for all the receiving transducers (12 piezoelectric discs arranged in a 4 x 3 matrix embedded within the left-hand loading platen in Figure 1c). In this

study we utilized 1 transmitter and 3 receivers. Details of the ultrasonic data analysis are shown in in Figure 2.4. Figure 2.4a shows an excerpt of a normal stress oscillation, red, and the received waveforms (decimated) in the same time domain. Two signals highlighted in green and yellow are projected down to Fig. 2.4b to demonstrate the connection between time shift, velocity, and the influence of the stress perturbation. The changes in ultrasonic wave velocity are determined by first calculating the time shift by the cross-correlation of each received signal with a reference waveform. The reference waveform is generated by averaging 50 waveforms at the beginning of each experimental run, when there are no stress oscillations. The window of cross-correlation is chosen to include the p-wave arrival to the end of of one period, as shown in Figure 2.4c. Since the calculated time shifts are typically on the order of 1 ns, smaller than the sampling rate of 5 MHz, the estimation of the time shift is improved by fitting the peak of the cross-correlation function with a second order polynomial, Figure 2.4d. The maximum of the parabola (fitted to the two data points adjacent to the cross-correlation maximum) corresponds to the modified time shift.

## 2.4 Results

We combine ultrasonic data, strain measurements, and permeability to document the nonlinear elastodynamic response and poromechanical effects of dynamic stressing. Here, we draw from an extensive set (>10) of experiments, calibrations, and tests to focus on data from two distinct experiments with a range of stressing amplitudes, frequencies, and shearing.

### 2.4.1 Nonlinear elastodynamic and hydraulic responses

Linear elasticity does not fully describe the behavior of rocks especially if they are fractured, highly stressed or subject to large-amplitude dynamic stressing. Even undamaged

rocks exhibit a range of nonlinearity due to a variety of structural features such as microcracks and soft grain boundaries [93]. When fractured or damaged, the nonlinearity of the rock is further affected by contact acoustic nonlinearity at fracture interfaces. The characteristic responses to dynamic stressing (transient softening, velocity modulation, and slow recovery) as shown in Figure 2.5, are indicative of nonlinear mesoscopic elasticity [41] and highly informative on rock micro-structure, fractures, and inter-grain contacts. Crucially, these are the features that also control the hydraulic properties of rock. Therefore, instead of analyzing the linear elastic response (wave speed and amplitude), we focus on the nonlinear elastic response i.e., the stress-dependency of wave speed and amplitude.

Through our active source ultrasonic monitoring we characterize the elastodynamic properties of the fractured Westerly granite by quantifying its response to dynamic stressing. Figure 2.5 demonstrates typical recorded elastodynamic and hydraulic responses to a 1 Hz, 1 MPa normal stress oscillation in experiment p4966. We characterize the elastodynamic response with three parameters to describe the nonlinearity, $\Delta c/c_0$, $dc/c_0$, and $\Delta A/A_0$. To calculate $c_0$ and $A_0$, we choose 1-s time windows that are short enough to capture pre- and post-oscillation values but long enough to provide averaged values not affected by local fluctuations in the data. Wave velocity changes from its initial value $c_0$ to a new steady-state value $c$ in response to a perturbation and $\Delta c$ is calculated as the average wave velocity over the oscillation duration excluding two cycles in the beginning and the end. We quantify the difference $c - c_0$ as $\Delta c$. In the case of Figure 5, the velocity decreased from about 4383.5 m/s to about 4832 m/s after the normal stress oscillation ended, so $\Delta c \approx 1.5$ m/s.

The RMS wave amplitude, $A$, is calculated in the time domain in a window comprising the first arrived p-wave, see Figure 2.4c. Dynamic stress oscillations result in a sudden decrease in amplitude relative to the initial value $A_0$ to a new temporary non-

equilibrium state. Therefore, both $\Delta c/c_0$ and $\Delta A/A_0$ represent nonlinear ratios that demonstrate the transient effect of dynamic loading on fracture stiffness, for a range of stress amplitudes and frequencies. Although RMS amplitude can be extracted from our data, that is not the main focus of this paper, but some results are reported in the Supporting Information in Figures S6-S7. Another nonlinearity parameter that we identify is modulation of the wave velocity, $dc$, during oscillations at frequencies that are harmonics of the driving frequency. This quantity represents the average amplitude of wave velocity modulations during dynamic perturbations after the system reaches a non-equilibrium state. Finally, after being stressed, the fractured rock exhibits long-term "recovery" trending toward the initial $c_0$ value, in which the wave velocity or amplitude evolves to a new steady state. The wave velocity evolution from post-oscillation to initial $c_0$ is well described by a logarithmic function of the form $c_r = \dot{c}\ \log t + b_1$, where $\dot{c}$ is the slope (recovery rate) and $b_1$ is the intercept.

The stress-induced changes in permeability are captured by two parameters: (1) The transient change in permeability $\Delta k/k_0$ defined as the %-change due to the imposed normal stress or pore pressure oscillations, normalized by the pre-oscillation permeability $k_0$ as illustrated in Figure 2.5c [20] and (2) the linear in log time rate of permeability recovery after the transient increase $\dot{k}$ where $k_r = \dot{k}\ \log t + b_2$, where $\dot{k}$ is the slope (recovery rate) and $b_2$ is the intercept. Figure 2.5 shows the pre-oscillation permeability $k_0$ and the post-oscillation permeability $k = k_0 + \Delta k$ calculated by averaging the measured values over 10- and 1-s time windows. Calculation discontinuities in permeability measurements shown in Supplemental Figure S3 correspond to times for which inlet/outlet flow rate difference exceeds the 5% threshold that we impose to ensure steady state flow. Permeability during dynamic stressing is indeterminate because there is no steady-state flow and the diffusion time across the fracture is slower than the higher oscillation frequencies (10 and 40 Hz).

To better illustrate how the elastodynamic and hydraulic properties of fractured rock change in response to dynamic perturbation we show an excerpt from the post-fracture stage of experiment p4975 in Figure 2.6. Figure 2.6 demonstrates how the inlet and outlet flow rates evolve during a 0.1 Hz normal stress oscillation; three colorbars highlight zoomed cycles in Figure S6. Note the clear evidence of compression and tension in the fracture normal displacement with increased and decreased normal stress (Figure 6). The inlet $Q_A$ flow rate is in phase with the imposed stressing, but the outlet flow $Q_B$ is 180° out of phase and of a much smaller magnitude than that of the inlet. These observations demonstrate the magnitude of changes we are characterizing and also reinforce that the fracture is continuously evolving during the dynamic perturbations; contacts undergo compression and tension resulting in changing fluid flow paths along the fracture. In subsequent subsections we discuss how nonlinear elastodynamic and hydraulic parameters $\Delta c/c_0$, $\Delta k/k_0$, $dc/c_0$, and $\Delta A/A_0$ vary with normal stress and pore pressure oscillation amplitudes and frequencies. We also discuss how these results are affected by shearing for both experiments p4966 and p4975.

### 2.4.2 Dynamic Stress-induced Changes in Permeability and Wave Velocity

Changes in fracture closure cause both changes in permeability and stiffness. A more complete understanding of both physical phenomena is important for understanding processes that control energy production from, and waste storage in, the subsurface. In this section, we report and compare the stress amplitude and frequency dependencies for both sets of parameters. Although these experiments pertain to different samples/fractures, both are composed of the same rock type, and the same loading conditions were used to produce the shear fractures.

The dependency of $\Delta k/k_0$ on the amplitude of normal stress and pore pressure os-

cillations is shown in Figure 2.7, which additionally differentiates the order in which the 1 Hz oscillations sets were imposed. We observe that the relative permeability change $\Delta k/k_0$ scales with the amplitude of 1 Hz normal stress oscillations and, to a greater degree, pore pressure oscillations in the post fracture case. Another interesting observation here is that the order in which oscillations were applied has an effect on the permeability enhancement/reduction. The first pore pressure oscillation set generally produces the largest permeability enhancement in the post-fracture case, but this is not observed for normal stress oscillations, where the second set is the most effective. This is likely due to how the pore pressure and normal stress oscillation sets were alternated during the experiments, see Figure 2.3d. The 1 Hz normal stress oscillations (increasing amplitude) are separated by successive pore pressure oscillation sets, rather than performing all of one oscillation type and then the other in each part of the experiments.

After shearing the fractures (5 mm in p4966 and 4 mm in p4975) the relationship between permeability enhancement and oscillation amplitude deteriorates. The post-shear normal stress oscillations sets cause no permeability enhancement with increasing amplitude, but noticeable reduction at larger amplitudes (>1 MPa). Though there is no clear linear trend, pore pressure oscillations are still able to enhance permeability in the first post-shear set. Another observation here is that permeability enhancement is less influenced by normal stress oscillation order compared to the pore pressure oscillations. After the second set of shear, both pore pressure and normal stress oscillation resulted in permeability reduction for nearly all amplitudes.

The relative change in velocity $\Delta c/c_0$ for the direct transmitter-receiver pair as a function of 1 Hz normal stress and pore pressure oscillation amplitudes are plotted in Figure 2.8. As expected [93], we observe an increasing velocity drop (more negative $\Delta c/c_0$) with oscillation amplitude for both normal stress and pore pressure. In this measure of fracture nonlinearity there is a clearer trend between oscillation order and

magnitude, for this transmitter-receiver path. For both oscillation types (normal and pore pressure), subsequent sets of oscillation reduce the magnitude of $\Delta c/c_0$.

Interestingly, shear displacement scarcely changes the magnitude of nonlinearity ($\Delta c/c_0$) with respect to the post-fracture case, especially for normal stress oscillations in experiment p4975. Another interesting observation from this transmitter-receiver pair is an increase in nonlinearity from post-fracture to post-shear 1 in experiment p4966. In the next section, we report other transmitter-receiver pairs across the fractures.

### 2.4.3 Spatial Variations of the Nonlinear Elastodynamic Response

The elastic response ($\Delta c/c_0$) presented in Figure 2.8 corresponded to a single pair of transducers. To further our understanding of the coupling between elastodynamic and hydraulic response to dynamic stressing, we investigate the spatial variations of the elastic response along the fracture by analyzing all available transmitter-receiver pairs measurement of wave velocity (Figures 2.9 – 2.10). Figures 2.9 and 2.10 show a coarse view of the nonlinear elastodynamic response across the fracture as a function of applied oscillation amplitude. Note that data point shape corresponds to oscillation frequencies. The direct path sensor (blue PZT in Figures 2.9 – 2.10) results were discussed in the previous section. The focus here is to describe observations regarding the other transmitter-receiver paths, that is the heterogeneity of the fracture interfaces. The other sensors measure larger differences in values and also more linearity in the case of the bottom sensor in p4975. The second shear displacement reduces nonlinearity (direct pair) and modestly increases nonlinearity (top sensor path), but does not have an overall coherent trend for both experiments and all increments of shear. The response to pore pressure oscillations, Figure 2.10, shows more coherent results as compared to applied normal stress. Again, large amplitude and high frequency oscillations generally pro-

duce the largest magnitude of relative change in velocity. This particular measurement of nonlinear elasticity is noticeably lower in experiment p4975 for the bottom receiver path. Another important observation is that shearing has little effect on the magnitude of nonlinearity for pore pressure oscillations. There are instances of large differences in nonlinearity at a particular amplitude and frequency (10 Hz for example), which are a function of oscillation set order. Generally, subsequent oscillation sets produce less nonlinearity, though this is not always the case.

Figure 2.11 relates permeability changes $\Delta k/k_0$, an hydraulic measurement averaged over the fracture plane, to the change in wave velocity $\overline{\Delta c/c_0}$ averaged across all receiver locations. The data point shapes again correspond to the oscillation frequencies and their sizes correspond to oscillation amplitude. The main observation for the post-fracture oscillation sets is that relative changes in permeability and wave velocity are highly connected. That is to say, larger normal stress or pore pressure oscillation amplitudes and frequencies produce larger transient softening and permeability enhancement for two separate experiments (different fractured samples). Overall, shearing weakens this relationship, reducing the amount of nonlinearity and permeability enhancement for both methods of dynamic stressing. Though, in the case of normal stress oscillations, the relationship with amplitude and frequency still exists, but the overall slope decreases due to shear displacement.

### 2.4.4 Wave Velocity Modulation

The direct effect of dynamic stressing is an instantaneous modulation in wave velocity at harmonic frequencies of the driving frequency. We denote the mean velocity amplitude as $dc$ (e.g., Figure 5). The relative change in average velocity oscillations $dc/c_0$ is a proxy for the nonlinear parameter $\beta$, estimated from the second harmonic (e.g., [41, 92, 93]). We observe a monotonic relationship between the magnitude of $dc/c_0$ and oscillation

amplitude for both rock samples (Figure 2.12).

There is a consistent trend that subsequent oscillation sets decrease the magnitude of nonlinearity of $dc/c_0$ for normal stress modulation. Pore pressure oscillations exhibit little to no change through subsequent repetitions, except for larger driving amplitudes. Shearing the fracture generally decreases the measured nonlinearity, especially for experiment p4966 (Figure 2.12). The trend is not as strong for p4975, where little to no change in $dc/c_0$ nonlinearity is observed after the first shear increment. Then, after the second shear, pore pressure oscillations interestingly increase the nonlinearity.

### 2.4.5 Permeability and Wave Velocity Recovery from Dynamic Stressing

The long-term evolution of permeability and wave velocity reveal the extent to which the fracture properties (asperities, loose wear material) recover from dynamic stresses. We observe that the magnitude of the log-time permeability recovery increases with pore pressure oscillation amplitude (see insets of Figure 2.13). Though our observations for post-shear are limited, the measurements suggest a decreasing rate of recovery as a result of shearing the fracture, as shown in Post - Shear 1 and 2 in Figure 2.13. The permeability recoveries from normal stress oscillations are minuscule and slopes have very low goodness of fit and we do not report the data.

The wave velocity recovery rate $\dot{c}$ for the direct transmitter-receiver pair as a function of 1 Hz normal stress and pore pressure oscillation amplitudes is plotted in Figure 2.14. We observe faster recovery with oscillation amplitude for both normal stress and pore pressure. In the post-fracture phase, there is a noticeable effect of order of $\sigma_{NS}$ oscillations on recovery rate; later oscillation sets exhibit smaller magnitude of $\dot{c}$, which suggests detectable damage to the fracture properties from the first oscillation set. The differences between oscillations sets decreases with shearing the fracture in both oscilla-

tion types. The effect of shear on fracture $\dot{c}$ is a decrease in the magnitude of recovery rate with oscillation amplitude for normal stress and pore pressure oscillations. Additionally, the differences between oscillation sets is generally reduced for both oscillation types.

Figure 2.15 relates the wave velocity recovery rate $\dot{c}$ averaged over all receiver locations to permeability changes $\dot{k}$, a hydraulic measurement across the fracture. The main observation $\dot{c}$ and $\dot{k}$ are more correlated for pore pressure oscillations in the post-fracture phase, though sparse. Also, there does not seem to be obvious scaling of frequency with the relation between $\dot{c}$ and $\dot{k}$. Overall, shearing the fracture decreases both the velocity and permeability recovery rates for pore pressure oscillations, especially in experiment p4975.

## 2.5 Discussion

Nonlinear elastic behavior of rocks is sensitive to fine-scale features, such as fracture aperture (impacting flow pathways, asperity stiffness) and nonlinear stiffness (impacted by rate-dependent friction and healing). We report the relation between changes in wave velocity and permeability in response to dynamic stressing and shearing. Furthermore, the heterogeneous measurements along multiple transmitter-receiver ray-paths across the fracture help illuminate the underlying mechanisms.

We show shearing the fracture significantly reduces the permeability enhancement as a function of amplitude oscillation, especially for normal stress oscillations, Figure 2.7. Another observation is that alternating between pore pressure and normal stress oscillations and/or subsequent sets of oscillations increases the magnitude of permeability enhancement for normal stress oscillations (post-fracture), but reduces permeability enhancement from pore pressure oscillations, noticeable even in the first post-shear experimental runs. This may be influenced by the wear material, gouge, generated at the

fracture interface during shear clogging and unclogging fluid pathways along the fracture. Measurements of nonlinearity ($\Delta c/c_0$) of the fracture interface, show that shearing the fracture modestly decreases the nonlinear response for both types of oscillations. Again, we find that the order of oscillation appears to have an effect on the evolution of the fracture interface by reducing the magnitude of nonlinearity ($\Delta c/c_0$) for oscillation amplitudes (normal stress and pore pressure). Perhaps, that particular fracture properties changed (more asperities in contact, different amount of gouge material) after shearing to produce a greater degree of nonlinearity; further experiments could allow us to determine the mechanism for this change.

The distinct transmitter-receiver ray paths reveal fractures with highly heterogeneous properties as the relation between $\Delta c/c_0$ and oscillation amplitude varies greatly for both normal stress and pore pressure perturbations, Figures 2.9-2.10. The observed differences are not completely unexpected given that fractured Westerly granite samples (Figures 2.1c and S1 (Appendix A)) have a heterogeneous aperture and irregularly distributed wear products (Figure S1 Appendix A), especially following the application of shear displacement. This is perhaps due to the fracture interface not being in contact compared to the rest of the fracture. Furthermore, there is much more similarity in results for the separate experiments than observed in the normal stress oscillations. It is conceivable that shearing widens the aperture in some locations, which could be filled with wear/gouge material or remain empty, while other parts of the fracture aperture could become closed. These possibilities may be partially responsible for the complicated behavior we observe.

To "predict" permeability change from nonlinear acoustic characterization of dynamically stressed fractured (and sheared) rock, we relate the relative velocity change ($\Delta c/c_0$) to the permeability changes $\Delta k/k_0$ and the recovery rates of velocity and permeability. Previous experimental work suggest that changes in permeability during pore

pressure oscillations results from unclogging fluid pathways, or conduits containing gouge material [20,21]. Other experimental work [105] and current results challenge this as the sole mechanism since normal stress oscillations consistently produce permeability enhancement post-fracture. This can be seen in Figure 2.11, where the average magnitude of nonlinearity ($\Delta c/c_0$) increases with permeability enhancement for both normal stress and pore pressure oscillations. However, after shear, the relationship changes such that there is less nonlinearity ($\Delta c/c_0$) and less permeability enhancement, especially for normal stress oscillations. Subsequent shearing continues this trend of reduced nonlinearity and permeability reduction. Overall, these results suggest normal stress oscillations, opening and closing mechanism of the fracture, is less effective in mobilizing fines to migrate along the fracture conduits, pathways, as more gouge is ostensibly created with shearing the fracture. Pore pressure oscillations are more effective in mobilizing the fines, thus allowing for a more rapid recovery to its initial state. Perhaps there is a complex interplay between gouge mobilization enhancing the permeability, but also reducing the fracture interface contact area, thus decreasing wave velocity as shown in Figure S9 (Appendix A).

The direct effect of dynamic stressing is quantified as the mean velocity amplitude as $dc$, a proxy for the second harmonic nonlinear parameter. There is a clear monotonic relationship between $dc/c_0$ and oscillation amplitude (normal stress and pore pressure) for both rock samples (Figure 2.12). Shearing decreases this measure of nonlinearity for normal stress oscillations, but slightly increases for pore pressure oscillations (p4975). We conjecture that the two types of dynamic stressing activate two different mechanisms: (1) opening/closing of pore throats from normal stress oscillations and (2) directly dislodging and mobilizing fines along the fracture from pore pressure oscillations.

In this study, we also measure the log-time recovery of permeability and velocity after dynamic stressing. These results show that larger pore pressure oscillation amplitudes

increases (the absolute value of) the rate of recovery. After shearing we observe slower log-time evolution of permeability, though our observations are very limited in this case. There is perhaps a complex effect from deformation of fracture asperities and the granular wear material that inhibit the recovery from the transient response to dynamic stressing. We hypothesize that the wear material comminuted as a result of subsequent shearing and normal stress oscillations, is transported along the fracture during the pore pressure oscillations, and impedes a recovery from the transient change.

## 2.6 Conclusions

We report laboratory experiments to determine the effects of dynamic stressing and shearing on elastodynamic and hydraulic properties of fractured rock. Monitoring in-situ fractures with active source ultrasonic transmission and fluid permeability during dynamic stressing driven by both normal stresses and fluid pressures reveals the complex relation between elastodynamic and hydraulic properties.

In response to oscillations of effective normal stress, fractured Westerly granite samples exhibit characteristic transient softening, acoustic velocity fluctuations, and slow recovery, informing us about microstructure and contact mechanics. As found in [105], large amplitude and high frequency oscillations generally increase permeability, with pore pressure oscillations producing the largest enhancement of permeability. In this study, we add to previous work [105], by analyzing the effect of shearing on the elastodynamic and hydraulic properties of fracture rock. Furthermore, we document spatial variability in elastodynamic properties across the fractured samples, revealing the effect of changes in fracture properties (such as contact asperity stiffness, aperture). We find that shearing generally decreases the relative velocity change ($\Delta c/c_0$) for both normal stress and pore pressure oscillations. The underlying physics remain unclear as to how fracture nonlinearity parameters ($\Delta c/c_0, dc/c_0, \dot{c}$) are correlated to hydraulic properties ($\Delta k/k_0, \dot{k}$)

resulting from dynamic stressing and fracture interface change (shearing). However, we hypothesize that the fracture dilation and compaction (heterogeneous aperture change) dominate during applied normal stress oscillations and clogging/unclogging dominates during pore pressure oscillations and these phenomena are related to the underlying mechanisms responsible for the observed nonlinearity and permeability changes.

Further experiments are warranted to decouple the effect of gouge material evolution and fracture asperities from the log-time recovery of permeability and velocity. We will develop methods to collect fine gouge material generated from in-situ fracturing and shearing in the downstream pore pressure lines in an attempt to quantify the degree to which unclogging mechanisms are responsible for the results we observe. Another way of investigating the effect of gouge transport is to systematically vary the thickness of a synthetic gouge layer of pre-fractured granite samples. Future experiments with pre-fractured samples will include characterization of surface roughness with high-resolution profilometry to better constrain the underlying mechanics of aperture and permeability change.

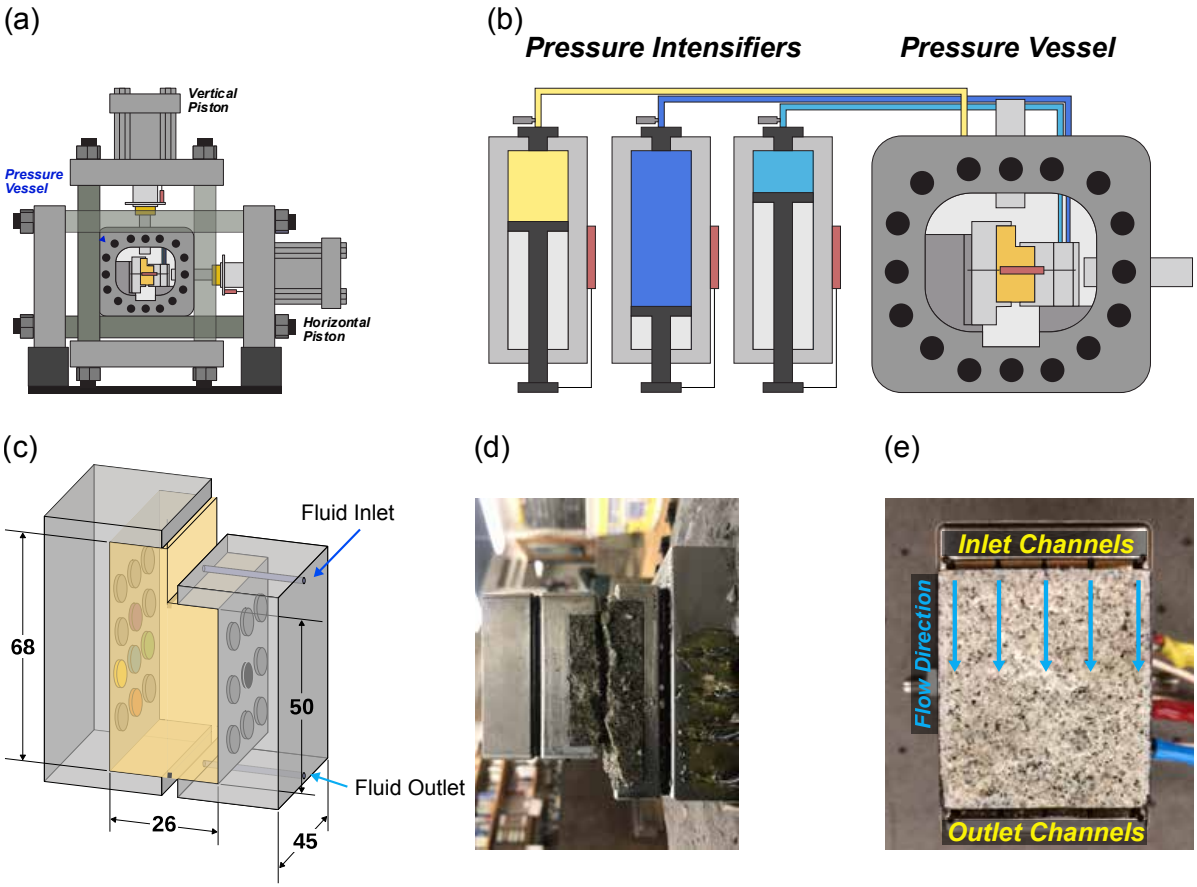



**Figure 2.1.** (a) The Biaxial deformation apparatus has servo-controlled vertical and horizontal pistons and a 10 kHz 24-bit analog to digital data recorder. (b) A pressure vessel is inserted into the Biax to create true triaxial loading. Pressure intensifiers control the confining pressure ($P_C$) and sample ($P_{PA}$ and $P_{PB}$ ) fluid pressures. (c) L-shaped samples of granite were loaded with platens containing piezoelectric transducers (p-polarized). After securing the sample in the loading platens it is sealed in a latex jacket to separate confining and pore fluids. (d) A photo of the sample after experimentation highlights the degree of roughness resulting from the in-situ fracturing. (e) Post-mortem photograph showing the rough fracture and fluid flow channels.

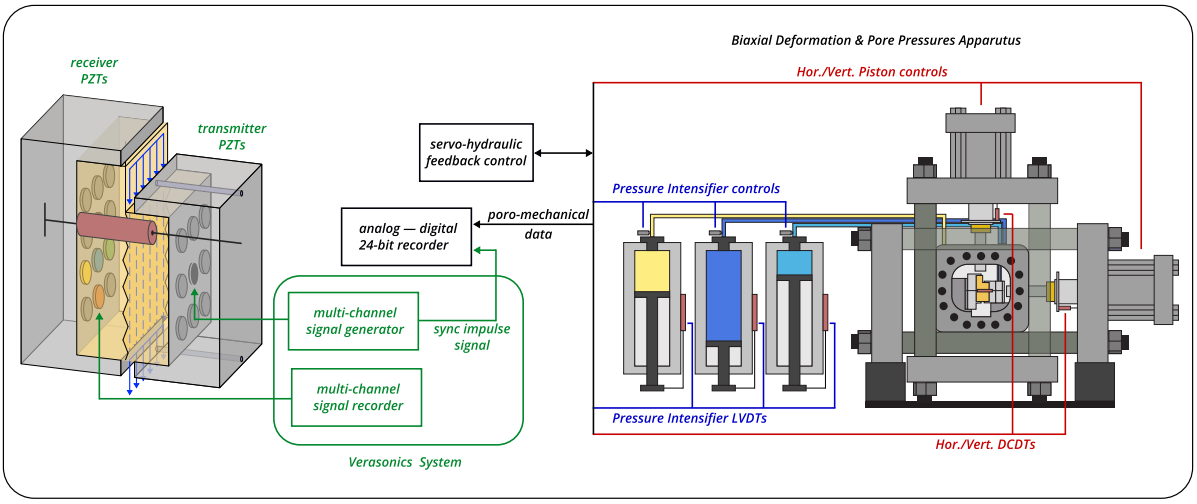



**Figure 2.2.** Schematic of the single direct shear configuration with the block diagram showing the main features of the data acquisition system for both the poro-mechanical and ultrasonic data. Each axis of loading is independently servo-controlled and all stresses, strains, fluid pressures and fluid volumes were recorded with ±10 V, 16-channel 24-bit analog-to-digital converters at 10 kHz and averaged to sampling rates of 100 Hz or 1 kHz. An LVDT (shown as red cylinder) was used to measure the dilation/compaction of the fracture. Active ultrasonic data were recorded using a Vantage TM Research Ultrasound (Verasonics) system. Also, the Verasonics system sends external triggers at regular intervals ($\approx$ 1s) that are recorded by the 24-bit analog-to-digital data acquisition system. This allows synchronizing of the ultrasonic data to the poro-mechanical data and then their joint analysis.

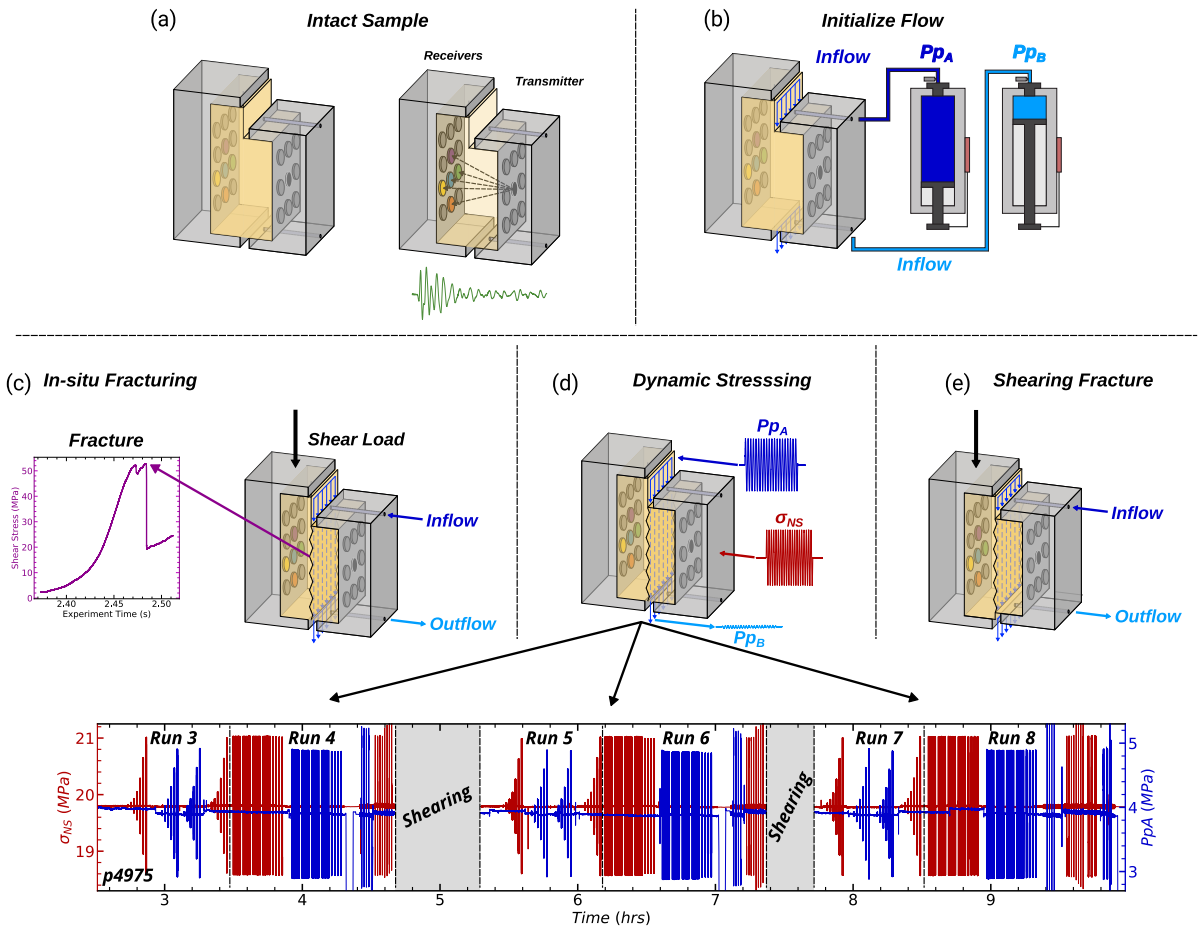



**Figure 2.3.** (a) Sketch showing sample dimensions and approximate PZT transmitter - receiver ray paths. (b) Fluid flow and pore pressure with inlet ($P_{PA} = 4$ MPa) and outlet ($P_{PB} = 2$ MPa). (c) Shear stress on the fracture plane was increased by advancing the long end of the L-shaped sample at a constant rate of 10 $\mu m/s$ while holding the short end in place. Fracture occurred in two stages at ≈55 MPa. (d) Sketch showing the oscillation protocol applied to the freshly fractured sample. Multiple sets of $P_P$ and $\sigma_{NS}$ oscillations of varying amplitude (up to about ± 1 MPa) and frequency (0.1, 1, 10 and 40 Hz) were applied. Oscillation sets are defined by a group of repeating oscillations of the same frequency or increasing amplitudes. (e) Fractures were sheared in two stages, each followed by the dynamic stressing protocol.

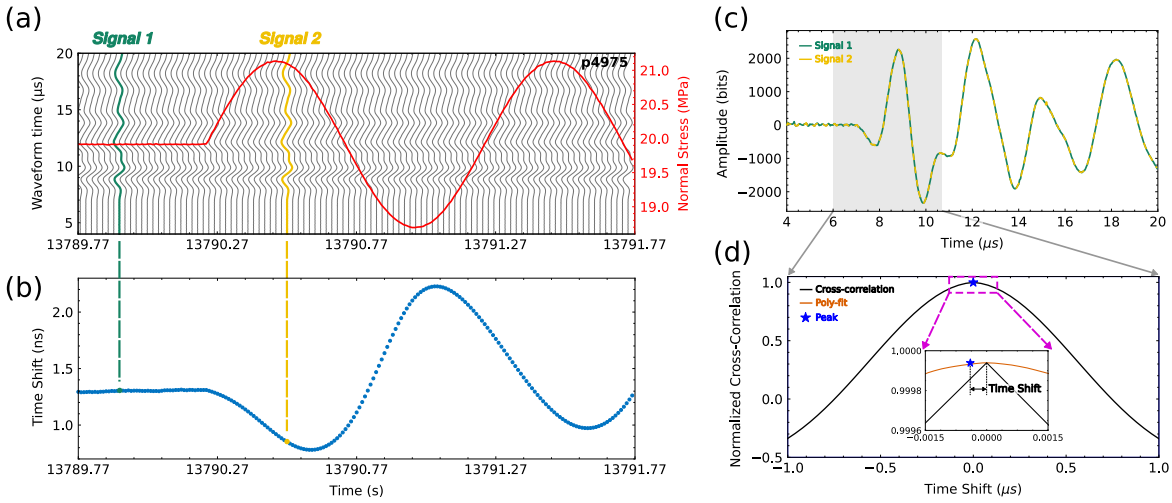



**Figure 2.4.** (a) Excerpt from Run 4 of experiment p4966 (see Fig. 3 for context in p4975) shows part of a 1 Hz, 1 MPa normal stress oscillation (red) and the concurrent raw ultrasonic waveforms (grey). The number of waveforms in the waterfall plot has been decimated for clarity. (b) Time shift was calculated by cross-correlating the waveforms with a reference waveform. (c) An example of a reference, unperturbed, waveform (green) and perturbed waveform (dashed yellow) highlights the similarity. (d) The maximum linear correlation between the reference and perturbed waveforms from cross-correlation is used to determine the time shift. The inset shows improvement of time shift calculations with a 2nd order polynomial fitting procedure.

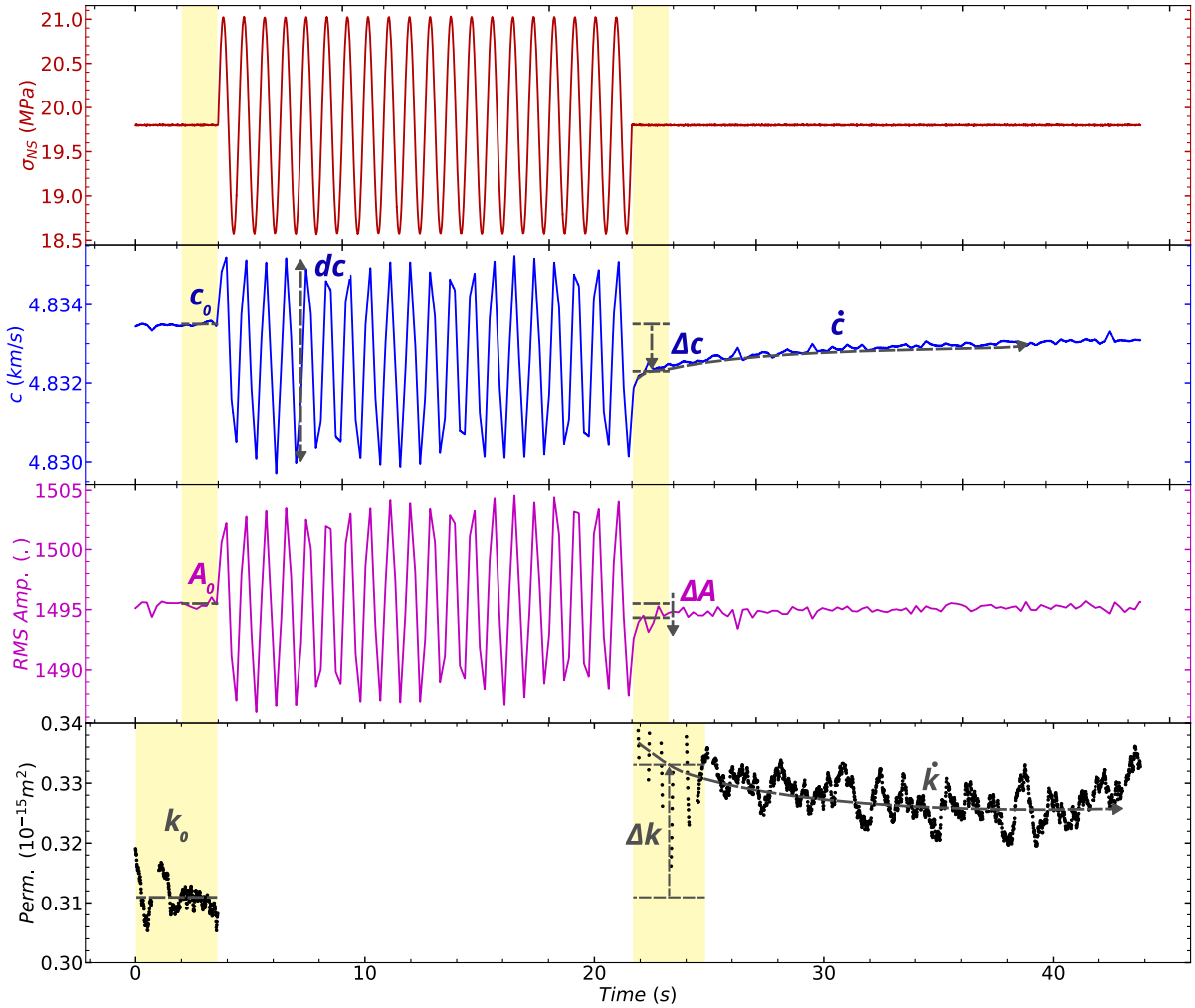



**Figure 2.5.** Details of elastodynamic and hydraulic response to dynamic stress oscillation, see Run 4 of p4975 in Fig. 3. Wave velocity and permeability changes are calculated using the measured values before and after oscillations averaged over the time windows indicated by yellow boxes. Permeability measurements are shown only for steady state flow when the inlet/outlet flow rates differ by $< 5\%$. We measure the log-time evolution in p-wave velocity ($\dot{c}$) and permeability ($\dot{k}$). The initial, pre-oscillation values ($c_0$, $A_0$, $k_0$) are averaged in a 1-s window. The changes in velocity (blue), RMS amplitude (magenta), and permeability (black), $\Delta c$, $\Delta A$, $\Delta k$, respectively, are the values after oscillation relative to the initial values. Furthermore, we measure the average change in p-wave velocity during dynamic stressing oscillations as $dc$.

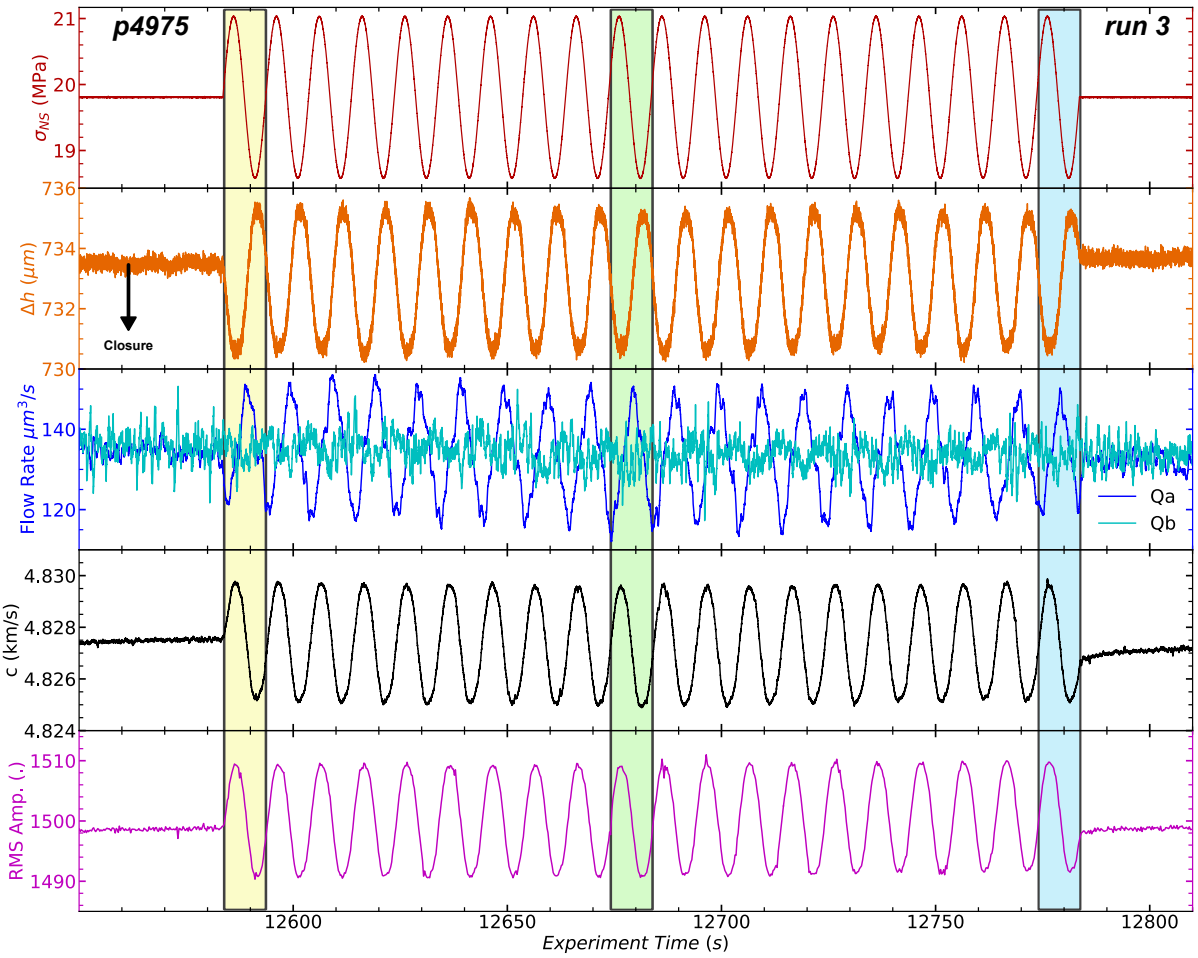



**Figure 2.6.** Elastodynamic and hydraulic data for one set of applied normal stress oscillations at a frequency of 0.1 Hz and amplitude of 1 MPa (See Fig. 3). Fracture closes initially as normal stress increases (orange trace) and then varies in phase with fracture normal stress. Fluid flow data from the fracture inlet (PpA) and outlet (PpB) document the transient response to changes in fracture flow pathways and stress state. Note that inflow is phase lagged relative to fracture dilation/closure. Elastic wave speed and amplitude are shown for the direct path pair (center transmitter to blue receiver in Figure 2). Three sections are highlighted showing one full cycle in the beginning, middle, and end of the normal stress oscillation.

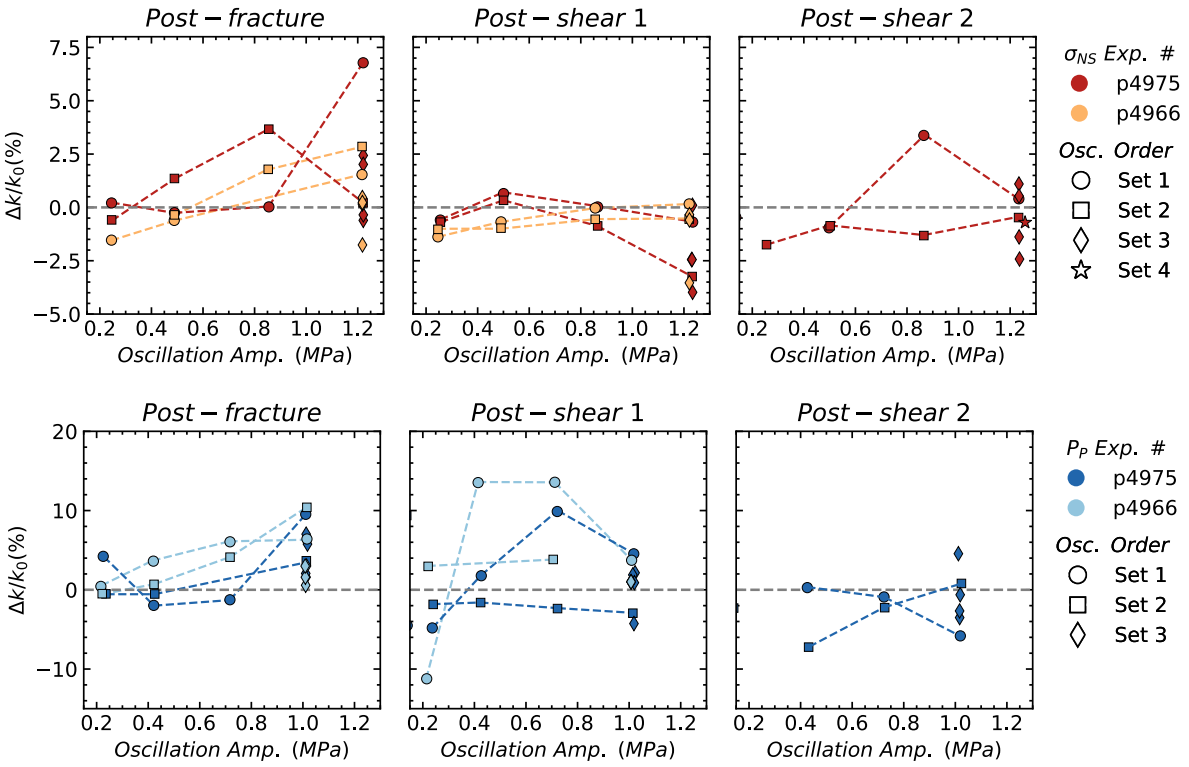



**Figure 2.7.** Relative changes in permeability for dynamic stressing via applied normal stress (top row) $\sigma_{NS}$ and pore pressure (lower row) $P_p$ at 1 Hz. Data are shown for the period just after the fracture formed (post-fracture) and after each increment of shear. Comparing post-fracture results to post-shear we observe a general reduction of permeability enhancement via dynamic stressing with smaller values of $\Delta k/k_0$. Gouge generated from shear is likely clogging flow pathways along the fracture plane. The hypothesized impediment to flow for the post-shear oscillation sets causes a reduction in permeability enhancement, especially for the post-shear 2 oscillation set.

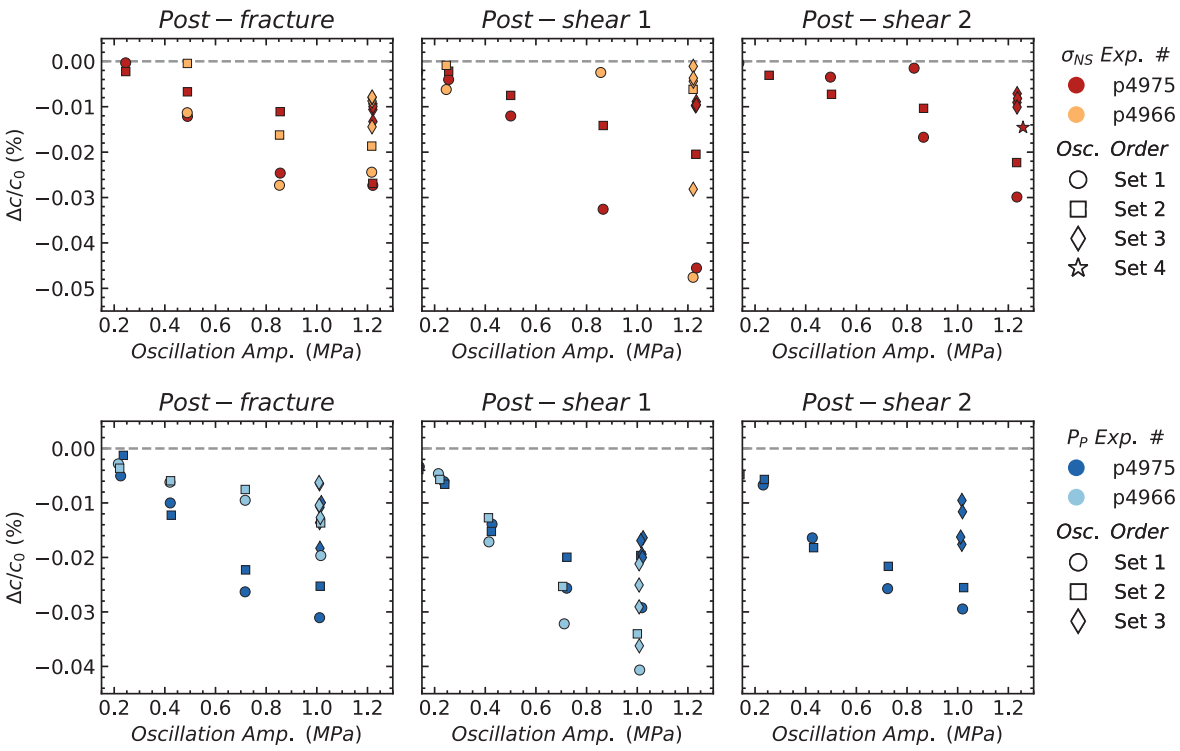



**Figure 2.8.** Relative changes in p-wave speed for dynamic stressing via applied normal stress (top row) $\sigma_{NS}$ and pore pressure (lower row) $P_p$. Data are shown for the direct transmitter-receiver pair (see Figure 2). Note that the magnitude of $\Delta c$ increases as a function of oscillation amplitude. We observe increased nonlinearity (absolute value of $\Delta c/c_0$) in some cases after the first shear displacement, but then observe a minor reduction for both normal stress and pore pressure oscillations after the second shear displacement.

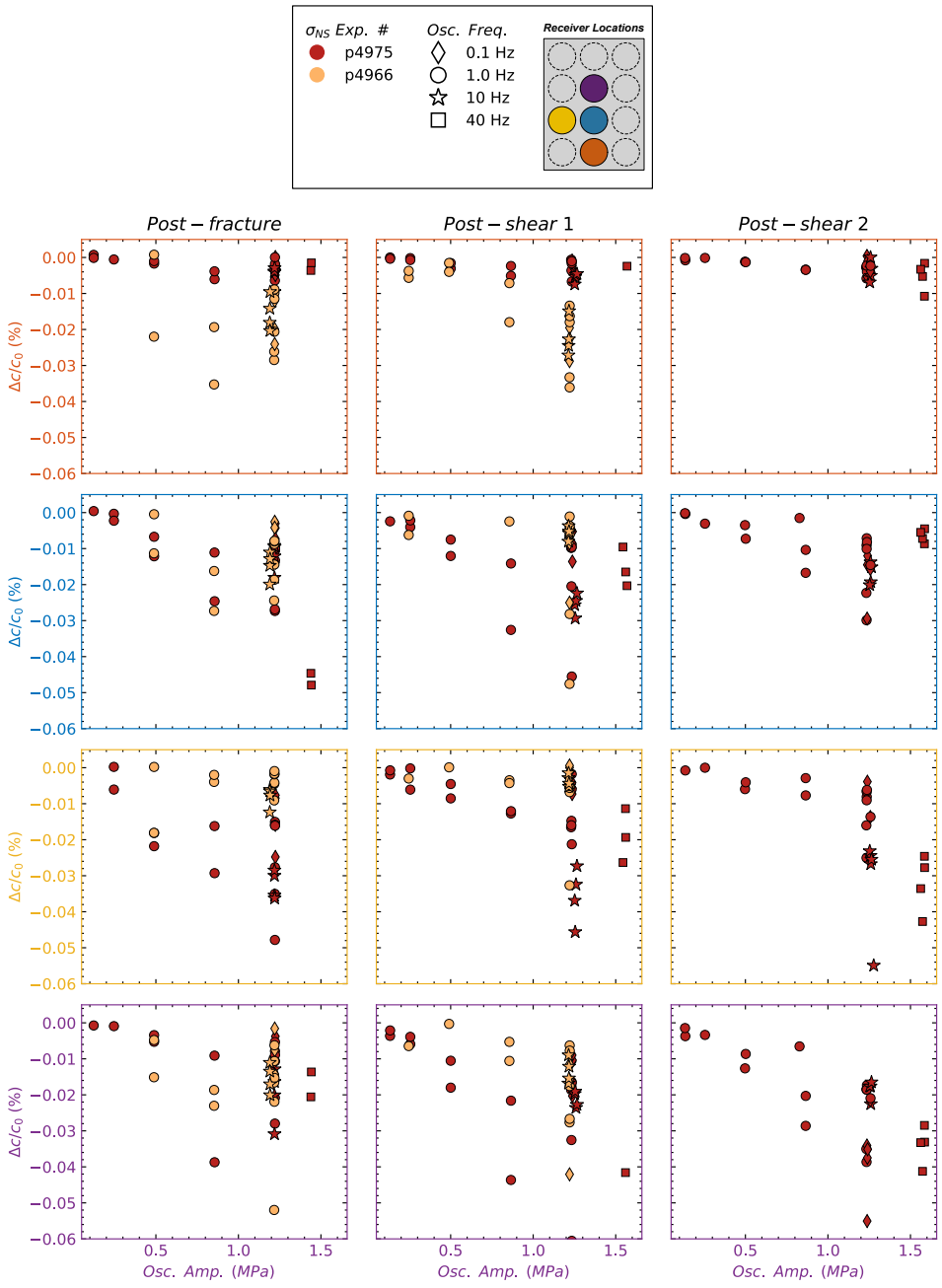



**Figure 2.9.** Nonlinearity as a function of $\sigma_{NS}$ oscillation amplitude for each receiver. Transitioning from post-fracture results to post-shear results, we observe decreasing nonlinearity. The plot colors correspond to PZT receiver locations. These results demonstrate the spatial variability in nonlinear elasticity across the fracture plane and furthermore shows that the two Westerly granite samples exhibit similar magnitude of nonlinearity ($\Delta c/c_0$) with normal stress oscillations.

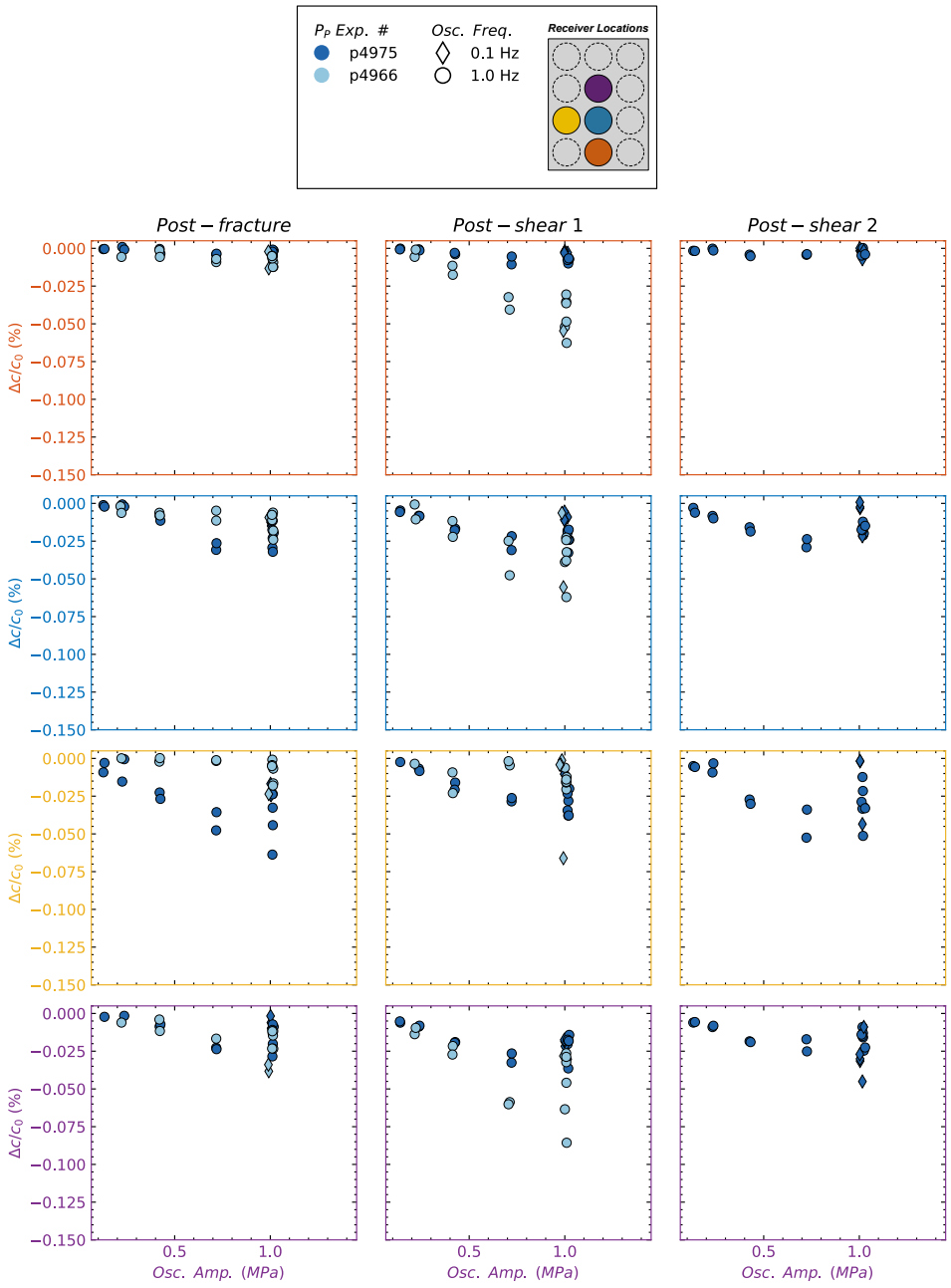



**Figure 2.10.** Nonlinearity as a function of pore pressure oscillation amplitude for each receiver. Transitioning from post-fracture results to post-shear results, we observe decreased nonlinearity. The spatial variability shows that the pore pressure oscillations in some of the receiver locations throughout the experiments cause larger changes in elastic nonlinearity than the normal stress oscillations.

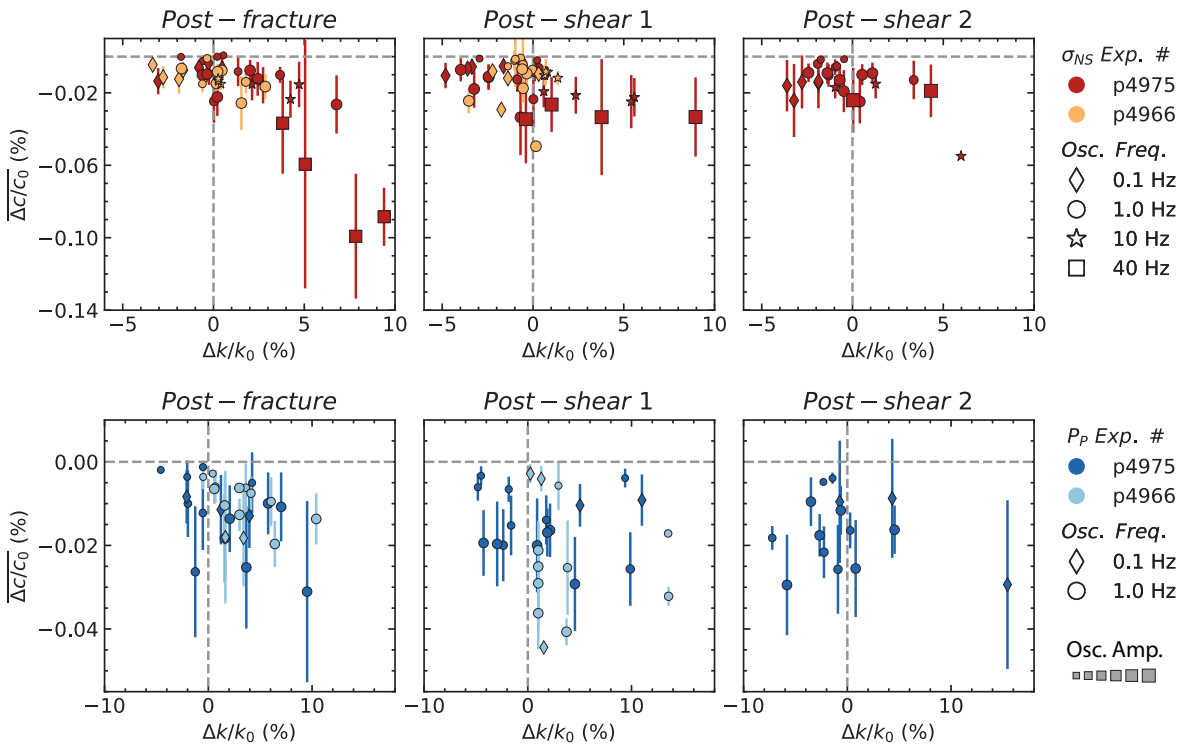



**Figure 2.11.** Nonlinearity as a function of permeability change for $\sigma_{NS}$ and $P_P$ oscillations averaged over all receivers. Data point shapes correspond to the oscillation frequencies and their sizes to amplitude. In post-fracture oscillation sets, relative changes in permeability and wave velocity are correlated. That is to say, larger normal stress or pore pressure oscillation amplitude and frequencies produce larger transient softening and permeability enhancement. Overall, shear weakens this relationship, reducing the amount of nonlinearity and permeability enhancement for both methods of dynamic stressing.

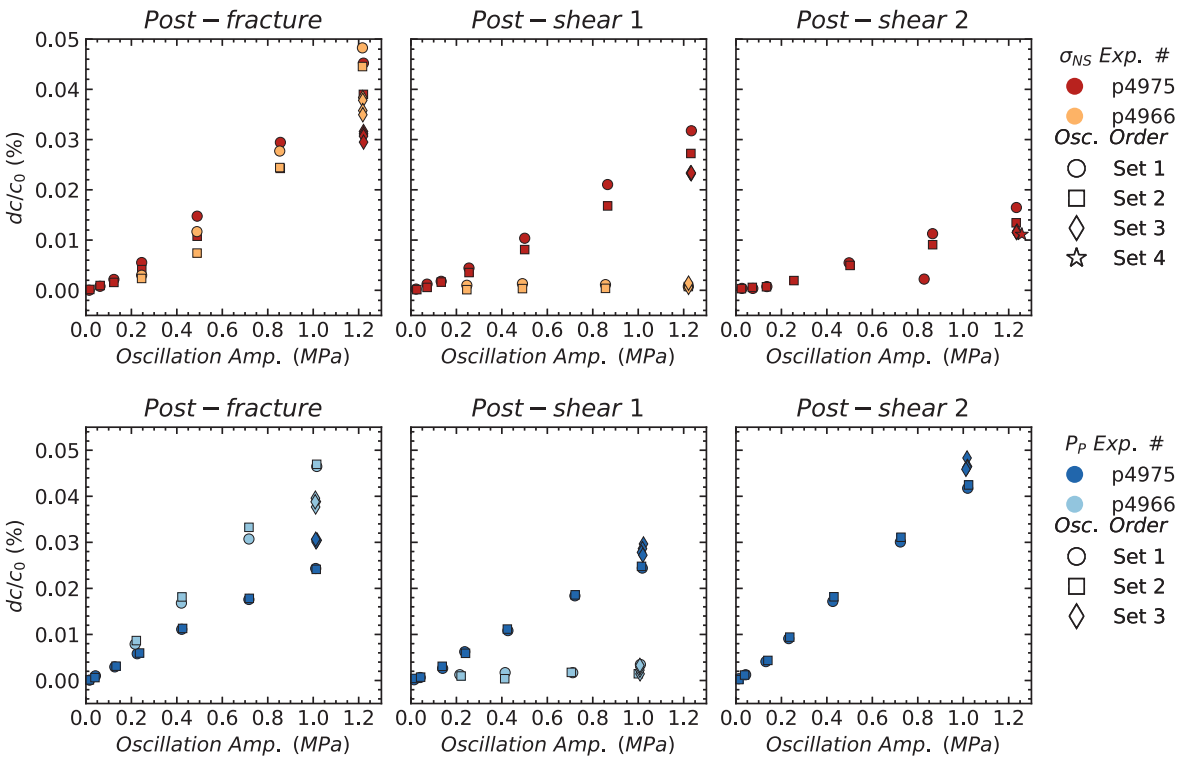



**Figure 2.12.** Velocity amplitude modulation averaged over all receivers ($dc/c_0$) as a function of normal stress and Pore pressure oscillations. There is a systematic reduction in $dc/c_0$ with accumulated shear for normal stress oscillations and there is very little variation in the oscillation order. The results from pore pressure oscillations in p4966 tell a similar story as the normal stress oscillations, but the pore pressure oscillations in p4975 show no change from post-fracture to post-shear 1 and an increase in $dc/c_0$ from post-shear 1 to 2.

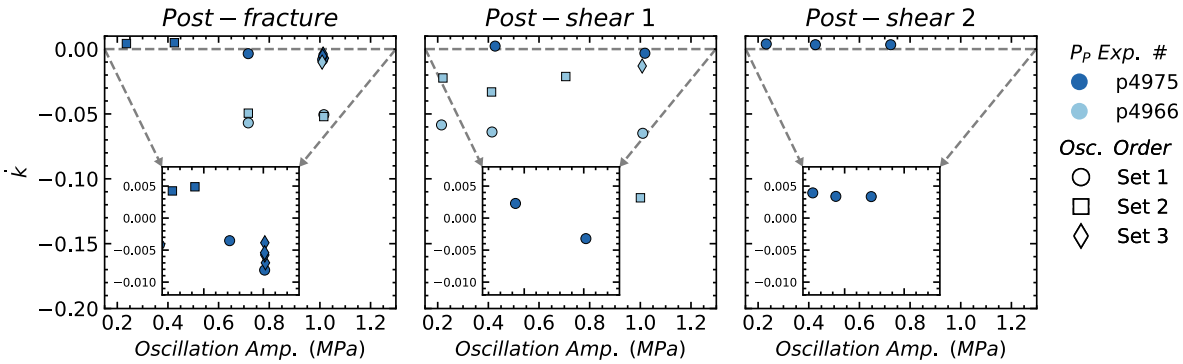



**Figure 2.13.** Permeability recovery $\dot{k}$ as a function of applied stress oscillations for $P_P$. Data point shapes indicate oscillation order. Recovery rate $\dot{k}$ linearly decreases with $P_P$ oscillation amplitude in p4975 and subsequent shearing results in slower $\dot{k}$ for $P_P$ oscillations.

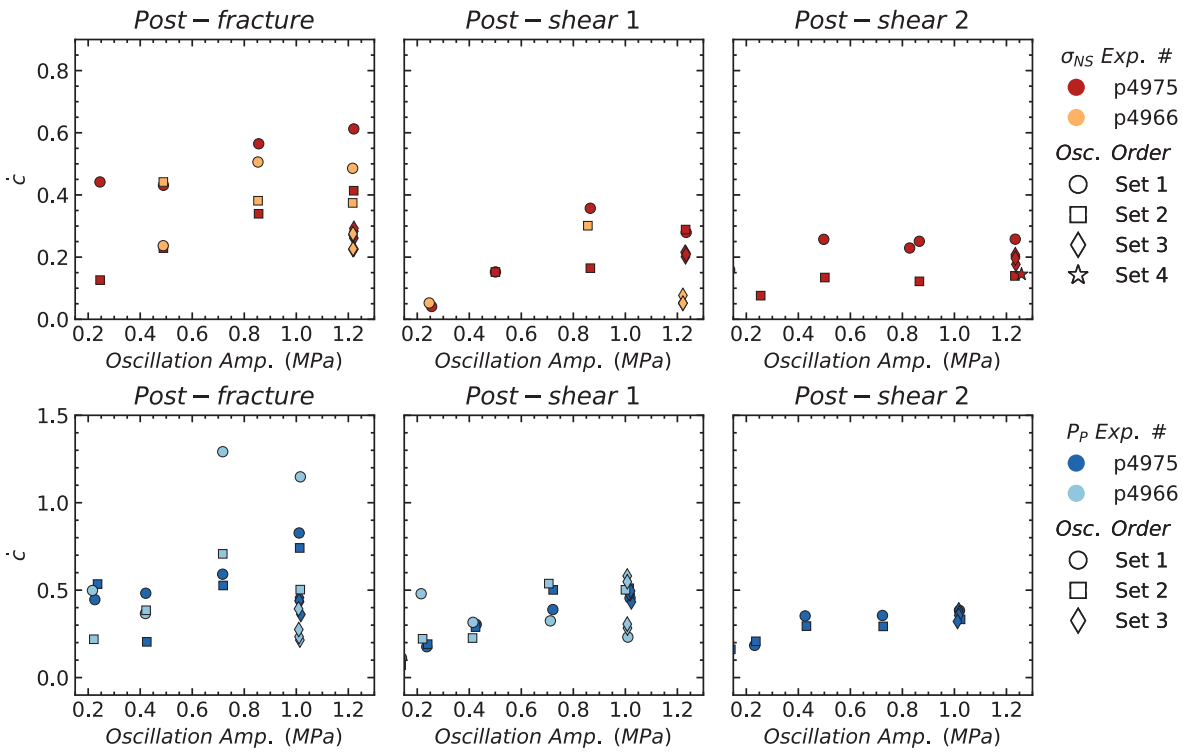



**Figure 2.14.** Wave velocity recovery $\dot{c}$ for direct-path receiver as a function of applied stress oscillations for $\sigma_{NS}$ and $P_P$. Data point shapes represent oscillation order. The recovery rate $\dot{c}$ modestly increases with both $\sigma_{NS}$ and $P_P$. Shearing decreases $\dot{c}$ and flattens after the second shear displacement.

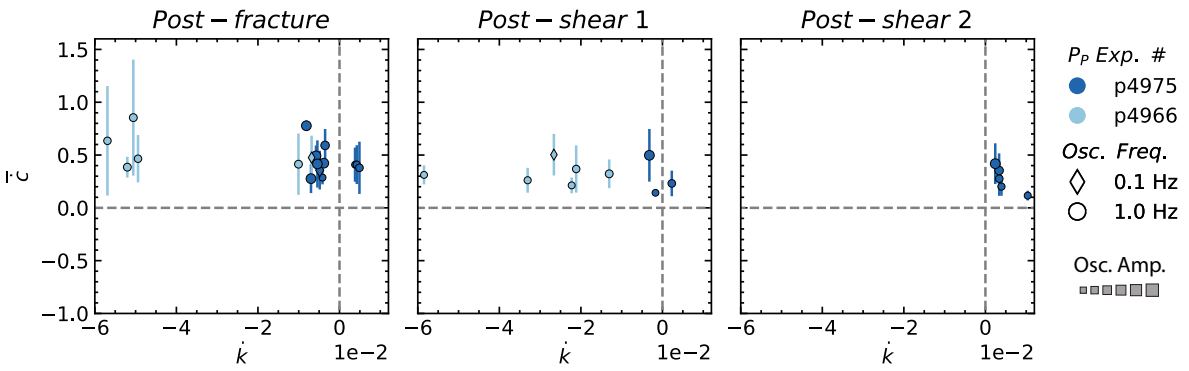



**Figure 2.15.** Average wave velocity recovery rate $\dot{\bar{c}}$ as a function of permeability recovery rate $\dot{k}$ for $P_P$ oscillations averaged over all receivers. Data symbol shapes correspond to the oscillation frequencies and their sizes to amplitude. In post-fracture oscillation sets, both high frequency and large amplitude oscillations yield faster recovery rates for both velocity and permeability. The predominant effect of shearing is an increase in $\dot{k}$ for $P_P$ oscillations.

# Chapter 3

## Relating hydro-mechanical and elastodynamic properties of dynamically-stressed tensile-fractured rock in relation to applied normal stress, fracture aperture, and contact area

### 3.1 Abstract

We exploit nonlinear elastodynamic properties of fractured rock to probe the micro-scale mechanics of fractures and understand the relation between fluid transport and fracture aperture and area under dynamic stressing. Experiments are conducted on rough, tensile-fractured Westerly granite specimen subject to triaxial stresses. Fracture permeability is measured from steady-state fluid flow with deionized water. Pore pressure oscillations are applied at amplitudes ranging from 0.2 to 1 MPa at 1 Hz frequency. During dynamic stressing we transmit ultrasonic signals through the fracture using an array of piezoelectric transducers (PZTs) to monitor the evolution of interface properties. We examine the influence of fracture aperture and contact area by conducting measurements at effective normal stresses of 10 to 20 MPa. Additionally, the evolution of contact area with stress is characterized using pressure sensitive film. These experiments are conducted separately with the same fracture and they map contact area at stresses from 9 to 21 MPa. The resulting 'true' area of contact measurements are made

for the entire fracture surface and within the calculated PZT sensor footprints, from numerical modeling of Fresnel zone. We compare the elastodynamic response of the fracture using the stress-induced changes in ultrasonic wave velocities for transmitter-receiver pairs to image spatial variations in contact properties. We show that nonlinear elasticity and permeability enhancement decrease with increasing normal stress. Additionally, post-oscillation wave velocity and permeability exhibit quick recoveries toward pre-oscillation values. Estimates of fracture contact area (global and local) demonstrate that the elastodynamic and permeability responses are dominated by fracture topology.

## 3.2 Introduction

Dynamic perturbations in the subsurface, regardless of their origin, are associated with critical observations of changes in poromechamical properties. These perturbations can be broadly categorized as "fluid-induced" or "strain-induced" and manifest similar phenomenological observations. For example, pumping of wastewater or carbon for storage purposes or hydrocarbon recovery perturb the stress state of the subsurface and can accelerate deformation, reactivate faults (inducing seismicity), or damage reservoir seals [42, 70, 71, 88, 110, 111, 119]. Also, fault stability may even be perturbed by elastic waves propagating from earthquakes [9,54,99] thus triggering seismicity [15,117]. This is often observed with co-seismic velocity variation, or "elastic softening", typically in the shallow crust [12–14, 25, 33, 46, 62, 63, 77, 122, 127]. This co-seismic softening, an instantaneous wave speed change (typically a decrease), is then followed by a time-logarithmic post-seismic recovery of the fractured rock stiffness e.g., [12, 78].

Experimental and field studies have use seismic wave velocity and attenuation to estimate fracture stiffness [65, 85]. These and other observations demonstrate that fracture topology, and its changes with stress, is central to the poromechanical response [17, 18, 81, 137]. Other experimental studies have investigated the changes in

elastic properties of faults during shear [57], usually with some amount of gouge or wear product. Other studies has demonstrated, with similar monitoring techniques, the relation between wave speed and amplitude and the following: contact area (evolution) [133], gouge layer dilation [56, 103], degree of surrounding bulk damage [108], and stress state [78]. In the work of [78], it was demonstrated in quasi-static experiments that elastic stresses in bulk rock exert significant control on transmitted wave velocity, but near-fault properties strongly influenced transmitted wave amplitude (attenuation). All of these studies provide rich information regarding the role of discontinuities in rocks and the role their topology plays in deformation (stress distribution) and fluid flow. However, these observations of planar, rough fractures are not necessarily indicative of their poro-elastic response under dynamic conditions (strain). Recently, dynamic acousto-elastic testing (DAET) has been used to study the nonlinear elastodynamic response of fractured rock under different stress and saturation conditions [67, 68]. In these studies, the nonlinear elastic responses can be activated with dynamic strains on the order of $10^{-6}$ [41, 55, 93]. The nonlinear elastodynamic behavior of rock, intact or fractured, is modulated by minute features such as apertures (governing flow transport, asperity compliance) and higher-order effects such as nonlinear effective stiffness (impacted by rate and state-dependent friction and healing). Laboratory experiments implementing DAET [67, 68, 94, 106, 126], show that transmitted ultrasonic wave velocity decreases in response to stress oscillations followed by a time logarithmic recovery, similar to the aforementioned field observations.

In the context of subsurface storage and energy recovery, dynamic stressing can result in permeability enhancement or reduction. Elastic waves from earthquakes may also induce pore pressure oscillations sufficiently large to change permeability [15, 66]. The underlying mechanism dominating empirical observations of permeability enhancement (and reduction) is postulated to be mobilizing and arresting of particles in porous media

[20, 21, 30, 64, 95, 96]. This effect of clogging and unclogging of pore throats has been observed experimentally [20,30], but the relation between these observations and elastic properties of fractured rock is not well understood. Other mechanisms could account for the changes in transmissivity of rough fractures such as: fracture orientation to flow [73], evolution of fracture geometry (i.e. roughness, contact area) [1, 137].

The similar poromechanical responses (permeability change and elastic softening) of faults and fractured rock to dynamic stressing sources indicate that these mechanisms – stiffness and fluid transport – are correlated [5–7, 17, 28, 35, 40, 47, 86, 124, 128, 137], much like the connection under static conditions [69, 75, 81, 83]. In this work we seek to decouple the nonlinear elastic and fluid flow responses to dynamic stressing under different applied normal stresses. To address this, we perform laboratory experiments on a tensile-fractured specimen of Westerly granite, where pore pressure perturbations were applied at different applied stress states. An array of cross-fracture ultrasonic sensors and through-fracture fluid flow measurements allow us to characterize the elastodynamic and permeability responses to the pore pressure oscillations. A unique contribution of this study is relating the nonlinear elastic and fluid flow changes to fracture contact area with the implementation of pressure sensitive films. This allows us to connect the inherent spatial variability of fracture geometry to applied stress state and the variability of observed nonlinear elasticity (for respective ultrasonic sensor locations).

## 3.3 Experimental Setup

We conducted a series of highly-constrained laboratory experiments on a pre-fractured sample of Westerly granite. For the first experiment (p5483), nonlinear elastic properties and flow rates were simultaneously measured under true triaxial stresses. Another experiment (p5596) was conducted to estimate the real area of contact of the fracture as a function of applied normal stress.

The sample was cut into a L-shaped block 69 x 45 x 50 x 26 mm (Figure 3.1a-b) that we grooved along the perimeter and split in Mode I over a knife-edge to create a rough quasi-planar fracture. The pre-fractured sample was re-mated, placed between two loading platens, and then sealed with a latex membrane (separating pore fluid from confining fluid). The steel loading platens include piezoelectric transducers (PZTs) embedded 3 mm from the on-rock faces as well as internal conduits to provide a distributed line source of fluid at both ends of the fracture, Figure 3.1b (using a modified version of the method of [30]).

After placing the sample between steel loading platens, it was sealed inside a latex membrane, and then placed inside a pressure vessel, Figure 3.1b-c; more details regarding sample preparation can be found in [67, 105, 126]. Leveling blocks below the bottom faces of the loading platens act to minimize tilting during the application of normal stress. Each loading axis is independently servo-controlled, including upstream and downstream fluid flow from pressure intensifiers. Mechanical displacements and stresses are measured with direct current displacement transducers (Trans-Tek Series 240 DCDT) as well as custom-built load cells and recorded by a 24-bit analog-to-digital data acquisition system at 100 Hz. Active source ultrasonic monitoring was conducted using a Vantage$^{TM}$ Research Ultrasound (Verasonics) system and PZTs (APC International Ltd. 6.35 mm diameter compressional crystals) with a nominal center frequency of 500 kHz. PZTs are adhered to the steel loading blocks with conductive epoxy and back-filled with sealant epoxy. The transmitting PZTs were successively pulsed every 0.2 ms and the ultrasonic response is recorded at the receiving PZTs at 25 MHz. A triggering signal from the Verasonics system is also recorded by the mechanical data acquisition system, allowing data synchronization. More details for the data acquisition are found in [67, 105, 126].

### 3.3.1 Experimental Procedure

After sample preparation and installation into the pressure vessel, the experiment commenced with the application of a normal stress of $\sim$ 10 MPa followed by a confining pressure of $\sim$ 5 MPa. Next, the inlet ($P_{pA}$ = 2.5 MPa) and outlet ($P_{pB}$ = 1.5 MPa) pressures were applied to provide a pressure differential across the sample, Figure 3.1. The large difference in confining and pore fluid pressures prevents fluid from flowing around the outside of the sample and/or along the grooved contour around the sample (used during tensile fracture). Pore pressure oscillations were applied via servo control by feeding a sinusoidal command signal to the inlet pressure intensifier $P_{pA}$. $P_{pA}$ stress oscillations ranged in amplitude from 0.2 to 1 MPa at 1 Hz while holding $P_{pB}$ constant, Figure 3.1d. All oscillations throughout the experiment are composed of 20 cycles, which allows for direct comparison in this experiment and to other studies [67, 105, 126]. The first pore pressure oscillation set is preceded by a normal stress oscillation set, which is used in the analysis of [67], and can be seen in the effective normal stress plot in Figure 3.1d. Afterward, the effective stress state was increased for a total of 5 different stress levels [10, 12.5, 15, 17.5, 20] MPa. Due to operational constraints, the effective stress state was decreased to $\sim$1 MPa and held over several hours, before resuming the experiment at 17.5 MPa. Three sets of pore pressure oscillations of varying amplitudes were repeated three times at each normal stress level when stresses were incremented and four sets when decremented, Figure 3.1d - e. The decremental stress levels, [17.5, 15, 12.5, 10] MPa, were conducted in order immediately proceeding largest stress, 20 MPa, and with an hour hold at 12.5 MPa. This protocol is designed to investigate the repeatability of measurements and to determine the effect, if any, of loading and unloading on the fracture properties (elastic nonlinearity, permeability).

### 3.3.2 Steady-state Permeability Measurements

Independent measurements of volumetric inflow ($Q_A$) and outflow ($Q_B$) rates are made using Linear Variable Differential Transformers (LVDTs) attached to the pistons of the pressure intensifiers. Our flow rate measurements are continuous, but we only consider data for near-steady flow conditions ($Q_A - Q_B \leq 5\%$). Darcy's law is used to calculate permeability $k$:

$$k = \frac{\mu L \, Q}{A \Delta P_P} \tag{3.1}$$

where $Q = \frac{1}{2}(Q_A + Q_B)$ is the average flow rate, $\mu$ is the fluid viscosity ($10^{-3}$ Pa·s) at 20° C, $L$ is the length of the flow path along the fracture plane (50 mm) and $A$ is the cross-sectional area perpendicular to the flow path (45 mm × 26 mm), which includes both the fracture and granite wall rock. This gives a measure of permeability of the fracture, assuming the surrounding rock matrix is several orders of magnitude smaller ($k \sim 10^{-21}$ m$^2$) and is therefore a negligible contribution to our analysis, even with increasing stress conditions. The permeability could also be calculated using other valid approaches [50, 134] which isolate the fracture permeability, but our focus here is on relative *changes* in permeability dominated by the stress-sensitive fracture.

### 3.3.3 Dynamic Permeability Measurements

In addition to measuring the steady-state permeability before and after oscillations, we use the flow-analysis technique as described in [112] to calculate the "dynamic" permeability, $\hat{k}$, during the pore pressure oscillations. The frequency of the imposed pore pressure oscillations, 1 Hz, is sufficiently fast enough to be nonsteady-state (i.e. $Q_A \neq Q_B$). The following equation is employed to quantify the permeability during

non-Darcian flow conditions:

$$\hat{\delta}_Q = \left| \frac{Q_A(t)}{P_A(t)} \right| = \frac{1}{2} \left| \frac{(1-i)\sqrt{\hat{\eta}\hat{\xi}} \sinh\left[(1+i)\sqrt{\hat{\xi}/\hat{\eta}}\right]}{\cosh\left[(1+i)\sqrt{\hat{\xi}/\hat{\eta}}\right]} \right|, \tag{3.2}$$

where $\hat{\eta} = (AT\hat{k}/\pi\mu L)$ and $\hat{\xi} = AL\hat{s}$. Here, $T$, $\hat{k}$, and $\hat{s}$ are the oscillation period (1 s), dynamic permeability, and hydraulic storage, respectively. This analytical expression is the solution to harmonic flow through a porous medium via diffusion. The hydraulic parameter $\hat{\delta}_Q$ is the ratio between imposed upstream pore press ($P_A$) and the resulting fluid flux $Q_A$, measured by LVDTs attached to the pressure intensifier pistons. Both the dynamic permeability, $\hat{k}$, and hydraulic storage, $\hat{s}$, are calculated from a least-squares minimization between the measured hydraulic parameter $\hat{\delta}_{Q\text{exp}}$ and the analytically calculated $\hat{\delta}_Q(\hat{k}, \hat{s})$:

$$(\hat{\mathbf{k}}, \hat{\mathbf{s}})_{\text{opt}} = \underset{\hat{\mathbf{k}},\hat{\mathbf{s}}}{\text{argmin}} \sqrt{\left| \hat{\delta}^2_{Q\text{exp}} - \hat{\delta}^2_Q(\hat{\mathbf{k}}, \hat{\mathbf{s}}) \right|}. \tag{3.3}$$

In subsequent sections, we report results of dynamic permeability, $\hat{k}$, under different stress conditions and in relation to active source ultrasonic measurements during oscillations.

## 3.4 Active Source Ultrasonic Measurements

Active source ultrasonic data are continuously recorded before, during and after the pore pressure oscillations. P-wave, transmitting PZTs are successively excited with half-sine pulses at 96 V having a center frequency of 500 kHz. Having an array of transmitters and receivers allows us to capture the spatial variability of the fracture's elastodynamic properties (i.e., wave speed and amplitude). Various limitations prevented the use of all possible transmitter-receiver pairs; we report the results from 7 transmitter-receivers

pairs.

The ultrasonic data are processed as previously documented [67, 92, 126], where all waveforms are cross-correlated with a reference waveform (constructed by averaging 50 recorded waveforms at the beginning of each experimental run before stress oscillations) to determine a time shift. Since the time shift is typically smaller than the signals' sampling time, often on the order of 1 ns, the resolution is improved with a second-order polynomial fit to the peak of the cross-correlation function [24]. Figure B.1 shows the raw waveforms for one transmitter-receiver pair during a 1 MPa amplitude pore pressure oscillation, which highlights minute changes we are able to measure. The absolute arrival time is obtained by adding the relative time shift to the p-wave arrival time of the reference waveform (obtained using a threshold). To obtain (corrected) p-wave wave speed, the sample thickness (corrected for compaction/dilation from internal DCDT which has $\pm$ 0.1 µm resolution) is divided by the absolute arrival times. The RMS amplitude is calculated over an approximately 10 µs time window including the p-wave arrival and one full period of the waveforms. Additionally, as part of a previous study [67], tests were conducted using a stainless steel specimen (of same dimensions) and concluded that the nonlinearity of the entire experimental apparatus is negligible compared to the nonlinearity measured in intact and fractured rock samples.

### 3.4.1 Fresnel Zone Imaging

A key aim of this study is relating p-wave velocity and permeability changes to changes in the fracture contact area. To accomplish this, we need to determine the size of the fractured region probed by a given ultrasonic transmitter-receiver pair in our experimental configuration. It is common to implement ray theory approximations of acoustic wave propagation for active-source monitoring, that connects changes in wave velocity and amplitude to changes in experimental fault contact area [43, 109], for example. In

this approximation, waves propagating from source to receiver are considered to be in the high-frequency limit and thus the wavefield is collapsed into a ray path approximated as an infinitesimally thin line [113]. In reality, elastic waves propagate within a finite volume whose width is frequency-dependent, rather than the volumeless trajectory of a ray path. The region around the propagation trajectory responsible for diffraction in a medium is called the Fresnel zone or Fresnel volume. The region around a ray that mostly influences the propagation of a band-limited wave is called the first Fresnel zone. Previous studies estimated the ellipsoidal Fresnel volume for active-source monitoring [135] by assuming point sources for transmitters and receivers, which may underestimate the region or volume probed by finite-sized transducers.

Here, we numerically model the Fresnel zone resulting from our finite-sized transmitter-receiver PZTs through the bulk rock sample using a sensitivity kernel (SK) to later estimate perturbations in the wavefield amplitude arising from heterogeneities at the fracture interface. The SK also provides insight on how other types of diffractors, i.e. wave speed or density, affect acoustic wave propagation [97]. The SK in Figure 3.3b shows the variation in transmitted wave field amplitude, where red colors indicate increased amplitude and blue colors correspond to reduced relative amplitude (from scattering). It is important to note that in our model we treat our transmitter and receiver as a collection of point sources and consequently the Fresnel zone is a superposition of their respective wavefields. The relative transmitted wave amplitude sensitivity kernel along the fracture profile is shown in Figure 3.3c, where the width of the half-power bandwidth of the first Fresnel zone (blue) is delineated by dashed gray lines. For a given transducer pair, we consider this region within the Fresnel zone to substantially contribute to the recorded changes in transmission characteristics along the transmitter-receiver travel path.

## 3.5 Fracture Contact Characterization

After conducting the dynamic stressing experiment described above, we conducted an additional multi-step experiment to characterize the real area of contact for the tensile fracture specimen under load. This was accomplished by inserting Fuji Prescale© Medium Film (9.7 –49 MPa) between the two halves of the fracture and loading the specimen to a range of stresses. The pressure sensitive film is a $\sim$ 100 µm thick plastic film containing capsules that rupture and react with an agent to produce the magenta color (Figure 3.2b when a sufficient force is applied, $>$ 9.7 MPa. The spatial resolution is 5 µm, which corresponds to approximately $\pm$1.5 Pa stress resolution [104]. Mating the fracture repeatably is imperative for the integrity of the asperities and also for accurate registration of contacts and voids. To that end, we installed locating pins to ensure that the fracture closed consistently each time and that the films were located precisely relative to one another. The pins were installed by drilling two 1.588 mm diameter through-holes in the shorter sample half and blind holes in the taller half such that the locating pins could be inserted to ensure alignment (Figure 3.2a). A blank pressure sensitive film was cut to size and then inserted between the two fracture halves before loading to the desired target stress. This procedure was repeated with a new pressure sensitive film for each stress ranging from 9 to 21 MPa in increments of 1 MPa. Figure 3.2b depicts a representative pressure sensitive film loaded to 20 MPa; magenta color corresponds to regions of the fracture interface in contact and the remaining areas are void space. The pressure sensitive films are digitized using a Epson Perfection 3200 Photo color scanner at 3200 dpi resolution. Digitized scans are aligned using cross-correlation (with the lowest stress, 9 MPa, as the reference) and then binarized using an algorithm that generates a threshold value based on mean pixel intensity. Figure 3.2c shows an overlay of the fracture contacts (shades of blue) for 10, 15, and 20 MPa (data

from experiment p5596).

## 3.6 Results

Our data include measurements of fracture permeability, p-wave velocity and fracture contact area. The transducer array and pressure sensitive film provide information on the spatial variability of fracture properties and its evolution during dynamic stressing. We integrate that data with fluid flow measurements to develop a detailed understanding of fracture properties.

### 3.6.1 Static Hydraulic and Elastic Responses

We quantify the overall linear elastic and hydraulic changes in responses to static loads. In Figure 3.4a, compaction, $\delta$, is measured during the beginning of each effective stress level for both the loading and unloading phases of the experiment. We observe fracture closure (positive) from 10 to 15 MPa, and then this trend changes, most likely in response to unloading the sample and holding at $\sim$ 2 MPa for several hours and then subsequent reloading of the specimen to 17 MPa. Despite this long hold time, there is a small effect on the stress-displacement relationship. During the unloading portion, the fracture aperture opens nearly linearly with decreasing stress. Overall, there is minor hysteresis at 10 MPa and minimal on-fault compaction. This is supported by our observations in Figure B.3, which shows the effective stress as a function of on-fault displacement for experiment p5483. This, along with the stress-displacement curves in Figure B.2, demonstrates that our observations are repeatable and that fracture misalignment is minimal and not dominating the overall elastic deformation. Figure 3.4b shows the evolution of static permeability, $k$, with increasing and decreasing effective stress. Static permeability decreases non-monotonically with increasing stress and is nearly invariant with decreasing effective stress. Interestingly, there is more hysteresis present compared

to on-fault displacement, but the ending permeability measurement is within 30% of the minimum starting value.

### 3.6.2 Connecting Sensor Footprint and Contact Area

A crucial component to this study is connecting fracture contacts to the active-source monitoring data. We estimate the real fracture contact area probed by each transmitter-receiver pair by superimposing the calculated PZT footprints (Section 3.4.1) onto the digitized and binarized pressure sensitive films. Figure 3.2d shows an example of fracture contacts (black indicates regions of contact and white indicates void) with locations and sizes of sensor footprints highlighted. This demonstrates the highly variable spatial distribution of contacts across the fracture. Additionally, the estimated total area of contact as a function of applied stress is shown in Figure 3.2e. The dashed red line shows a cubic fit to these data, suggesting a Hertzian-contact relation between real contact area (from pressure sensitive films) and nominal applied stress [45]. Furthermore, we quantify the change in real contact area within PZT footprints with stress, see Figure 3.5, with respective dashed lines are cubic fits. As expected, the contact area within each PZT footprint generally increases with stress with a few exceptions, possibly due to the inevitable variations in mating of the two fracture surfaces at each stress level. A comparison between the regions probed by sensors highlighted with dark green (top right) and light orange (bottom left) illustrate the disparity of contact area. The relation between these results and nonlinear elastodynamic measurements are detailed in the Discussion section. The measured contact area (Figures 3.2d and 3.5) is consistent with previous studies using similar contact registration methods [76] and rough surfaces [115] to quantify stress-contact area relationships, with approximately 10 % area in contact at 10 MPa applied normal stress.

### 3.6.3 Hydraulic and Nonlinear Elastodynamic Responses

Rocks exhibit nonlinear elastic behavior due to the nonlinear response of their constituent minerals and structures, namely, microcracks and compliant grain boundaries [41,93]. When rocks are fractured, as in nature, this nonlinearity is compounded by contact acoustic nonlinearity (CAN) at fractured interfaces. Figure 3.6 shows characteristic responses to dynamic pore fluid pressurization upstream (blue) where transient softening and modulation of baseline velocity [92] are manifest with slow recoveries to the pre-oscillation condition. In comparison, a linear elastic response would be effectively stress invariant, not showing any of the aforementioned characteristics. Thus, nonlinear elasticity reveals much about the rock micro-structure, fractures, and inter-grain contacts [41], all of which also modulate the hydraulic properties. Both fluid and acoustic transmission characteristics are highly sensitive to pore/fracture apertures and contact condition. Thus, we seek to link the effect of stress state and resulting fracture aperture and contact to the elastodynamic and hydraulic properties of dynamically-stressed fractured rock. The nonlinear elastic response to dynamic stressing is characterized by the following: (1) relative change in wave velocity, $R_0 = \Delta c/c_0$, (2) the wave velocity amplitude modulation $R_1$, and (3) the evolution of slow dynamics or post-oscillation recovery of wave velocity $c_r$. Both $R_0$ and $R_1$ are extracted using a projection procedure following [92]. The long-term recovery, or slow dynamics, is observed to be logarithmic in time [106,107,116] and is recorded in a 90 s window following each oscillation, although the time to full recovery may be much longer [106]. Besides the nonlinear elastodynamic measures described above, the relative stress-induced change in permeability $\Delta k/k_0$ and log-time recovery $k_r$ are quantified, as noted in the permeability subplot of Figure 3.6.

### 3.6.4 Dynamic Stress-induced Changes in Permeability

The relation between relative change in permeability ($\Delta k/k_0$) and pore pressure ($P_{pA}$) oscillation amplitude for each effective normal stress ($\sigma_{\text{eff}}$) ranging from 10 MPa to 20 MPa in 2.5 MPa increments is shown in Figure 3.7a. All oscillations were applied with the same frequency of 1 Hz to allow direct comparison. As expected [105, 126], we observe increasing permeability enhancement with increasing amplitude of the applied pore pressure oscillation, though, in some cases this reaches a plateau. Additionally, the scaling between $\Delta k/k_0$ and oscillation amplitude (least-squares fit) varies with the stress state of the fracture, generally decreasing with increasing stress and assumed greater fracture closure, Figure 3.7b. This relationship is nearly monotonically decreasing with applied stress except for the increase in $\varphi$ from 15 to 17.5 MPa. Though the overall permeability (Figure 3.4b) is not sensitive to the long hold after 15 MPa, perhaps the relative change in permeability is very sensitive to minute changes in fracture mating or indentation creep [27].

The dynamic permeability, $\hat{k}$, calculated using equations 3.2 and 3.3, is a measure of permeability during oscillations, when flow is non-Darcian. As with permeability, $k$, we observe that $\hat{k}$ monotonically increases with pore pressure amplitude, Figure 3.8a. Whereas, $k$ is a measure of a transient response, $\hat{k}$ corresponds to the actuation of the fracture aperture, flow pathways, during oscillations. Furthermore, the nominal values of $\hat{k}$ at the lowest oscillation amplitude, 0.2 MPa, are consistent with the nominal static permeabilities, see Figure 3.4b. Also, the slope of dynamic permeability with respect to oscillation amplitude, indicated with dashed blue lines in Figure 3.8a decreases with applied stress and remains nearly invariant during the unloading phase. This slope, $\hat{\varphi}$ is summarized in Figure 3.8b and is consistent with our measurements of static permeability throughout the experiment, 3.4b.

### 3.6.5 Dynamic Stress-induced Changes in P-wave Velocity

One of the measures of elastic nonlinearity, the relative change in velocity ($R_0$) for all transmitter-receiver pairs as a function of pore pressure oscillation amplitudes are shown in Figure 3.9a. As noted previously [67, 105, 126], the magnitude of $R_0$ clearly increases with increasing pressure oscillation amplitude. Furthermore, after an initial increase, increasing effective stress generally reduces the magnitude of $R_0$, as seen in Figure 3.9b in agreement with previous observations [67, 94]. The data in Figure 3.9 are colored by location of the PZTs along the fracture plane (see scaled version in figure legend) to reveal the spatial variability of the measured nonlinearity. One observations across all stress levels is that the nonlinearity (larger magnitude $R_0$) measures the highest for the transducer pair at the bottom left corner (light pink color). In contrast, the nonlinearity measured by the transducer pair at the top right corner (dark green color) is among the lowest at all stress levels.

Another measure of elastodynamic nonlinearity that we investigate is the relative change in the average amplitude of the wave velocity change, $R_1$. Figure 3.10a shows $R_1$ as a function of pore pressure oscillation amplitude for all transmitter-receiver pairs. Like $R_0$, the average amplitude wave velocity $R_1$ scales linearly with increasing pore pressure oscillation amplitude, as expected [92, 93]. As the fracture is closing with the increased applied stress, the slope of $R_1$ with respect to the oscillation amplitude denoted as $\beta$ increases at 12.5 MPa, decreases, and then slightly increases again at 17.5 MPa, see Figure 3.10b. The trend is slightly different for different transducer pairs. Overall, the magnitude of the nonlinear elastic parameters are consistent with previous studies on fracture rock specimens, for the respective stress levels [68, 105, 126].

### 3.6.6 Measurements During Loading vs. Unloading Phase

A key part of this study is understanding the effect of fracture aperture, degree to which the fracture is closed or open under different applied stresses, on the stiffness and hydraulic properties of the fracture interface. Besides measurements at increasing effective stress levels (loading), we performed a subset of the pore pressure oscillation protocol while unloading the sample. During the unloading phase, the confining stress was decreased incrementally to the stresses previously used during the loading phase (17.5, 15, 12.5, 10) MPa. Figure 3.11 shows summarized results of the $\Delta k/k_0$ slope, $\varphi$, as a function of applied stress for both the loading (circle markers) and unloading (square markers) phases of experiment p5483. There is some hysteresis comparing the loading phase to the unloading phases with nearly an order of magnitude difference between $\varphi$ at the beginning and end of the loading cycle. During the loading phase, there is a large increase in $\varphi$ from 15 to 17.5 MPa, which we attribute to the long hold after 15 MPa. We posit that the $\Delta k/k_0$ measurement is sensitive to on-fault properties such as surface mating, creep, or fine wear products (breakage of asperities). However, during the unloading phase, $\varphi$ generally increases with decreasing applied stress, but does not return to the initial value at 10 MPa. This hydraulic measurement could be, to some extent, influenced by deformation that occurs at 20 MPa, marginally changing preferential fluid pathways.

This hysteresis is also observed in the measures of nonlinearity, $R_0$ and $R_1$ albeit less pronounced. Figure 3.12 shows $\alpha$ measured for each transmitter-receiver pair as a function of applied stress for the loading and unloading phases of experiment p5483. During the loading phase, there is a characteristic decrease at $\sigma_{\text{eff}} = 12.5$ MPa (higher nonlinearity) and then an increase at $\sigma_{\text{eff}} = 20$ MPa (lower nonlinearity) for most of the transducer pairs. However, during the unloading phase, the change in $\alpha$ is either nearly invariant with applied stress (light blue, dark red) or linearly increases in magni-

tude. A common observation across all transducer pairs is the slightly higher measured nonlinearity during unloading than that during the loading phase at a given stress. Possibly, the asperities break and deform when loading leading to a larger instantaneous stress-induced stiffness change $R_0$ during unloading and therefore, larger $\alpha$ magnitudes.

Similarly, Figure 3.13 shows $\beta$ as a function of applied stress for each transmitter-receiver pair during the loading and unloading phases of the experiment. The measured $\beta$ and hysteresis vary significantly for different transducers. The pairs in the two upper rows with $\beta$ close to zero show nearly stress-invariant wave velocity amplitude modulation, whereas others in the bottom row show greater nonlinearity and hysteresis loops. As previously noted, the measured $\beta$ during the loading phase is mostly insensitive to the effective stress level except for a local increase at 12.5 and a slight increase at 17.5 MPa for some transducer pairs. During the unloading phase, $\beta$ generally increases returning to the initial value measured at 10 MPa. The observed hysteresis loops appear larger for transducer pairs with a larger measured $\beta$. Unlike what is observed for $\alpha$, $\beta$ measures consistently lower during unloading than loading. Previous studies relate $\beta$ to opening and closing of fractures [93]. We hypothesize that the broken and deformed fracture asperities during loading facilitate the mating of the two fracture surfaces, making it harder for the fracture to close, thus smaller $\beta$. We note that for both $\alpha$ and $\beta$, the nonlinearity measured during unloading increases with decreasing stress, which is expected due to fracture opening. Though, we did not quantify the damage and did not observe noticeable damage while conducting the experiment or pressure sensitive film testing. Upon visual inspection gouge material (from broken asperity tips) was not present in the down-stream reservoir, indicating that the concentration is low and particle size is $<$µm.

### 3.6.7 Permeability Recovery and Slow Dynamics

The post-oscillation evolution of permeability and p-wave velocity is related to how the fracture contact asperities have been transiently or irreversibly changed during the imposed oscillations. Also, the time-dependent phenomenon provides an indication of the rate of healing [27] and recovery at the perturbed interface. Here, this is measured as the slope of the recovery in logarithmic time. Our observations indicate that log-time permeability recovery $k_r$ is mostly invariant to the amplitude of pore pressure oscillations at higher normal stresses ( $>$ 12.5 MPa), Figure 3.14a. At lower normal stresses, the log-time evolution recovers more quickly at lower pore pressure oscillation amplitudes. These overall trends are summarized in Figure 3.14b with the slope of $k_r$ as a function of applied stress, which also includes results from the unloading phase of the experiment.

The p-wave velocity recovery $c_r$ for all transmitter-receiver pairs as a function of pore pressure oscillation amplitude is shown in Figure 3.15a. The measured recovery rate slightly increases with increasing pressure oscillation amplitude i.e., the wave velocity returns to the pre-oscillation value quicker after larger amplitude oscillations. The slopes change slightly and unsystematically with fracture closure, Figure 3.15b, but during the unloading phase, there is much less spread between the transmitter-receiver pairs and more systematic evolution with applied stress (fracture opening). In Figures 3.14b and 3.15b and 3.15c, both $k_r$ and $c_r$ slopes show a hysteretic relationship with fracture closing and opening (increasing and decreasing applied stress).

## 3.7 Discussion

### 3.7.1 Elastic Deformation of Fracture and Bulk

We observe that the hydraulic and elastodynamic measurements scale with applied stress. On-fault compaction (Figure 3.4a) shows minimal hysteresis in loading and unloading the fractured rock specimen. This, along with the stress-displacement curves in Figure B.2, demonstrates that our observations are repeatable and the fracture is well-mated. A common observation in experimental studies is that fracture specimens must be "pre-conditioned" with an initial load/unload cycle with the purpose of optimally mating the two fracture faces [4, 98]. Importantly, these studies find that subsequent loading cycles produce reversible (as a function of stress) elastic or hydraulic properties. Our results depart from these observations as seen in Figure 3.4a and S3, which show that despite reducing the stress after the 15 MPa stress level and holding at 2 MPa for several hours before increasing the stress to 17 MPa, that the overall elastic deformation is not dominated by severe misalignment. An additional observation is a minor degree of compaction unloading the sample from 20 MPa to 17.5 MPa. We surmise that the sudden increase in pore pressure after the last pore pressure oscillation sequence (before the normal stress reduction) may have an influence on compaction of the fracture sample. This effect is minor in that it is a couple microns and it does not have a noticeable effect on permeability or the dynamic measurements (Figures 12 - 15). Furthermore, the hydraulic measurements of this study (static and dynamic permeabilities) do no exhibit a significant (order of magnitude) difference in loading and unloading phases of the experiment, like in [98]. We interpret the reduction in permeability (static and dynamic) during the loading phase as being dominated by fine-scale asperity deformation, likely plastic [10].

As previously stated in Section 3.6.3, the nonlinearity in the elastic response of

rocks arises from the compliant features in their matrix structure (microcracks and grain boundaries) [41, 93]. Fracture interfaces introduce additional nonlinearity (CAN). However, as shown in our previous work, the influence of a fracture on the overall elastodynamic behavior of fractured rock depends on the applied stress as well as the number and size of asperities in contact. In [68], a similar set of experiments were conducted, in which the nonlinear response of intact Westerly granite was compared to that of fractured (fluid-filled and dry) specimens at 10, 15, and 20 MPa normal stresses. At all stresses and excitation frequencies (0.1, 1, and 10 Hz) considered, the nonlinearity in the elastodynamic response (measured in terms of relative wave speed change) of the dry intact specimen was larger than that measured in the tensile-fractured specimen. To explain this counter-intuitive observation, a 2D finite element analysis on simplified models of intact and fractured rock with different roughness under static stress was conducted. The numerical modeling and simulation results illustrated that the fracture significantly modifies the strain distribution in the bulk of the stressed rock in our test configuration as later reported by [100] as well. It appeared that intact samples could experience larger strain in their bulk compared to fractured samples, where strain is largely concentrated on the asperities in contact at the fracture interface. As a result, a larger change in wave speed may be measured in bulk, where a larger area is strained above $10^{-6}$, the widely accepted threshold for activating elastic nonlinearity. Interestingly, the relative change in wave amplitude measured larger for dry fractured sample under 10 MPa and 15 MPa at low frequencies, contrary to what was consistently observed for the wave speed change. Although not discussed in [68], this apparent contradiction is in agreement with [78] and [109]'s conclusions that wave amplitude is more affected by on-fault properties while wave speed reflects the strain distribution in the bulk. At 20 MPa, both relative wave speed and wave amplitude are smaller for fractured sample indicating that the strain in the bulk under this larger stress dominates

the straining of the in-contact asperities, possibly because of their larger contact areas. In sum, there is no simple way to disentangle nonlinearity of the bulk from the fracture interface in our experimental observations. The partitioning is controlled by the strain distribution in the bulk vs. the strain concentrated at the fracture interface (asperities) which depend on the amount of stress applied, the overall contact area and the size of individual asperities in contact.

### 3.7.2 Linking Stress-Induced Elastodynamic and Hydraulic Changes

To investigate the coupling between fluid flow changes and elastodynamic nonlinearity, we analyze how the observed stress-induced changes in p-wave velocity is connected to changes in permeability at different normal stress levels. Figure 3.16a relates stress-induced changes in p-wave velocity to changes in permeability ($\Delta k/k_0$) for each effective applied stress. In this figure, $\overline{R_0}$ denotes $R_0$ averaged over all transmitter-receiver pairs. Both of these parameters measure average changes along the fracture in response to stress perturbations. We observe a linear correlation between $\overline{R_0}$ and $\Delta k/k_0$, which appears to be mostly independent of the stress level. In addition to the transient changes, we relate the stress-induced changes in p-wave velocity and dynamic permeability during the oscillations. Figure 3.16b shows the nonlinear elastic parameter $R_1$ averaged over all transmitter-receiver pairs as a function of $\hat{k}$. Again, we observe a monotonic relationship between the magnitude of nonlinearity, $\overline{R_1}$, and dynamic permeability, $\hat{k}$. Furthermore, in both plots in Figure 3.16 show that increasing applied stress reduces both the elastodynamic response ($\overline{R_0}$ and $\overline{R_1}$) and permeability enhancement ($\Delta k/k_0$ and $\hat{k}$), consistent with the idea that these are measures of the degree to which the fracture aperture is modulated.

### 3.7.3 Relating Contact Area to Elastodynamic Properties

True fracture contact area constrain many of the elastodynamic and hydraulic observations. Figure 3.2c,e show that the estimated true contact area using pressure sensitive film increases as a function of applied stress in a Hertzian-contact-like manner (cubic relationship), effectively reducing aperture and enlarging individual contact areas. Defining Fresnel ray-path tunnels between transmitters and receivers (PZT footprints) projected on the pressure sensitive film images allows us to investigate the true contact area and its evolution for individual transducer pairs. The estimation of fracture contact area is limited by two main factors: (1) spatial/stress resolution of the pressure sensitive film and (2) physical characteristics of the pressure sensitive film (i.e. film thickness and stiffness), which determine how the plastic film deforms between the fracture halves and registers local stresses. We observe that nearly all asperities register the maximum stress $> 49$ MPa, therefore limiting analysis to a binary contact/void image. The ideal application of such pressure sensitive films is between two nominally planar surfaces, however, despite some deformation or crinkling of the films, we emphasize its utility in reliably estimating contact area, Figures 3.2e and 3.5. Though there are caveats to this method of measuring real contact area, Figure B.2 demonstrates the high degree of repeatability. The loading/unloading curves all show minor hysteresis, but are nearly identical even at low stresses, which suggests that the contact area measurements using pressure sensitive film are relevant to the main experiment where we measured hydraulic and elastodynamic changes in response to stress oscillations. Figure 3.5 confirms significant heterogeneity in the area of contact for various transmitter-receiver pairs at the same applied stress. We posit that this heterogeneous distribution in asperity contact resulting in spatial variation of specific stiffness across the fracture is a key factor behind the observed differences among nonlinear elastodynamic measurements from different transducer pairs. Though post-experiment contact area measurements have the poten-

tial to introduce some bias, we believe that the mechanics during the loading phase of the experiment are more comparable to the successive load/unload cycles involved in the pressure sensitive film measurements. Due to the nature of the pressure sensitive films, we are not able to register the real area of contact while unloading. Compared to roughened planar surfaces, it is more challenging to measure the real area of contact for tensile fractures with long wavelength roughness.

Next, we investigate the relationship between the nonlinear parameters and estimated contact area. Since stiffness is defined as $\kappa = \frac{F}{S\delta}$, where $\delta$ is displacement, assuming a nominal unit area and considering the dependence of the contact force $F$ on the number and radii of asperities in contact [51], we may take contact area $S_0$ to be a proxy for the interface stiffness at rest $\kappa_0$. It is important to make the distinction that this is not the only source of nonlinearity [41, 55]. Previous studies [51, 68] show that intact specimens exhibit a greater degree of nonlinear elastic response to dynamic stress compared to fractured specimens. Nonetheless, a fracture with a larger true contact area is expected to be stiffer and therefore is more difficult to induce changes. Since the nonlinearity parameter $R_1$ is believed to be related to the opening/closing of the fracture, it is considered to be a measure of $\Delta\kappa/\kappa_0$. Therefore, an important question to ask is whether our data show a correlation between $R_1$ and $S_0$. That is to say, what is the correlation between elastodynamic changes and initial contact area. To our knowledge, this is the first experimental investigation of the relation between contact area and elastic nonlinearity of a fracture. The expectation is that regions of the fracture with a larger true contact area, $S_0$, should be stiffer and therefore, more difficult to open and close (at a given dynamic stress level). This reasoning is supported by our observations shown in Figure 3.17, which shows $S_0$ as a function of $\beta$ during the loading phase of the experiment. This illustrates that regions with a smaller contact area (pale orange) for a given stress level exhibit larger nonlinearity compared to those with larger contact area

(dark green). Results for contact area as a function of $\beta_{unload}$ are plotted in Figure B.4. Despite the caveats to this technique (see Section 3.6.2 for details), we emphasize the utility in estimating the distribution of contacting asperities to interpret, with greater certainty, the causes of spatial variability in ultrasonic measures of fracture properties. Furthermore, Figure 3.17 suggests that over the range of normal stresses explored in our experiments, fracture topology (contact area and roughness) is the primary control on fracture stiffness and also fluid flow [84].

### 3.7.4 Broader Impacts and Insights

Dynamic stressing of pore pressure at a range of amplitudes in our experiment allows simulates dynamic stressing in field conditions and the observed hydraulic and elastic responses. Furthermore, repeating this pore pressure oscillation protocol at different applied stresses simulate conditions at different (shallow) depths in the crust. Figure 3.6 demonstrates many qualitative similarities between experiment and field observations. The transient decrease in cross-fault wave velocity is reminiscent of field observations of co-seismic elastic softening [12–14, 25, 33, 46, 48, 62, 63, 77, 122, 127]. Figure 3.6 also shows through-fault permeability enhancement, much like what is observed in the subsurface [15, 66]. Importantly, the fractured specimen in our experiment did not contain real or simulated gouge material, further demonstrating that many of the complex field conditions can be approximated with a "bare" fracture under similar stress conditions and evolution of fracture geometry (roughness, contact area) may be a prevailing factor.

Another quality produced in our experimental configuration is the log-time recovery of velocity and permeability (slow dynamics) toward their respective pre-oscillation values. The magnitude of velocity recovery is comparable to previous observations of rough fractures [68, 126], similar to post-seismic recovery of rock stiffness [14, 78]. However, permeability recovers much quicker than previous observations where gouge/wear mate-

rial is present at rough fracture interface [30, 126]. A pressure-solution mechanism [1] is assumed to not play a role in contact area changes in our experiment due to insufficient conditions – low temperature and stress and non-reactive pore fluid (deionized water). This highlights the degree to which chemo-mechanical [130, 131] and gouge transport (clogging/unclogging) [20, 21, 30] dominate field observations of permeability enhancement induced by seismicity [15, 66].

## 3.8 Conclusion

We present tightly-constrained experiments to investigate the role of aperture and real contact area on hydraulic and elastodynamic properties of dynamically-stressed fractured rock. Conditions are representative of fractures at various depths and therefore stresses. Simultaneous measurements of fluid flow and active-source ultrasonic transmission show how these mechanisms are coupled – potentially linking permeabilities with elastodynamic characteristics. Additionally, we quantify the heterogeneity of the fracture contacts at discrete stresses in order to better interpret our observations from multiple transducer pairs probing different parts of the fracture.

Fractured Westerly granite exhibits characteristic mesoscopic elastic nonlinearity when subjected to pore pressure oscillations, revealing rich information about the contact mechanics of the asperities. Our observations, as found in [105,126], show a nearly monotonic relationship between increased permeability enhancement and increased pressure oscillation amplitude. We add to the work of [67, 105, 126] by documenting a reduction in pore pressure oscillation-induced permeability enhancement with increasing normal stress on the fracture and related fracture closure. Similar trends are observed for the nonlinearity parameters $\alpha$ and $\beta$. For some transmitter-receiver pairs, the nonlinearity parameters depend on the degree of fracture openness (in the corresponding region of the fracture) immediately before oscillation. There is a noticeable increase in nonlinearity,

$\alpha$ and $\beta$, from 10 MPa to 12.5 MPa, for example (see Figures 3.9b and 3.10b). That is to say, the dominating factor is not necessarily the stress state, but the local fracture aperture.

We investigate the spatial heterogeneity of nonlinearity parameters with regard to actual estimations of fracture contacts and voids. To that end, pressure sensitive film images are related to ultrasonic measurements; a smaller initial contact area ($S_0$) is associated with higher nonlinearity $\beta$ and a larger $S_0$ with a smaller $\beta$. Importantly, the estimate of fracture contact area over the range of normal stresses explored in our experiments demonstrates that fracture topology is a primary control on the observed elastodynamic and hydraulic responses.

Finally, we document the rate of recovery from post-oscillation state of permeability and wave velocity. The rate of permeability recovery (log-time) increases above $\sim 0.4 - 0.6$ MPa amplitude oscillations at lower stresses ($\sigma_{\text{eff}} < 17.5$ MPa) and is oscillation amplitude-invariant at higher stresses ($\sigma_{\text{eff}} > 15$ MPa), (see Figure 3.14). These recovery rates are orders of magnitude smaller than those reported in previous studies [105, 126], where gouge present at the fracture interface dominated permeability changes. During the unloading phase, the rate of recovery increases with decreasing stress state. These recovery rates are also smaller than in previous studies [105, 126], suggesting "accumulated deformation" throughout the loading phase of the experiment.

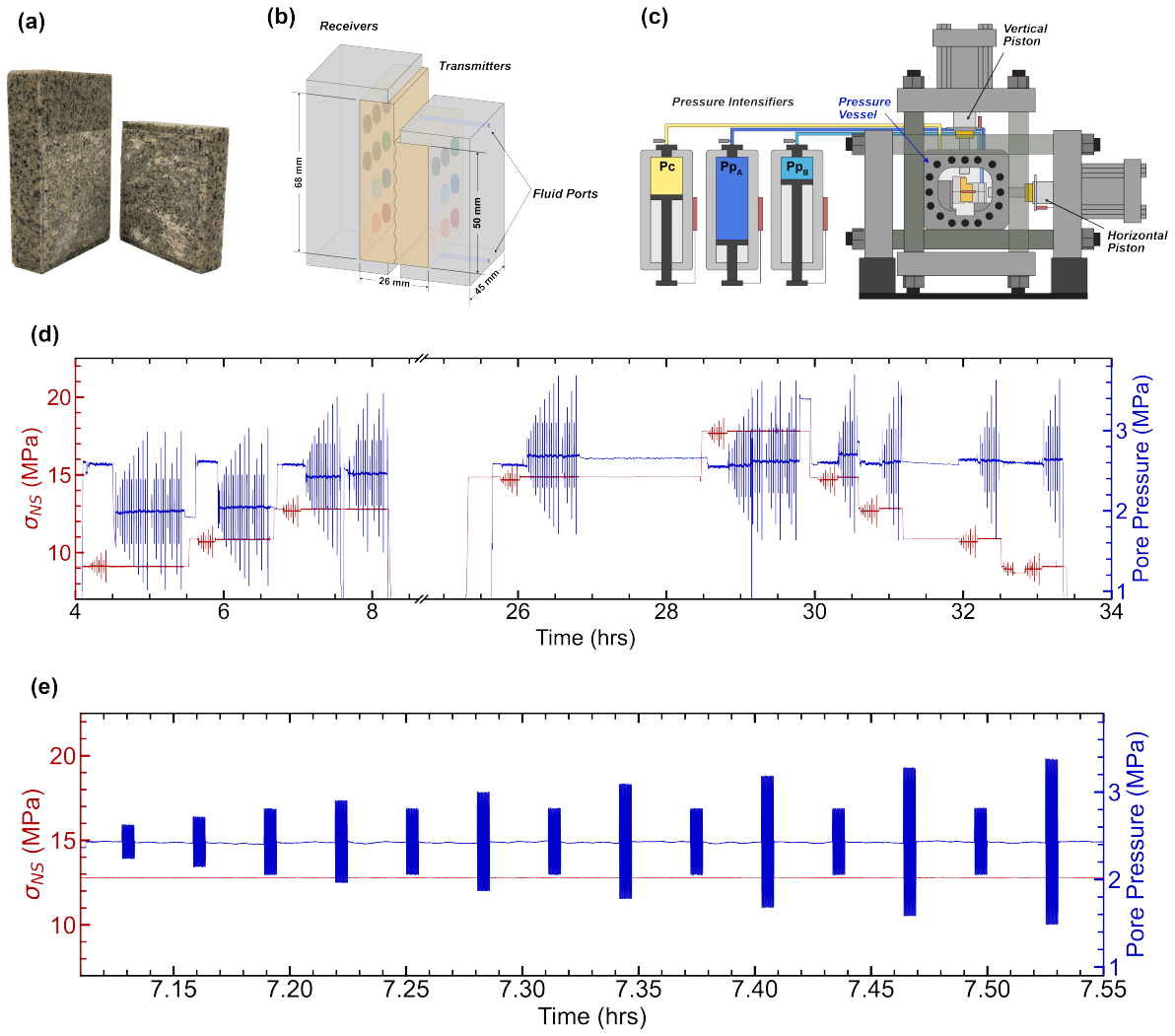



**Figure 3.1.** (a) Pre-fractured L-shaped Westerly granite sample. (b) Transmitter-receiver pairs used in active source ultrasonic monitoring embedded inside loading blocks (inactive sensors are dark-grey). (c) Biaxial loading apparatus with pressure vessel in Penn State's Rock Mechanics Laboratory. After sample preparation and installation in the pressure vessel, the fracture was saturated with deionized water. Imposed dynamic oscillations of pore pressure with amplitudes ranging from 0.2 to 1 MPa at 1 Hz. (d) Overview of the experiment showing the applied normal stress levels (10, 12.5, 15, 17.5, 20 MPa) in red and pore pressure oscillations in blue. Normal stress oscillations at the beginning of each stress level were performed for a separate study. (e) Pore pressure oscillations at 15 MPa $\sigma_{\text{eff}}$.

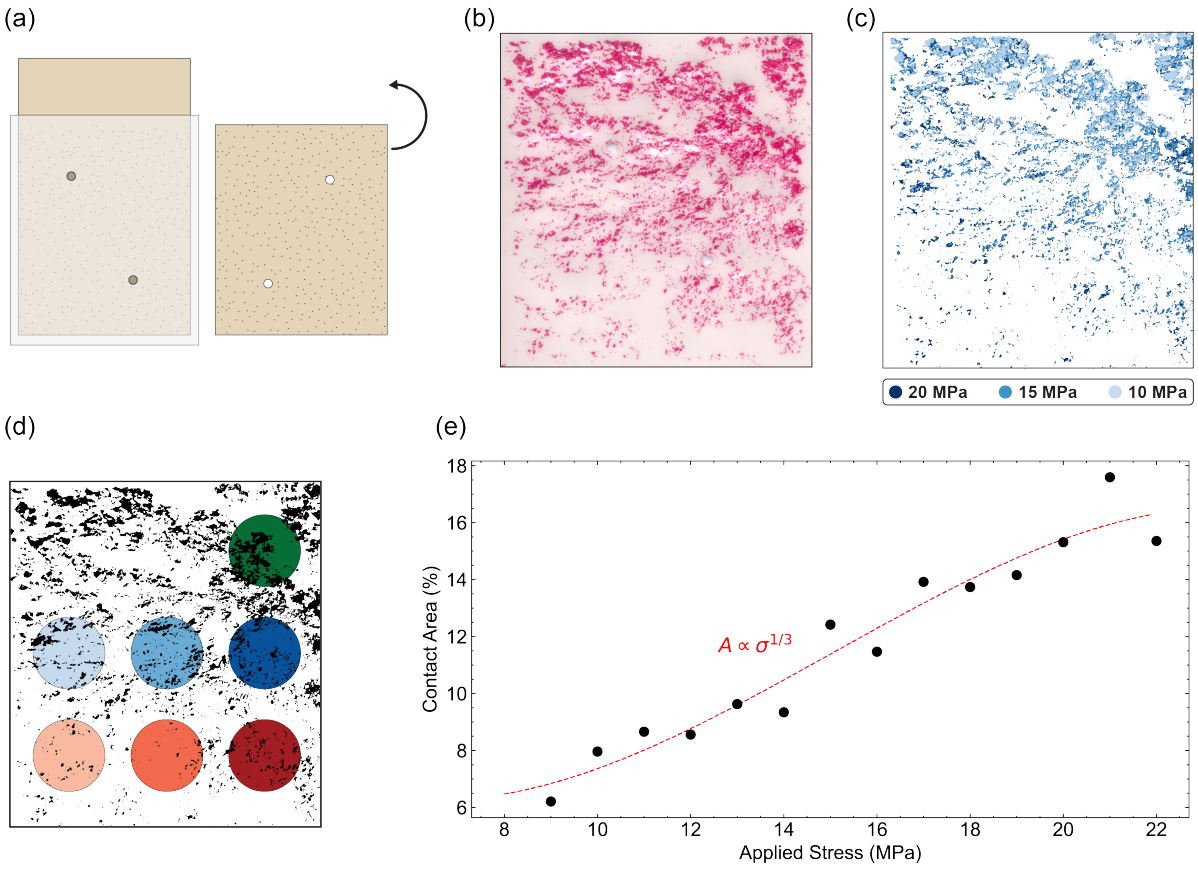



**Figure 3.2.** (a) Sketch of fracture and locating pins to insert pressure sensitive film. (b) Example of pressure sensitive film after loading to 20 MPa. Magenta regions represent contact and remaining areas are voids. (c) Superimposed images showing the evolution of contact area with applied stress at 10, 15, and 20 MPa. (d) Colored circles represent fracture regions probed by the array of transmitter-receiver pairs, where the footprint size is calculated from the Fresnel zone. (e) Real contact area from film measurements (as in b) relative to nominal total area as a function of applied stress. The dashed line shows a cubic fit to these data, suggesting a Hertzian-contact relation between area and stress.

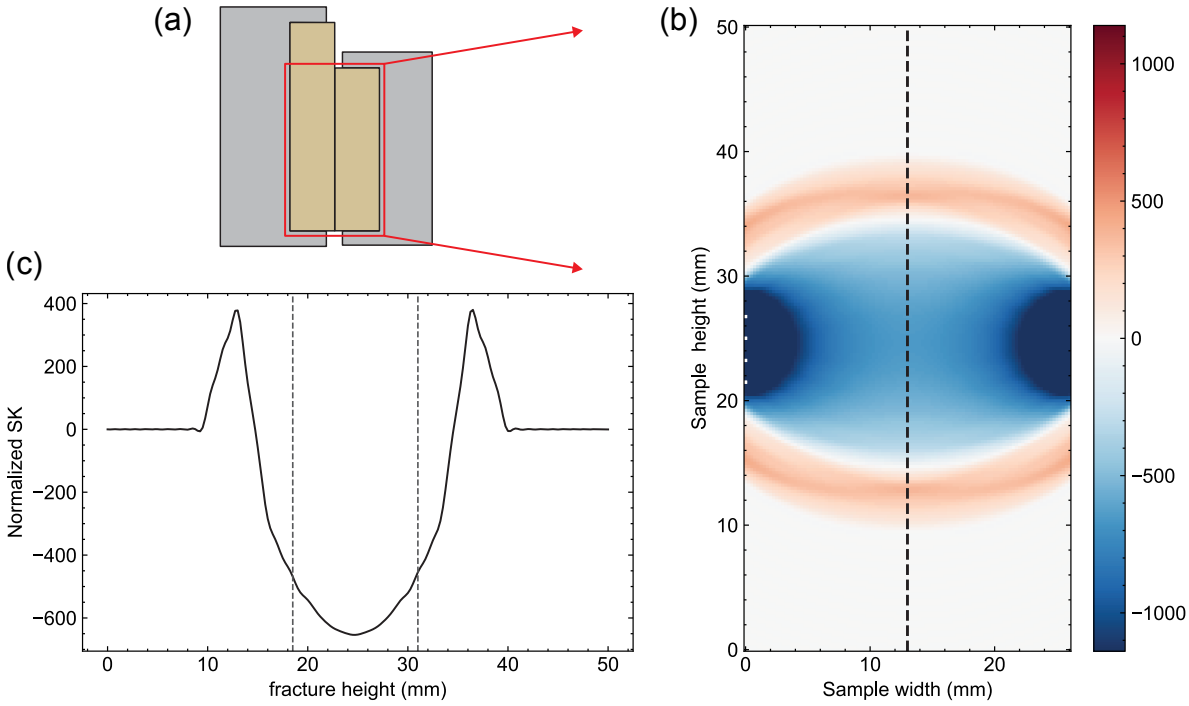



**Figure 3.3.** (a) Diagram of L-shaped configuration with region of interest outlined in red. (b) Amplitude sensitivity kernel model across granite block, where intensity represents response of transmitted wave to perturbation. (c) Profile of sensitivity kernel along the fracture plane (denoted by dashed black line in (b)). Dashed gray vertical lines indicate the half-power bandwidth of the Fresnel zone, where the transmitted waves are most sensitive to perturbations along the travel path (left to right).

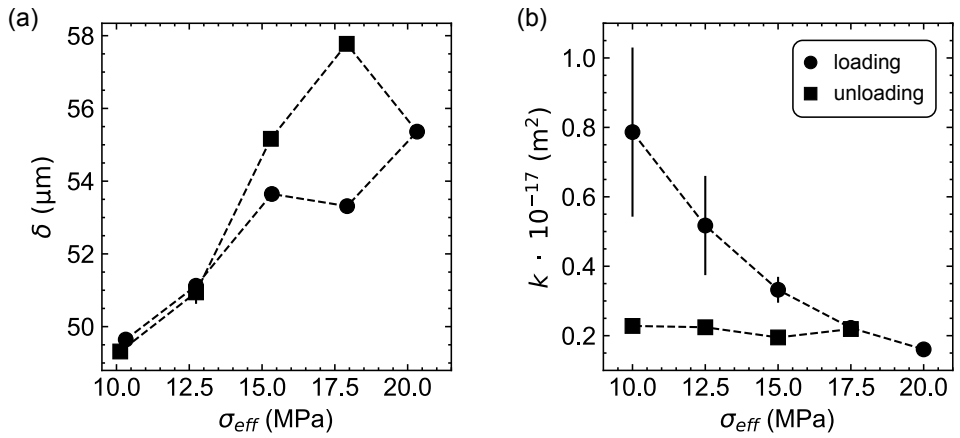



**Figure 3.4.** (a) Compaction, $\delta$, at each effective stress level during the loading and unloading phase. (b) Static permeability, $k$, as a function of effective stress.

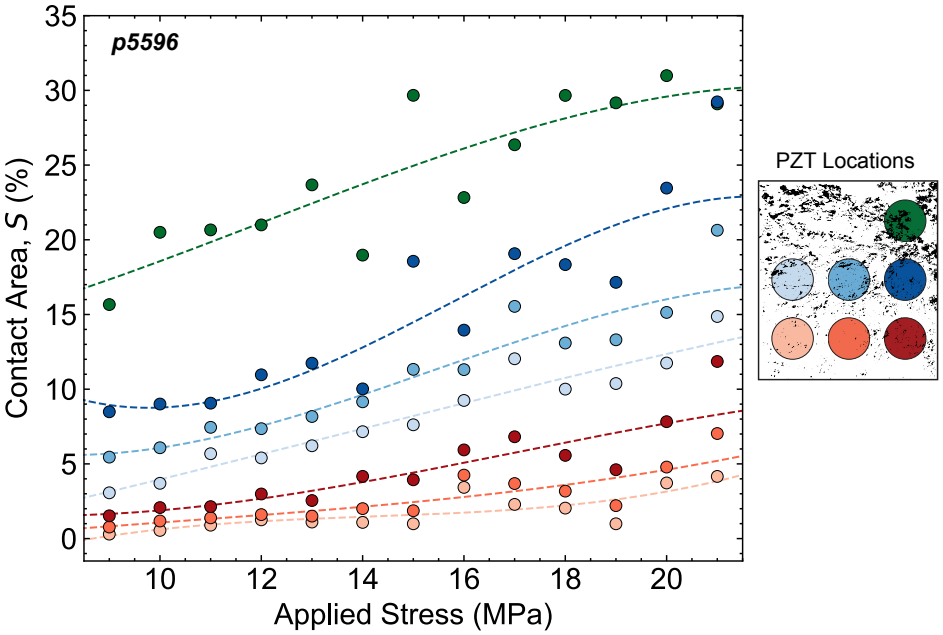



**Figure 3.5.** Percent area of fracture in contact within each PZT "footprint area" as a function of applied stress for one experiment. Contact area is directly estimated by pressure sensitive films at each stress. Note spatial variations in contact, as expected for a rough fracture, and also non-linear changes with stress. Each measurement involves re-mating the fracture and thus some variability is expected.

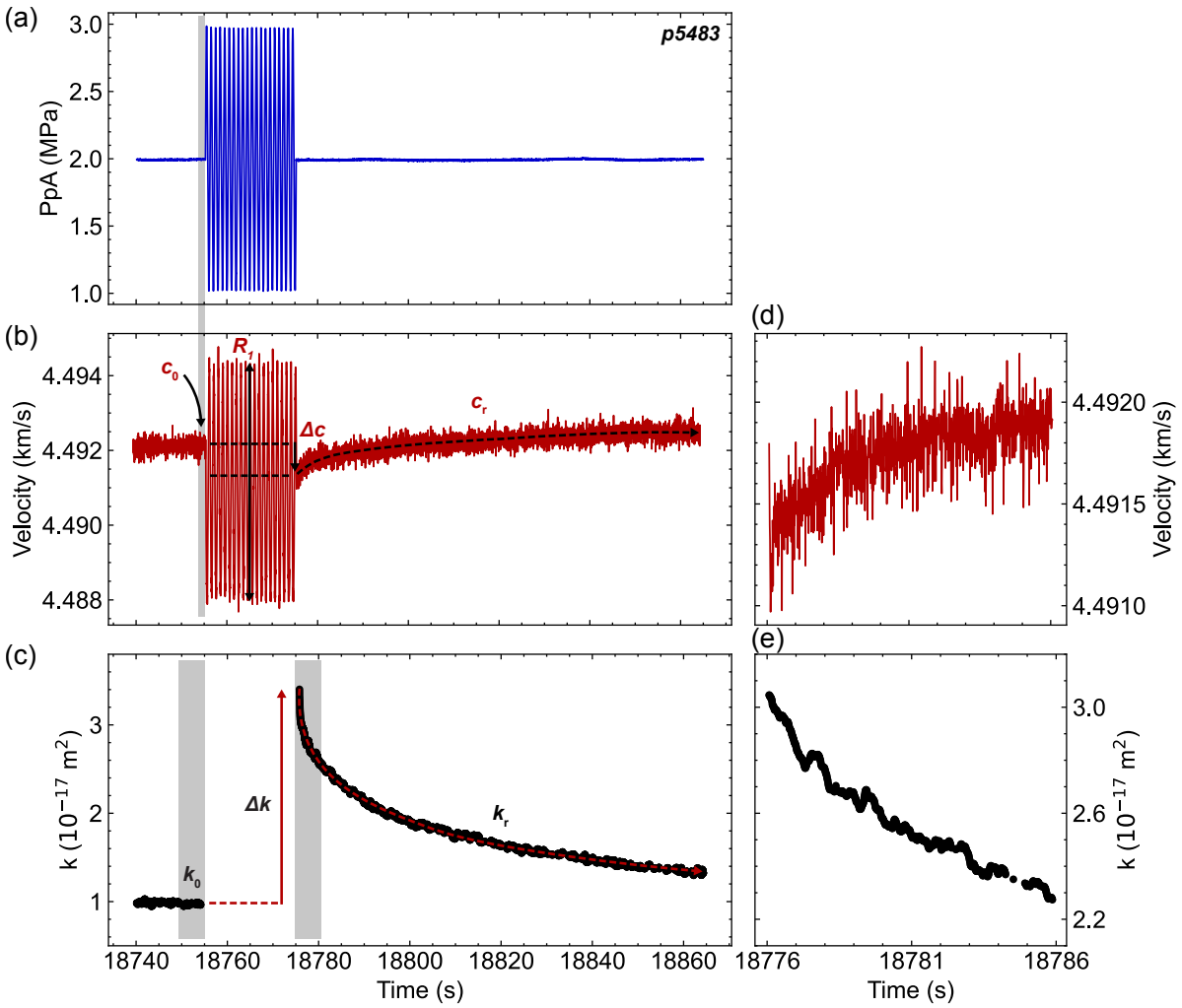



**Figure 3.6.** Excerpt of data from experiment p5483 illustrating the effect of (a) pore pressure oscillation (1 MPa amplitude at 1 Hz) on (b) ultrasonic p-wave velocity and (c) permeability at applied normal stress of 20 MPa. A 1 second window preceding the oscillation is used to calculate the pre-oscillation values of velocity ($c_0$), highlighted in grey. Changes in permeability are calculated from pre-oscillation, $k_0$, and post-oscillation magnitudes, $k_1$, averaged in 5 s windows, respectively. Long-term post-oscillation evolution in wave velocity and permeability ($c_r$, $k_r$ respectively) are illustrated with arrows. The first 10 s of post-oscillation recovery for p-wave velocity and permeability are shown in (d) and (e), respectively.

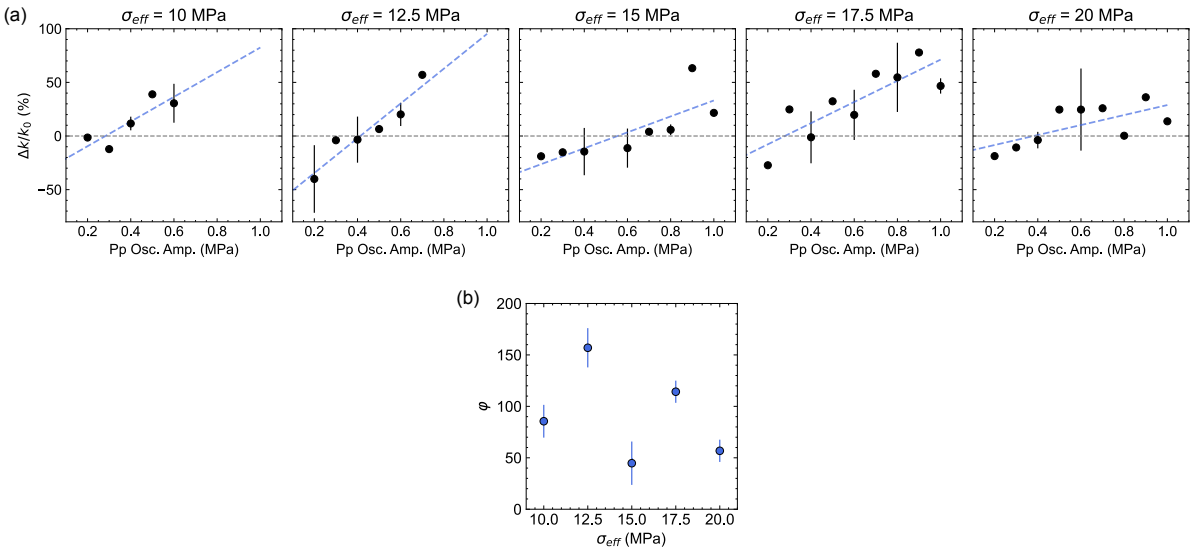



**Figure 3.7.** (a) Relative permeability change ($\Delta k/k_0$) as a function of pressure oscillation amplitude for each applied normal stress. For all applied normal stresses, permeability changes increase with increasing pressure oscillation amplitude. Error bars are one standard deviation from mean for oscillations with repetitions. (b) The ratio of change in relative permeability with pore pressure amplitude, $\varphi$, generally decreases with applied stress, except from 15 to 17.5 MPa.

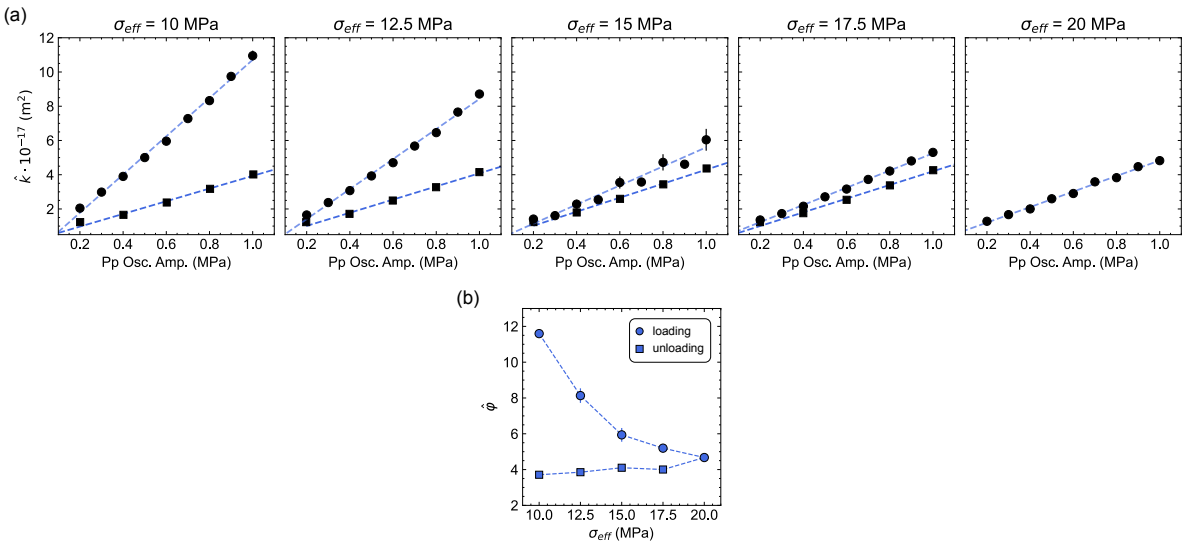



**Figure 3.8.** (a) Dynamic permeability, $\hat{k}$, as a function of pore pressure oscillation amplitude for each effective stress level, circles indicate loading phase and squares indicate unloading phase. (b) Slope of dynamic permeability, $\hat{\varphi}$, for the loading and unloading phases.

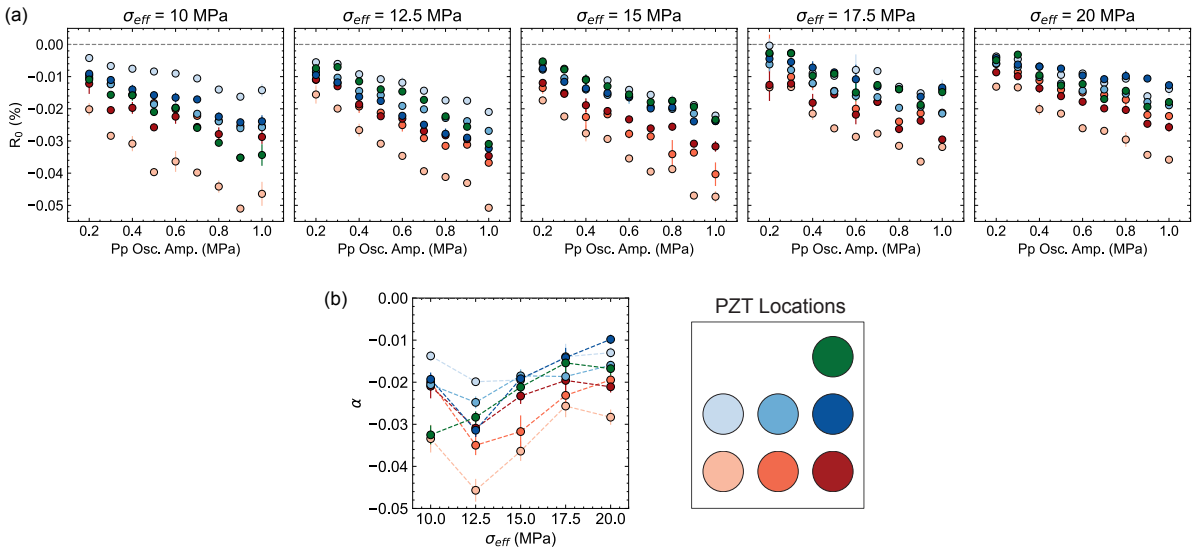



**Figure 3.9.** (a) Relative velocity change ($R_0$) averaged over repetitions at each oscillation amplitude as a function of amplitude. Symbol colors correspond to the highlighted transducer footprint locations (see legend). (b) Slope of $R_0$, $\alpha$, versus oscillation amplitude for each normal stress, a measure of hysteretic nonlinearity. $\alpha$ decreases, then increases for most transmitter-receiver pairs. This represents a presumed fracture closure and increase in specific stiffness.

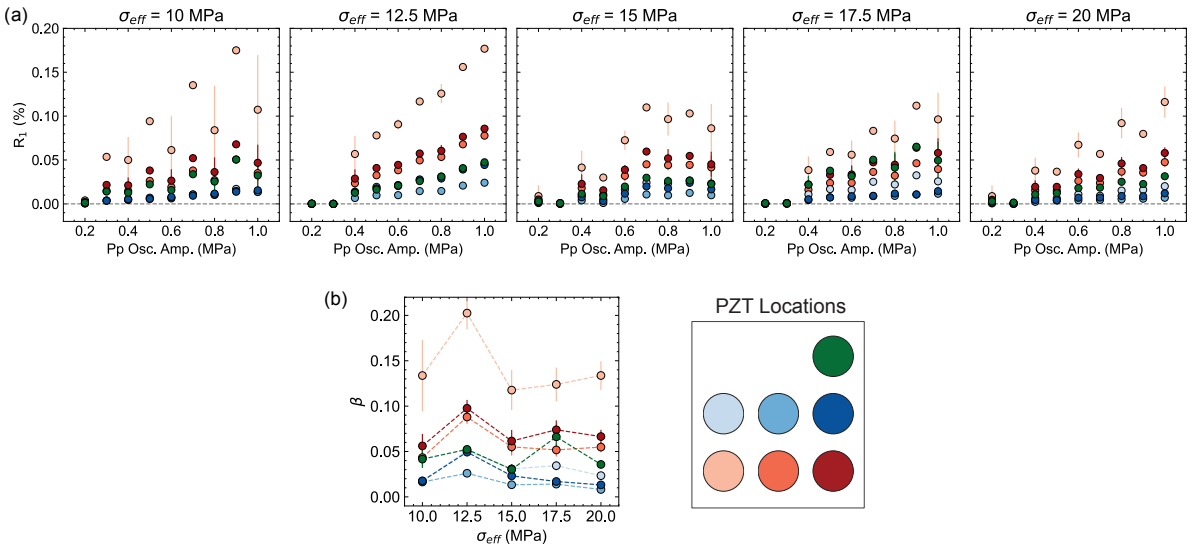



**Figure 3.10.** Relative change in the average amplitude of the wave velocity change ($R_1$) as a function of pressure oscillation amplitude. Symbol colors correspond to various ray path locations across the fracture. (b) Slope of $R_1$, $\beta$, versus pressure oscillation amplitude for increasing applied normal stress.

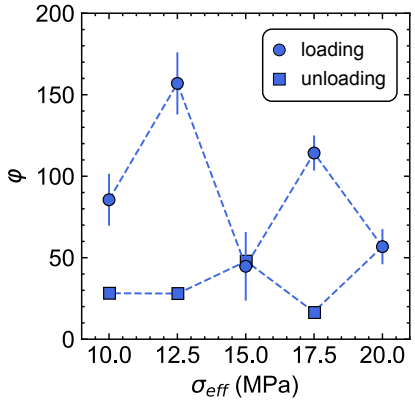



**Figure 3.11.** Slope of $\Delta k/k_0$, $\varphi$, as a function of applied stress for loading and unloading phases of the experiment.

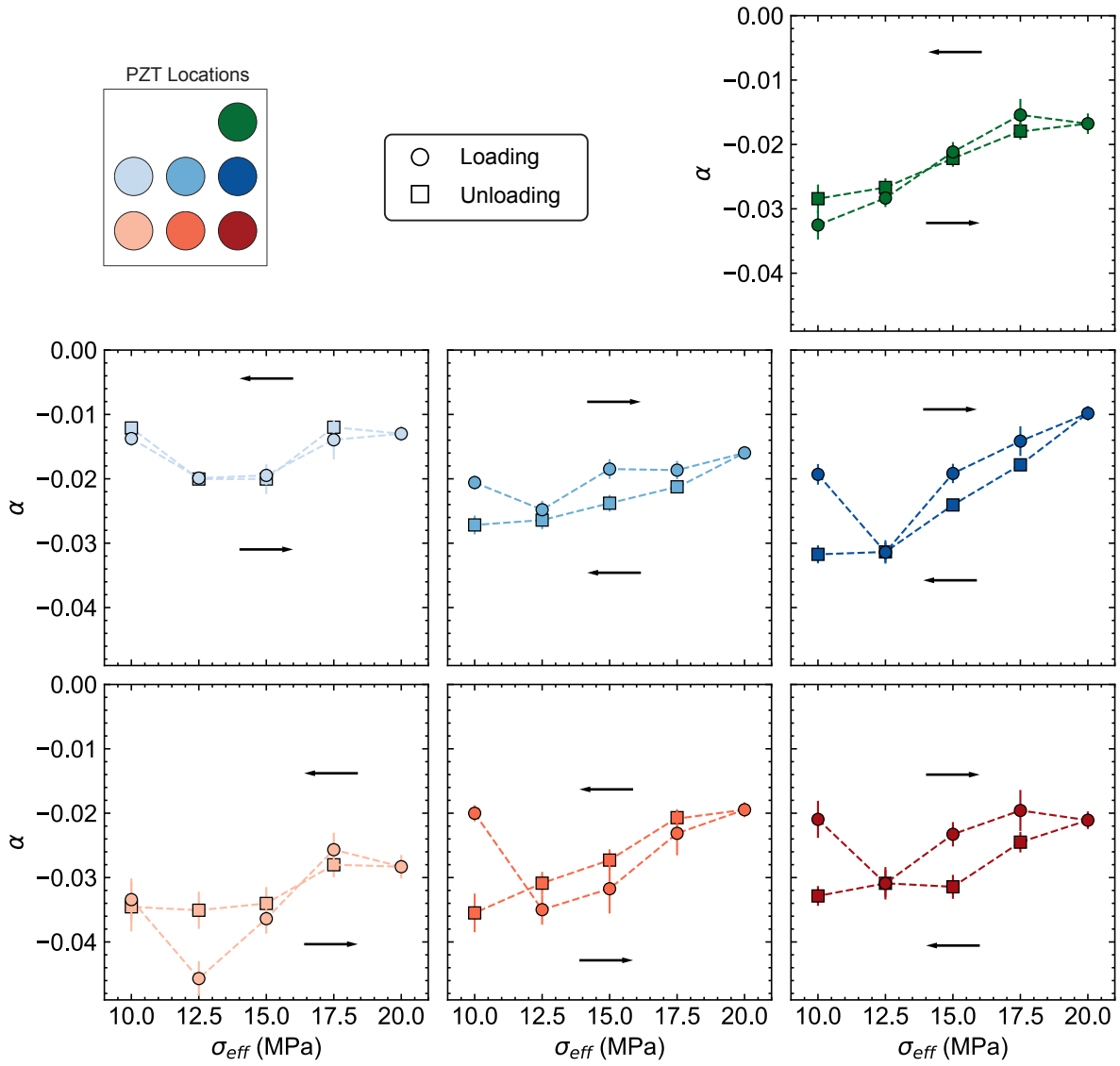



**Figure 3.12.** $\alpha$ vs. applied stress for loading and unloading phases of the experiment. A lower value of $\alpha$ corresponds to a larger nonlinearity. We see an overall decrease in nonlinearity with applied stress ($\alpha$ tends toward zero) for some of the pairs (e.g., dark green), while no clear trend can be seen for other pairs (i.e., light blue).

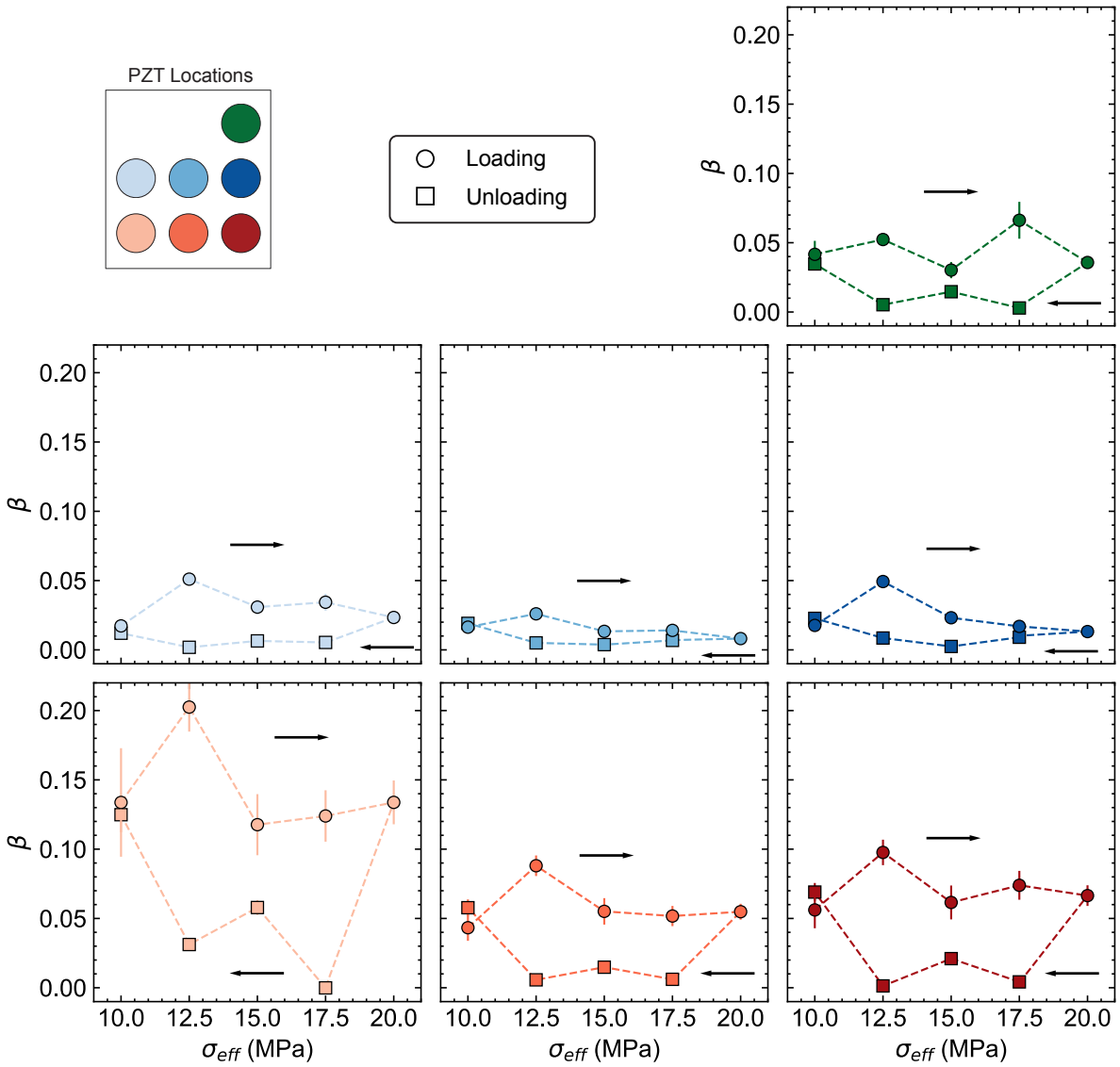



**Figure 3.13.** Nonlinearity parameter $\beta$ vs. applied stress for loading and unloading phases of the experiment, shows the hysteresis in changes in fracture stiffness.

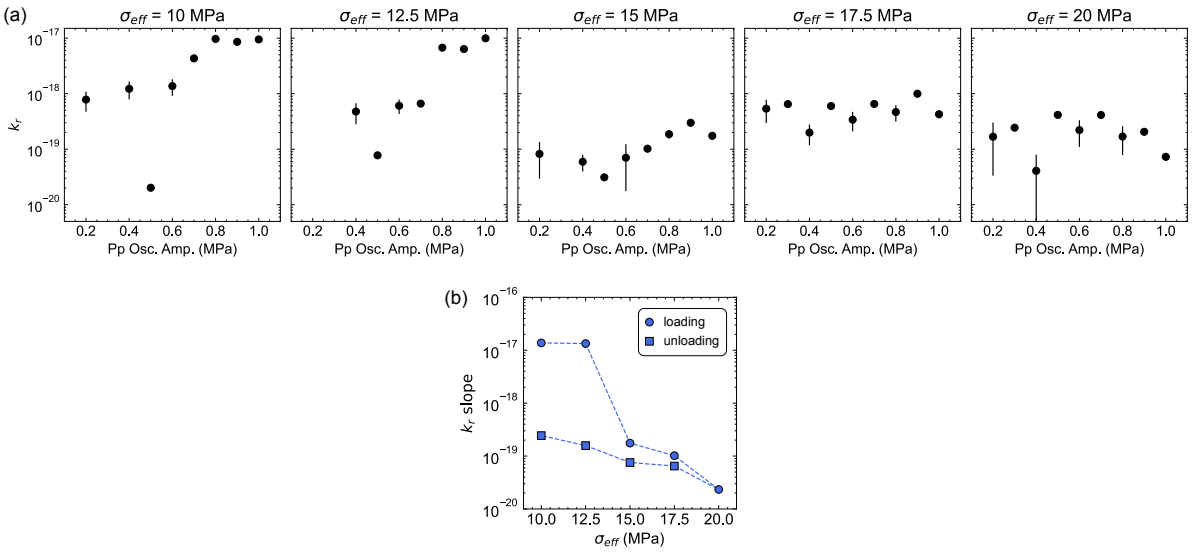



**Figure 3.14.** (a) Log-time recovery of permeability after pressure oscillations for each normal stress. The recovery rate is oscillation amplitude-dependent at lower stresses ($< 15$ MPa), but not at higher normal stresses ($> 12.5$ MPa) and with relatively little change up to the largest normal stress (20 MPa). (b) Slopes of $k_r$ as a function of applied stress for the loading and unloading phases of the experiment.

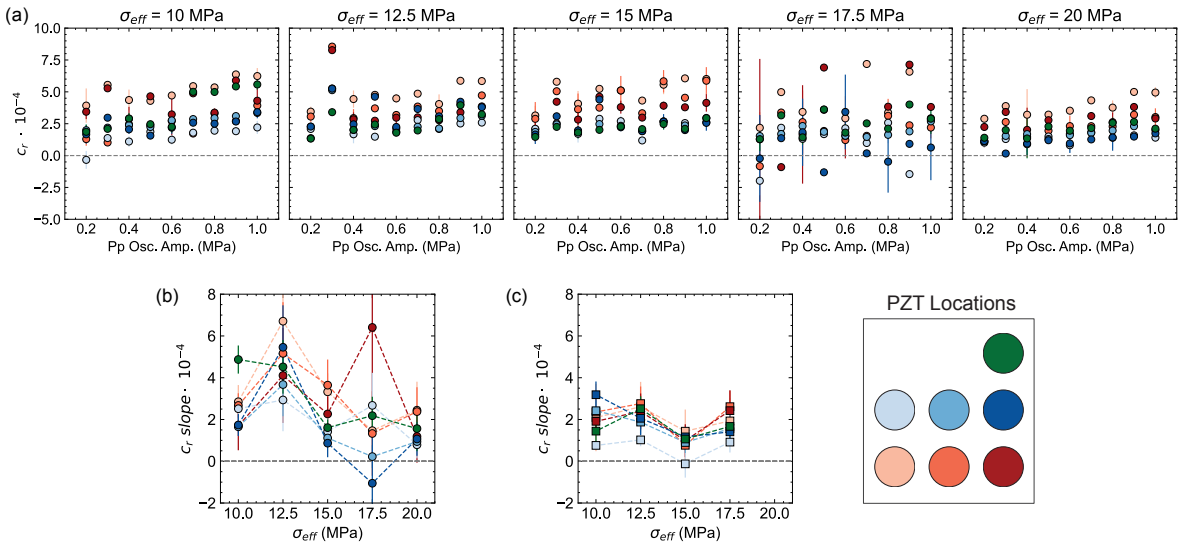



**Figure 3.15.** (a) Log-time recovery rate for all transmitter-receiver pairs. Positive values indicate a transient change to the fracture asperities and negative values indicate irreversible changes to fracture contacts. (b) The slope of $c_r$ as a function of applied stress does not seem to systematically evolve with increasing $\sigma_{\text{eff}}$. (c) Slopes of $c_r$ as a function of applied stress during the unloading phase of the experiment.

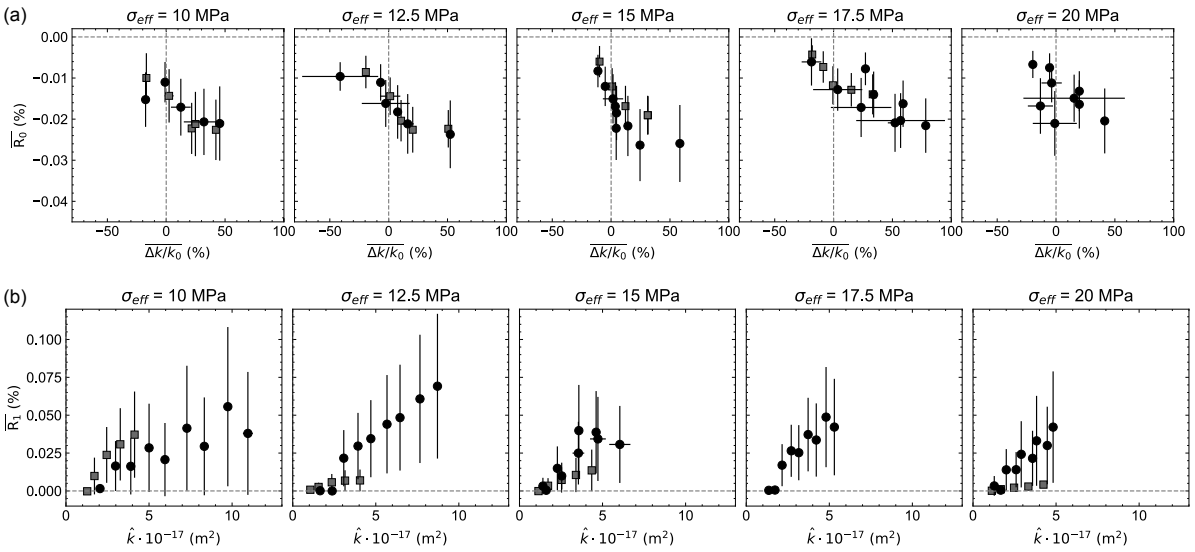



**Figure 3.16.** (a) Relation between relative changes in velocity, $R_0$, and permeability, $\Delta k/k_0$, for each normal stress level. (b) Relation between relative changes in velocity, $R_1$, and dynamic permeability, $\hat{k}$, for each normal stress level. Circle markers correspond to loading phase and square markers correspond to the unloading phase of the experiment.

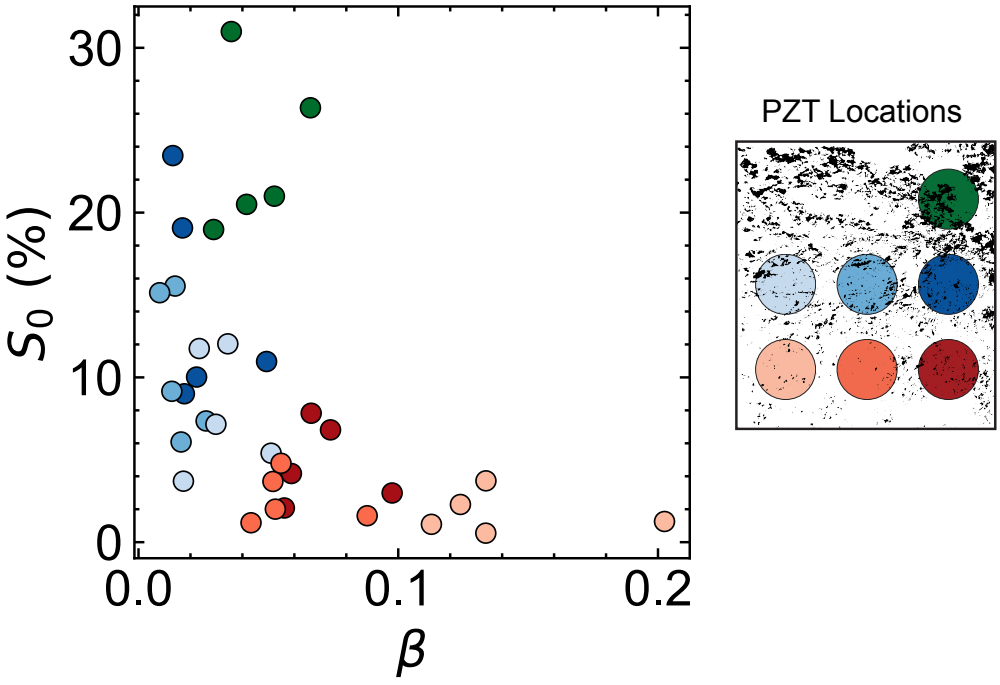



**Figure 3.17.** Regions with larger contact area ($S_0$) exhibit smaller measure of nonlinearity, $\beta$, and regions with small $S_0$ exhibit larger nonlinearity during the loading phase of the experiment.

# Chapter 4

## Multiphysics modeling of rough fracture deformation to constrain the connection between fracture stiffness, permeability, and acoustic transmission

### 4.1 Abstract

The response of hydraulic and elastic properties of the subsurface to stress perturbations is important in energy production, waste storage, and other processes. We describe an integrated lab and numerical study to elucidate the mechanisms controlling fault permeability and elastic properties in response to quasi-static stressing. In the experiments, water is injected into a rock interface subjected to triaxial loads at 10, 15, and 20 MPa while measuring permeability and ultrasonic wave properties. We oscillate the effective normal stress to evaluate contact acoustic nonlinearity (CAN) and document changes in permeability and ultrasonic wave properties with applied normal stress. We used high-resolution (µm-scale) optical profilometry to measure roughness of the rock interfaces and to obtain digital imprints of the surface contact geometry. These data were used in linear elastic numerical simulations to predict surface contact, deformation under load, and fracture permeability. For each applied normal stress, we derive permeability from the contact aperture distribution using the parallel plate approximation to the Reynolds equation and elastic transmission properties from the contact stiffness using a quasi-

static model. We make direct comparisons between the lab and numerical results to resolve the micro-mechanical links between nonlinear elastic properties of fractured rock with changes in permeability. We find that fracture surfaces are sensitive to alignment, modulating compaction, stiffness, and therefore fluid flow. Additionally, we find that the numerical fluid flow scales with fracture normalized fracture stiffness, over a range of 5 orders of magnitude of applied stress.

## 4.2 Introduction

Fracture roughness, contact area, and aperture are important geometric characteristics [82] that control the distribution of stress and both mechanical [19] as well as fluid transport properties of rock [36]. The interplay between contact mechanics and fault permeability is of significant interest in reservoir characterization [3], energy production [11], waste storage [38], and natural processes in the subsurface [79, 118]. Fault topography has been measured from experimental to natural scales ($10^{-5}$–$10^{4}$ m), and shown to be fractally self-affine [22, 90], which is widely exhibited on both natural and engineered surfaces [2].

Numerical simulations of deforming rough surfaces in contact are generally implemented with synthetic statistically-equivalent rough surfaces using methods that assume self-affine fractal geometry with a Hurst exponent $H < 1$ [23,31,60,80,120,121,129] that has been shown representative of fault geometry [22, 90]. Another common method of representing elastic rough surfaces in contact is through asperity-based models [19,23,39, 52, 80, 136], which are unable to resolve contact area and contact pressure distributions and local stiffness.

Typically these numerical approaches use and/or generate self-affine fracture or percolation-based geometries [80,87]; it is uncommon to also constrain simulation results with experimental observations [61,101]. In this study, rather than generating rough sur-

faces, we use high-resolution profilometry scans of both sides of a tensile-fractured Westerly granite specimen, assuring a "natural" roughness free of potential bias of the generation method, a rarely implemented approach [59, 136]. Furthermore, we use pressure sensitive films to measure "natural" fracture contact area, map of contacting asperities, for the same specimen scanned with a profilometer. That is to say, we have direct measurements of fracture topology; contact area, roughness, and aperture, using a variety of experimental methods and techniques. In addition to geometrical measurements of the fracture surfaces, we employ an array of ultrasonic active acoustic interrogation pairs to estimate the local changes in elastodynamic response on the fracture interface, as well as the correspondence between normal stress levels, fault permeability, and ultrasonic characteristics. Here we show comparisons between experimental and numerical results and provide insights into dominating mechanisms responsible for our key experimental observations.

## 4.3 Methods

### 4.3.1 Experiment

We use observations of stress, deformation, permeability, mechanical stiffness and active source ultrasonic monitoring [125] to constrain multiphysics numerical models of fracture aperture deformation and fluid transport. Experiments are conducted on an L-shaped block $69 \times 45 \times 50 \times 26$ mm of Westerly granite cleaved in Mode I to create a quasi-planar "natural" fracture. We measure the elastodynamic and fluid flow response of the fractured sample at triaxial stresses (10 –20 MPa) with superimposed oscillations in pore fluid pressure (0.2 –1.0 MPa amplitude, experiment p5483). Custom loading platens with an array of embedded piezoelectric transducers (PZTs) and distributed internal fluid ducts allow the concurrent measurement of transmitted ultrasonic and fluid flow

properties. The PZTs are 0.635 mm diameter, p-polarized, and have a central frequency of 500 kHz. Details of the experimental apparatus and data acquisition are available in [67, 105]; and [125, 126]. Additional experiments used pressure-sensitive films to estimate real areas of the contacting asperities in the re-mated specimen under different stress levels –see [125] for further details. We connect our results from active acoustic monitoring (wave velocity and RMS amplitude), permeability and fracture roughness via numerical models that include contact geometry and deformation.

### 4.3.2 Surface profilometry and digital alignment

Post-experiment, the fractures were optically profiled (Keyence VR 3200 optical profilometer at 50x magnification in wide-field mode) at a lateral resolution of 11.758 µm and over $\approx$ 20 cm$^2$ for each side, allowing us to resolve fine details of the roughness (Figure 1). Figure 4.1c shows 3D topographies of surfaces $h_1(x, y)$ and $h_2(x, y)$ on either side of the fracture interface, respectively.

Before numerical modeling, the digital profiles were processed to resolve the following: undefined heights (missing) in the roughness profile, differences in areal extents of the two scans (offset on both sides of the fracture), absence of an absolute reference between the surfaces, spurious high-frequency noise in measurements and minute tilts ($z$–direction) of each surface. To address these points, undefined heights are first estimated and filled through linear interpolation, followed by 2D cross-correlation of $h_1(x, y)$ and $h_2(x, y)$ to determine the "lateral phase lag" ($xy$ –misalignment). To correct for the "rotational phase lag", misalignment, the surfaces are mapped into cylindrical coordinates, $h_1(\rho, \varphi)$ and $h_2(\rho, \varphi)$, before cross-correlation. Sub-pixel lateral and rotational alignment corrections are not considered.

The resulting matched fracture aperture, or "gap height" distribution, is shown in Figure 4.1c, after removing lateral and rotational misalignment, which is simply

$h_{\text{gap}}(x,y) = h_1(x,y) - h_2(x,y) + C_{\text{gap}}$, with the scalar $C_{\text{gap}}$ ensuring that $\min(h_{\text{gap}}(x,y)) = 0$. To remove high spatial frequency noise, we applied a 2D Gaussian filter of $\sigma = 2$ pixels $\approx 24$ µm. Further corrections include removing tilt from the out-of-plane ($z$-) direction, either for each surface or for the fracture aperture. This is achieved by using linear regression to fit a plane to the fracture aperture and subsequently subtracting the best-fit plane from the surfaces to minimize the RMS height of $h_{\text{gap}}(x,y)$. Figure 4.2a and b qualitatively show the similarity between the fracture aperture, $h_{\text{gap}}(x,y)$, and a binarized image of a pressure-sensitive film of the fractured Westerly granite sample under 10 MPa used in experiment p5483.

### 4.3.3 Elastic contact simulation

With the pre-processed *digital representation* of the Mode I fractured rough equivalent surface $h_{gap}(x,y)$, we employ a spectral boundary integral method [34, 114] to solve for the full fields of contact stress and displacement. We follow the assumptions of Hertzian contact [44, 53], where the contact is frictionless and non-adhesive between two non-conforming elastic half-spaces with Young's moduli and Poisson's ratios of $E_1, \nu_1$, and $E_2, \nu_2$, respectively. Here, each side of the fracture is the same material, so $E_1 = E_2$.

These assumptions allow us to solve for the first-order approximation of the contact problem without numerical instabilities and achieve convergence in the solutions (see Supporting Information). We have followed the common strategy of considering the contact between between two nominally flat rough surfaces as a rigid composite rough surface as defined by $h^*(x,y) = h_2(x,y) - h_1(x,y) + C' = C^* - h_{\text{gap}}(x,y)$ (with $C'$ and $C^*$ ensuring $\min\left(h^*(x,y)\right) = 0$), impinging on a flat elastic half-space with effective Young's modulus [53] of

$$E^* = \frac{E_1 E_2}{E_2(1-\nu_1) + E_1(1-\nu_2)} \ . \tag{4.1}$$

This simplification halves the complexity of the contact model accelerates the numerical

solution. The boundaries of the contacting rough surface are assumed to be periodic due to the nature of the spectral method [114,123]. The solver iteratively refines the solution to match the average fracture stress to a target applied stress. We use measurements of Poisson ratio and elastic modulus for Westerly granite made by [8] as material inputs for our numerical simulations. In section 4.5.2, we conduct a parametric study of the effect of varying these parameters.

### 4.3.4 Energy-based tilt refinement

Since the granite sample was "naturally" fractured in Mode I [125], roughnesses are unconstrained and wavelengths close to, or longer than the sample, are evident. This feature compromises the standard tilt removal technique described in the previous section to establish a uniform contact stress distribution, as shown in Figure 4.2a. The imprints from the pressure-sensitive film (Figure 4.2b) show a primarily uniform contact footprint across the entire fracture interface –requiring a second-order refinement in surface tilt to correct for inconsistency between our contact model and experiments. We use the principle of minimum potential energy and propose an energy-based tilt refinement method. The tilt-refined rough surface $h(x, y, \mathbf{a}) = h^*(x, y) + h'(x, y, \mathbf{a}) + C$ is the composite surface superposed with a tilt plane $h'(x, y, \mathbf{a}) = a_0 x + a_1 y$, in which $\mathbf{a}$ is an array containing the two variables, $a_0$ and $a_1$ that define the normal to the tilt plane, and $C$ enforces $\min\left(h(x, y, \mathbf{a})\right) = 0$. The optimal tilt plane is then found by minimizing the surface strain energy under an invariant load ($\overline{\sigma}_n = 0.01$ MPa)

$$\mathbf{a}_{\text{opt}} = \underset{\mathbf{a}}{\operatorname{argmin}} \frac{1}{2} \iint_S \sigma_n(h(x, y, \mathbf{a}), \overline{\sigma}_n)\delta(h(x, y, \mathbf{a}), \overline{\sigma}_n)\, \mathrm{d}s, \tag{4.2}$$

where $\sigma_n$ and $\delta$ are solutions for the full field contact stresses and displacements from the elastic contact solver The optimal solution that yields minimum surface strain energy $\mathbf{a}_{\text{opt}}$ is then substituted into $h(x, y, \mathbf{a} = \mathbf{a}_{\text{opt}})$ and adopted as a tilt-corrected solution for

further simulations and analyses, as shown in Figure 4.2c.

### 4.3.5 Fluid flow simulation

Following [49], we employ the finite difference method to simulate fluid flow between two parallel plates using the Reynolds approximation. Assuming that the fluid (water) is incompressible, the two-dimensional steady state flow equation [91] simplifies to

$$\frac{\partial}{\partial x}\left(\frac{b_h^3}{12\mu}\frac{\partial P}{\partial x}\right)+\frac{\partial}{\partial y}\left(\frac{b_h^3}{12\mu}\frac{\partial P}{\partial y}\right)=0\ , \tag{4.3}$$

where $b_h$ is the local gap height (aperture) $\tilde{h}_{\text{gap}}(x,y)=h_{\text{gap}}(x,y)-\delta(x,y)$ under loading. We impose boundary conditions in accordance with experiment p5483, with no flow on the left and right sides while applying upstream and downstream pressures of 2.6 MPa and 1.4 MPa, respectively, creating a 1.2 MPa pressure differential. We then solve for $P(x,y)$ using finite difference method. The volumetric flow rate, $Q(x,y)$, is calculated from the solution of $P(x,y)$ using the cubic law,

$$Q(x,y)=\frac{b_h^3(x,y)w}{12\mu l}\Delta P(x,y)\ , \tag{4.4}$$

where $l$ is grid length in the downstream direction, $w$ is the grid width perpendicular to flow , $\Delta P$ is the fluid pressure differential, and viscosity of water at 20°C $\mu = 8.9\times 10^{-4}$ Pa s. In order to accelerate the numerical solution, we down-sampled the input $b_h(x,y)$ by a factor of 4, for a large saving in computational time without compromising accuracy.

## 4.4 Results

### 4.4.1 Elastic deformation

As previously described, aligned profiles of the two sides of the fracture are converted into a composite surface, then used as the input for simulating the Hertzian elastic deformation. We first simulate the deformation of the rough surfaces in contact at nominal applied stresses within the range of experiment p5483 (10 –20 MPa) and then extend applied stresses to encompass a larger range. The latter results are then compared with other numerical approaches and loading conditions. Figure 4.2a shows a binarized image of a pressure-sensitive film imprint of the fractured Westerly granite sample under 10 MPa used in experiment p5483. Qualitatively, there are many similar features between the topology of the digitally constructed fracture aperture (see Figure 4.1e) and the pressure-sensitive film imprint - in particular the 3 mm wide gap extending $\sim$ 12 mm along the fracture length. The pressure sensitive film provides a unique physical constraint to our numerical simulations and, to the knowledge of the authors, has not been implemented in this fashion before.

Clearly, local stresses are sensitive to interface roughness and spatial deviations. This is illustrated in Figure 4.2a and c, which show the normal stress distribution, $\sigma_n(x, y)$, from the elastic contact simulation across the fracture surface at a nominally applied stress of $\overline{\sigma}_n$=10 MPa. In both cases, the asperities, small contacting regions, experience large stresses several orders of magnitude larger than the nominally applied stress. Stresses on asperities can reach magnitudes near or beyond the yield strength of Westerly granite at higher applied stresses –and thus violating the elastic contact mechanics assumed for the models. In Figure 4.2a, the spatial distribution of stress is heterogeneous before tilt refinement, leaving the top right quadrant of the fracture plane with few asperities in contact. Using the pressure-sensitive film as a heuristic,

simply removing the out-of-plane tilt by subtracting the best-fit plane from the surface is evidently insufficient. Figure 4.2c yields a more uniform distribution of asperities in contact after the tilt refinement compared to that of the stress distribution in Figure 4.2b. Naturally fractured surfaces contain more low (spatial) frequency roughness, which may dominate tilt correction using a method of a best-fit plane. These qualitative observations are summarized in Figure 4.2d, which shows the density distributions of $\log_{10}(\sigma_n)$ for quadrants of the fracture surfaces, emphasizing that our new approach of tilt refinement by minimizing the strain energy produces a more uniform stress distribution.

### 4.4.2 Fluid flow

The other output from the elastic contact modeling is the displacement field, $\delta(x, y)$, which directly affects the aperture for fluid flow. Figure 4.4a shows the compaction across the fracture plane at a nominally applied stress of $\overline{\sigma}_n = 10$ MPa. Most of the deformation is concentrated on small asperities across the fracture interface. Figure 4.4b shows that flow occurs predominantly in conduits that align along the direction of flow ($y$–direction) and form around contacting asperities –this flow generally concentrates in regions with higher $h_{\text{gap}}$ (Figure 4.1e). The flow distribution reveals some anastomosing flow paths along the direction of flow, but the velocity distribution is saturated by the large flow rate in the gap located between 11–14 mm along the base of the fracture plane.

### 4.4.3 Comparing numerical and experimental fluid flow results

We compare our numerical modeling of fluid flow to experiments by simulating the fluid flow through deformed synthetic apertures at applied stresses in the range of experiment p5483, i.e., 10–20 MPa. Figure 4.5a shows the experimentally measured flow rate as a function of normal stress, with nominal values on the $y-$axis (left) and relative change on the $y-$axis (right). Note the large decrease in flow rate as normal stress increases

from $\sigma_n = 10$ MPa to 12 MPa. Cycled loading also reveals a marked hysteresis in flow from loading (circle markers) to unloading (square markers) – again indicative of the presence of non-ideal elastic and linear-flow response in real fractures. The average flow rates from the numerical simulations (Figure 4.5b) are orders of magnitude higher than those observed experimentally (Figure 4.5a), but also decrease with applied stress in a nonlinear fashion. However, the relative change in flow rate, $\Delta Q/Q_0$, closely matches experimental observations during the unloading phase of the experimental data. We discuss this lack of consistency between the absolute flow rates for the real and virtual samples in the following as potentially resulting from lateral mismatch in the re-mating of fractures– where a small mismatch of $\sim$1 mm may result in a large difference in virtual flow rate.

### 4.4.4 Fracture Interface Stiffness and Contact Acoustic Nonlinearity

One objective of this work is to elucidate the physical mechanisms responsible for the nonlinear elastic response of fractured rock (media) to dynamic stressing. To that end, we calculate the distribution of stiffness across the fracture interface and investigate how it relates to the experimental measurements of fracture stiffness (through ultrasonic transmission). Figure 4.6a shows the average interface stiffness, $\langle\kappa\rangle$, as a function of applied stress from numerical modelling. We define average interface stiffness as:

$$\langle\kappa(x,y)\rangle = \left\langle \frac{\sigma_n(x,y) - \sigma_{\text{ref}}(x,y)}{\delta(x,y) - \delta_{\text{ref}}(x,y)} \right\rangle . \tag{4.5}$$

In this case, we define the reference model for each nominal applied stress of $\overline{\sigma}'_n$ with $(\overline{\sigma}'_n - 0.1)$ MPa applied stress and calculate the resulting stress $\sigma_{\text{ref}}$ and displacement fields $\delta_{\text{ref}}$. A linear relationship is expected as the result from a purely elastic contact

model. To connect this to experimental observations, we average the interface stiffness within each transmitter-receiver footprint (see Figure 4.6b). Overall, stiffness increases nearly linearly with stress within these regions and heterogeneously across the fracture plane. Additionally, we estimate fracture stiffness from experimental data (p5346 and p5356 from [67] with same Westerly granite specimen) using the following relation as described by [57, 74, 86, 102]:

$$T = \frac{A_f}{A_i} = \frac{2\kappa}{\sqrt{(\rho\omega c)^2 + (2\kappa)^2}}. \tag{4.6}$$

In this formulation, transmission coefficient, $T$, is proportional to the transmitted wave amplitude, $A_f$, propagating through a mechanical discontinuity, normalized by the amplitude through an intact specimen, $A_i$. It is then trivial to solve for stiffness, $\kappa$, with density, $\rho = 2414$ kg/m$^3$, angular frequency, $\omega = 3.14$ MHz, and wave speed, $c = 4000$ m/s, measured from experimental values. Figure 4.6c shows the estimated fracture stiffness increases nonlinearly as function of applied stress (bottom center transmitter-receiver pair). We observe that the fracture stiffnesses calculated from our numerical simulations, for $E = 70$ GPa and $\nu = 0.23$, are smaller than the fracture stiffness estimated from experiments, $\sim 1.25 \cdot 10^{12}$ Pa/m. Within the transmitter-receiver footprints, we observe that the stiffness increases nonlinearly with applied stress, Figure 4.6c, and that regions with fewer asperities in contact are stiffer. The difference in absolute value between simulation and experiments is influenced by material properties inputs, $E$ and $\nu$, and potentially by assumptions in this contact model, i.e. purely elastic and neglects interactions such as adhesion and friction.

Though the contact model contains some simplifications, the stiffness values are reasonable [8]. Furthermore, we seek to understand the role of local roughness/aperture on the nonlinear elastodynamic response of fractured rock. We calculate the stress and displacement fields cycled to $\pm$1MPa in increments of 0.1 MPa and around nominal

applied stresses of 10, 15, and 20 MPa. The fracture is under extension when $\Delta\sigma_n < 0$ and compression when $\Delta\sigma_n > 0$.

In Figure 4.7, we show a side-by-side comparison between relative changes in flow rate ($\Delta Q/Q_0$), time delay ($\Delta t/t_0$), and transmission coefficient ($\Delta T/T_0$) from numerical simulations, left, and experiment, right. For each parameter, the results from applied stress levels of 10, 15, and 20 MPa are overlain. In Figure 4.7a and b, the relative change in flow rate decreases with increased stress level, but the magnitude of these changes are dissimilar between simulation and experiment. This discrepancy could be influenced by our choice of input parameters for the simulation, elastic modulus and Poisson ratio, or alternatively, that flow was not steady-state during the pore pressure oscillations of the experiment. The relative change in time delay (Figure 4.7 c and d) show a similar trend with increasing normal stress between simulation and experiment but a large difference in absolute values. Again, simulation input parameters $E$ and $\nu$ and analytical inputs for CAN ($\rho$, $c_p$, $\omega$) would influence the magnitude of $\Delta t/t_0$, but not likely by two orders of magnitude. We posit that these parameters are highly sensitive to the interface stiffness and may be influenced by damage to and remnant comminuted products adjacent to the asperities and within the fracture void. Although the relative change in transmission coefficient and RMS Amplitude are not directly comparable, their relative changes ($\Delta T/T_0$ and$\Delta A/A_0$) should be similar. Figure 4.7d and e compare the change in transmission coefficient from simulation results and change in RMS Amplitude from experimental results, which show systematic similarities that the slope of each decreases with increased stress state. Overall, our observations demonstrate that the fracture interface becomes stiffer at high stresses which results in smaller changes in flow rate and elastic softening. However, in all of the experimental results we observe an instantaneous response to the stress oscillation, which we interpret as an elastic softening. Since there are many simplifications in the numerical simulations (e.g. quasi-

static, linear elasticity, and frictionless contacts) we are unable to reproduce these more complex behaviors found in the experimental observations. Despite these limitations, we are still able to capture how fracture interface stiffness can modulate hydraulic and elastic responses to stress perturbations.

To summarize the above observations: (a) Relative change in flow rate $\Delta Q/Q_0$ as a function of normal stress; the lower applied stresses yield larger changes in flow rate. (b) Relative change in interface stiffness $\Delta\kappa/\kappa_0$ as a function of applied stress. The fracture interface is relatively stiffer during compression and compliant during extension. Increasing normal stresses results in smaller overall stiffness. These two observations qualitatively match experimental results. (c) Relative change in transmission coefficient $\Delta T/T_0$ with increasing applied stress. (d) Relative change in phase time delay $\Delta t_p/t_{p0}$ as function of stress change. The time delay is negative (i.e. faster wave speed) during compression and positive (i.e. slower wave speed) during extension.

## 4.5 Discussion

### 4.5.1 Sensitivity to surface alignment/mating

While the relation between $\Delta Q/Q_0$, $\Delta d/d_0$ and $\overline{\sigma}_n$ of our models closely match the unloading phase in our experiment, as shown in Figure 4.5a,b one major difference lies in the drastic reduction in flow rate during the loading phase in the experiment. Similarly, there is a discrepancy between the measured experimental displacement and the average displacement from the numerical simulations, Figure 4.3. One of the hypotheses that might explain this behavior is the presence of a slight misalignment between the two surfaces at the beginning of the experiment, and their gradual realignment and re-mating to their preferred configuration as the applied load increases. The realigning and re-mating processes decrease the overall gap height and closes flow pathways of the

fracture interface. This realignment would then persist through the unloading phase, allowing the fracture interface to exhibit only the changes in $\Delta Q/Q_0$ due to elastic contact deformation, as depicted by the numerical models. To better understand the hysteresis found in experiments, we intentionally add in slight misalignment (10 - 1000 µm) between the two mated and aligned rough surfaces, i.e., $h_1(x, y)$ and $h_2(x, y)$ with alignments and refinements described in Section 2.2 and 2.4, to investigate the sensitivity of fault permeability to surface alignment. Figure 4.5c shows the average flow rate, $\langle Q \rangle$, in response to added offsets between two surfaces in $\pm x$ and $\pm y$ directions. Figure 4.3c shows the average displacement in response to added offsets between two surfaces in $\pm x$ and $\pm y$ directions. Results indicate that $< 1$ mm of misalignment in $\pm x$ or $\pm y$ directions can result in up to 500% enhancement in flow rate. Since there is no rigid fixture that limits translation parallel to the real fracture surfaces in the experimental setup, where sub-mm movement is allowed, we consider this mechanism to be highly likely responsible for the drastic reduction during the loading phase in the experiment. This result also highlights that any mechanism (experimental scale or field scale) that could induce misalignment between mated rough surfaces, such as shearing [72] or dynamic stressing [29, 32, 105, 125, 126], is likely to significantly change the fluid transport properties and interface stiffness, Figure 4.6b.

### 4.5.2 Effect of bulk elastic modulus

We explore the effect of material properties and nominal applied stress on flow rate to explore the impact of high stresses on response. Figure 4.8a shows the average flow rate as a function of applied stress over 5 orders of magnitude (10 kPa to 1 GPa) and variable elastic moduli(1 GPa to 500 GPa) representing very compliant to very stiff bulk parameters. In this parametric study, we find that the flow rate $Q$ decreases linearly with the logarithm of normal stress. This relationship breaks down for normal stresses

exceeding $\sim 10^2$ MPa, suggesting that our model is limited to a stress range less than the yielding stress of the asperities. This is also illustrated in Figure 4.8b, which shows the average flow rate as a function of fracture interface stiffness $\kappa$. Each elastic modulus, $E$ has a different power law that diverges at large applied stresses, $\kappa \approx 10^{13}$ Pa/m. Furthermore, we find that these results collapse when elastic modulus is normalized by interface stiffness, "compliance", see Figure 4.8c, suggesting that fluid transport may have a linear relationship with compliance of fractured materials.

### 4.5.3 Hydro-mechanical properties dependence on roughness

Thus far, we have presented results from simulations and compared them to experimental observations. Additionally, a parametric study that modulated bulk elastic properties allows us to explore a range of rock types and stress conditions, depths in the subsurface. A key question is how our numerical model can scale from lab to field. Rather than using a correlation length to measure roughness, we choose to characterize the surface with fractal dimension, calculated from a power spectral density as a function of wave number, of our aperture under different magnitudes of deformation. Figure 4.9a shows the fractal dimension, $\langle D \rangle$, averaged over the $x-$ and $y-$ directions as a function of applied stress. We observe that the composite fracture surface, aperture, is self-affine and the fractal dimension $D$ increases slightly across 5 decades of applied stress for different material properties (elastic modulus and Poisson ratio). This highlights the importance of fracture/fault roughness, in addition to bulk elastic properties on mechanical deformation. Also, this demonstrates that as a fractured rock experiences greater stresses, more asperities come into contact and therefore increase a shear force necessary for slip. Furthermore, we attempt to relate the scale-invariant mechanical properties of the deformed fracture to fluid transport properties in Figure 4.9b, which show the fractal dimension as a function of permeability, where $k = \frac{Q\mu}{\Delta P l}$. We observe a correlation between fractal

dimension $D$ and permeability $k$ linearly correlated, where $k$ increases with decreasing $D$. This, again, highlights the importance of roughness (contacting asperities) and the degree to which it modulates fluid flow. We posit that the small range in permeabilities is likely influenced by the elastic contact model, whereas elasto-plastic could account for a larger span in values. However, fluid flow is also influenced not only by fracture aperture geometry, but other first-order effects such as viscosity, hydraulic head, and wear products.

## 4.6 Conclusion

In our unique study, we present a multiphysics model of fracture deformation and fluid flow that is constrained by experimental measurements through pressure-sensitive films, fracture permeability, and active acoustics. Alternative to generating a synthetic rough surface via fractal geometry, Hurst exponent, or percolation, we scanned a tensile fractured Westerly granite specimen, used in experiments, with a high resolution profilometer to reconstruct a composite aperture digitally. Before this can be used as an input for our numerical modeling, these surfaces are aligned and then implement a novel energy-based tilt refinement method to ensure a proper mating and uniform stress distribution.

This composite aperture is deformed using an elastic contact model where deformation is influenced by neighboring regions, as opposed to an ensemble, statistical, "asperity-based" approach. Fluid flow is then solved across the deformed fracture aperture based on a hydraulic cubic law. We find that our numerical simulation does not reproduce the fluid flow rate as measured in experiments, but the relative change in flow as a function of a applied stress matches very well. Additionally, we posit that the hysteretic relationship observed in experiment is likely dominated by minute evolution in fracture surface alignment.

Furthermore, the elastic deformation model reveals how fracture stiffness hetero-

geneity may influence acoustic transmission results in experiments. However, since this contact model is purely elastic and neglects surface effects such as friction, we are unable to reproduce higher order nonlinearity mechanisms found in dynamic stressing, elastic softening, and hysteresis. A parametric study in which bulk properties, elastic modulus and Poisson ratio, were modulated for a range of 5 decades of applied stresses demonstrates that fluid flow is linked to the compliance of the fracture interface. Since this range of data collapse on each other, we consider this to be a proxy for a range of rock types at different stress states or subsurface depths. Finally, we characterize the fractal geometric roughness, show that it remains nearly invariant across the large range of applied stresses and relate it to fracture permeability, with respect to elastic and applied stresses.

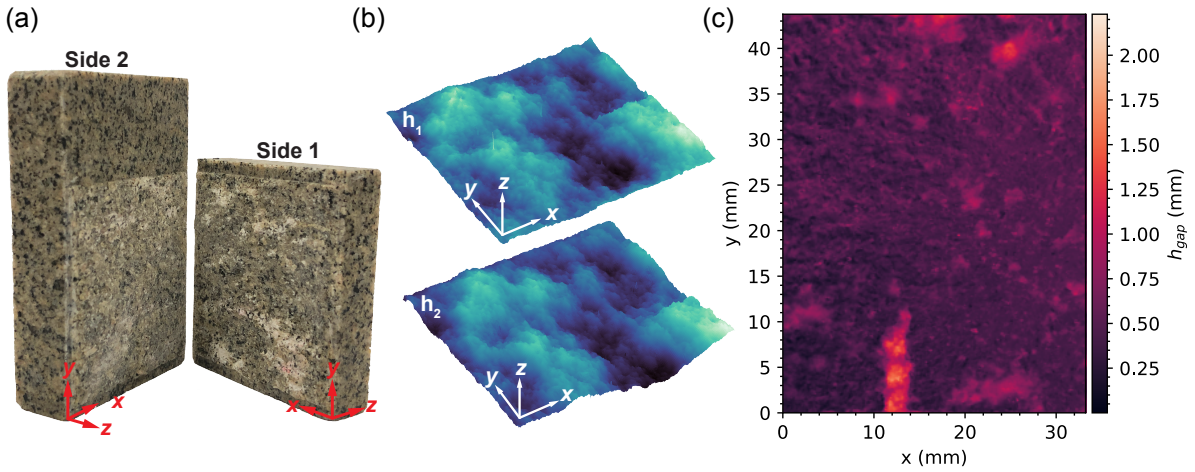



**Figure 4.1.** (a) Photographs of side 1 and side 2 of a tensile-fractured Westerly granite specimen. (b) High-resolution profilometry of both sides, $h_1(x, y)$ and $h_2(x, y)$, of the tensile fractured Westerly granite sample. (c) Composite aperture and gap height distribution (at 0 stress) constructed from digitally aligning both surfaces by cross-correlation between $h_1(x, y)$ and $h_2(x, y)$. Voids are filled through linear interpolation (or nearest neighbor).

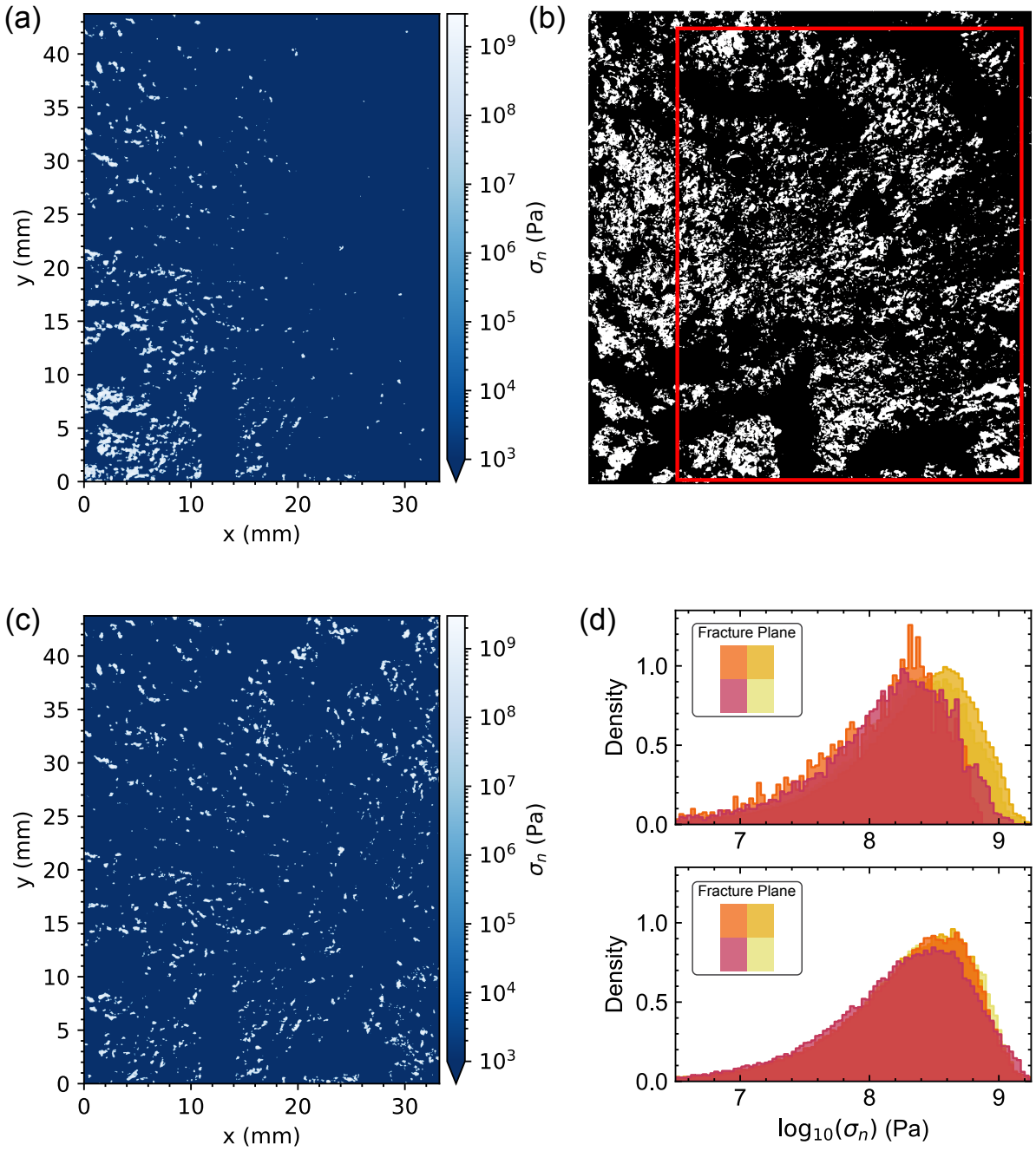



**Figure 4.2.** (a) Stress distribution, $\sigma_n$, from elastic contact simulation across the fracture interface at a nominally applied stress of 10 MPa. (b) Binarized image of a pressure-sensitive film of the fractured Westerly granite sample used in experiment p5483. Red box indicates the region where fracture surfaces were scanned and then digitally aligned. (c) Stress distribution from elastic contact simulation at an applied stress of 10 MPa with additional tilt adjustment, which produces a more uniform pressure distribution. (d) Histograms showing distribution of stress in each quadrant of the fracture plane. Top plot shows distribution of stress with planar-fitting tilt correction and bottom plot shows distribution with the proposed energy-based tilt correction.

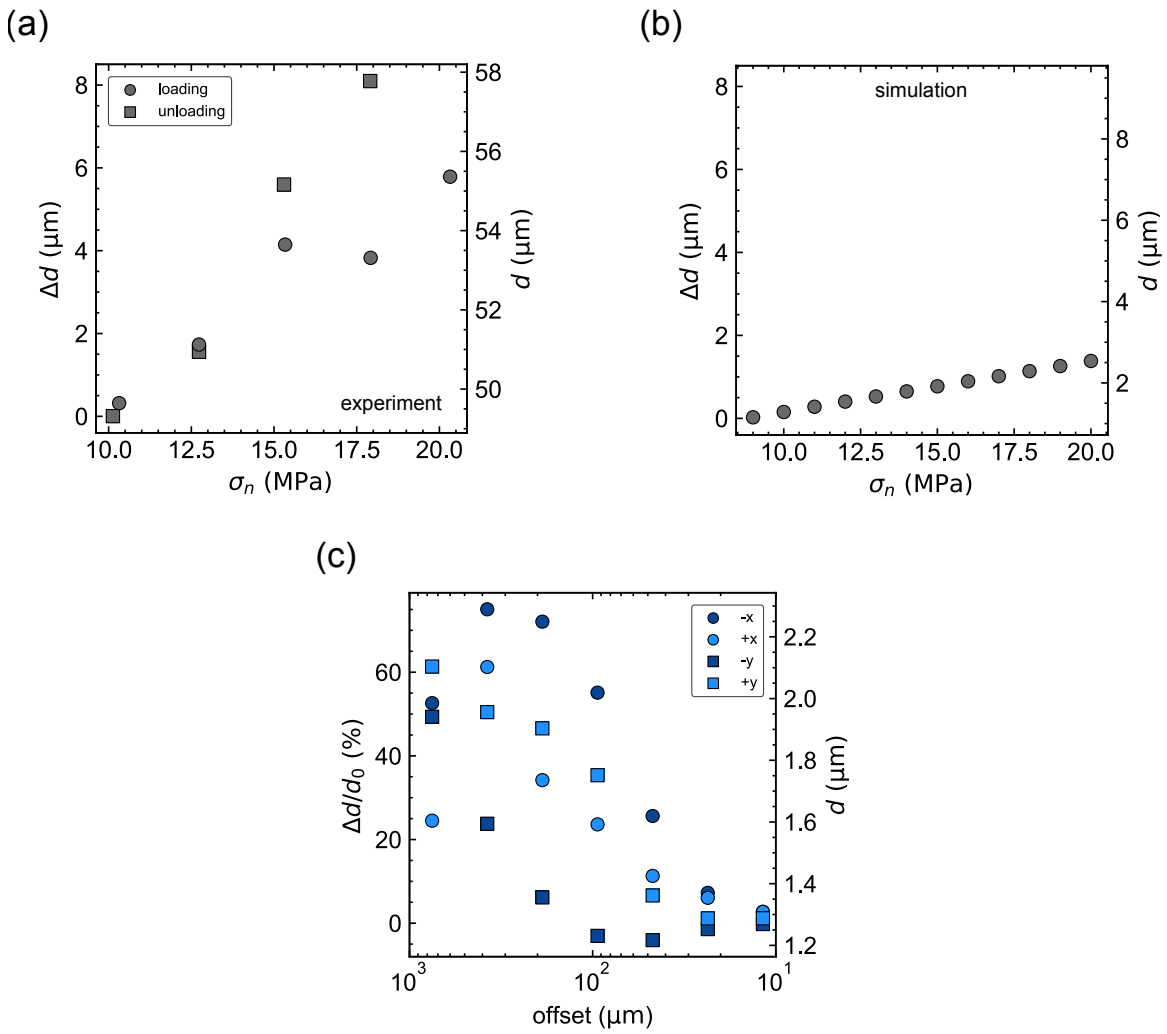



**Figure 4.3.** (a) Displacement,$\delta$, as a function of applied normal stress from experiment. (b) Bulk displacement, $\delta$, from applied normal stress from contact simulation. (c) Numerical average displacement as a function of misalignment between the fracture surfaces in the $\pm x, \pm y$ directions.

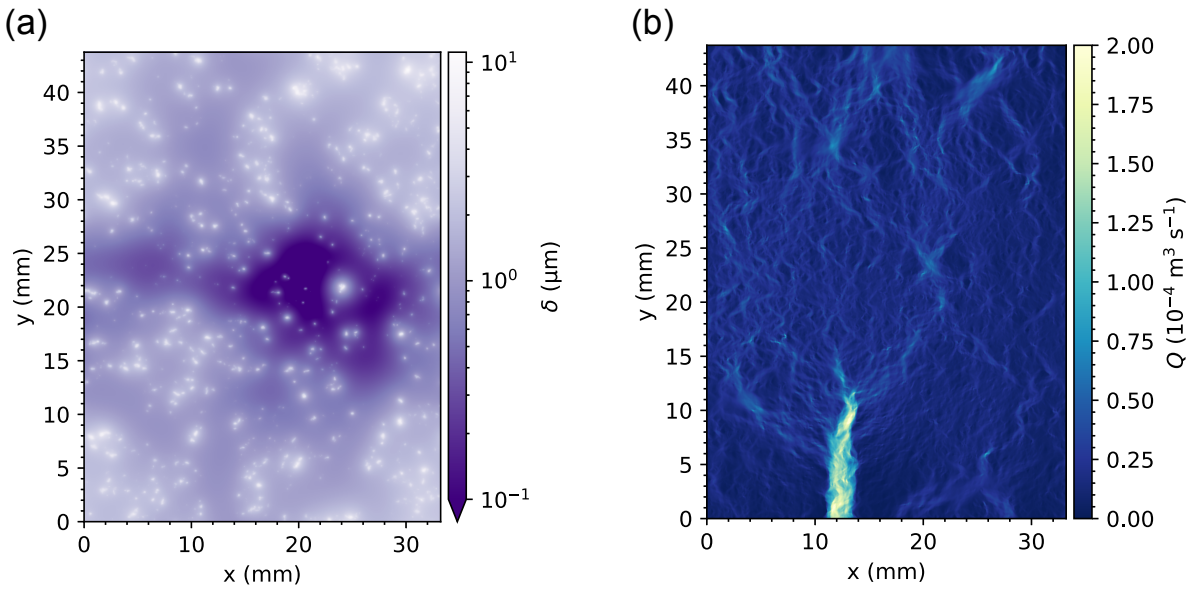



**Figure 4.4.** (a) Displacement field, $\delta$, derived from elastic contact simulation at a normal stress of $\sigma_n = 10$ MPa. Note that deformation is concentrated on small asperities across the fracture interface. This deformation is subtracted from the aperture and then used as the input for modeling fluid flow. (b) Volumetric flow rate, $Q$, calculated using a finite difference method to solve Reynold's equation. We imposed boundary conditions from experiment p5483 where there is no flow on the left and right sides, the inlet pressure is 2.6 MPa and the outlet pressure is 1.4 MPa, i.e., $\Delta P = 1.2$ MPa.

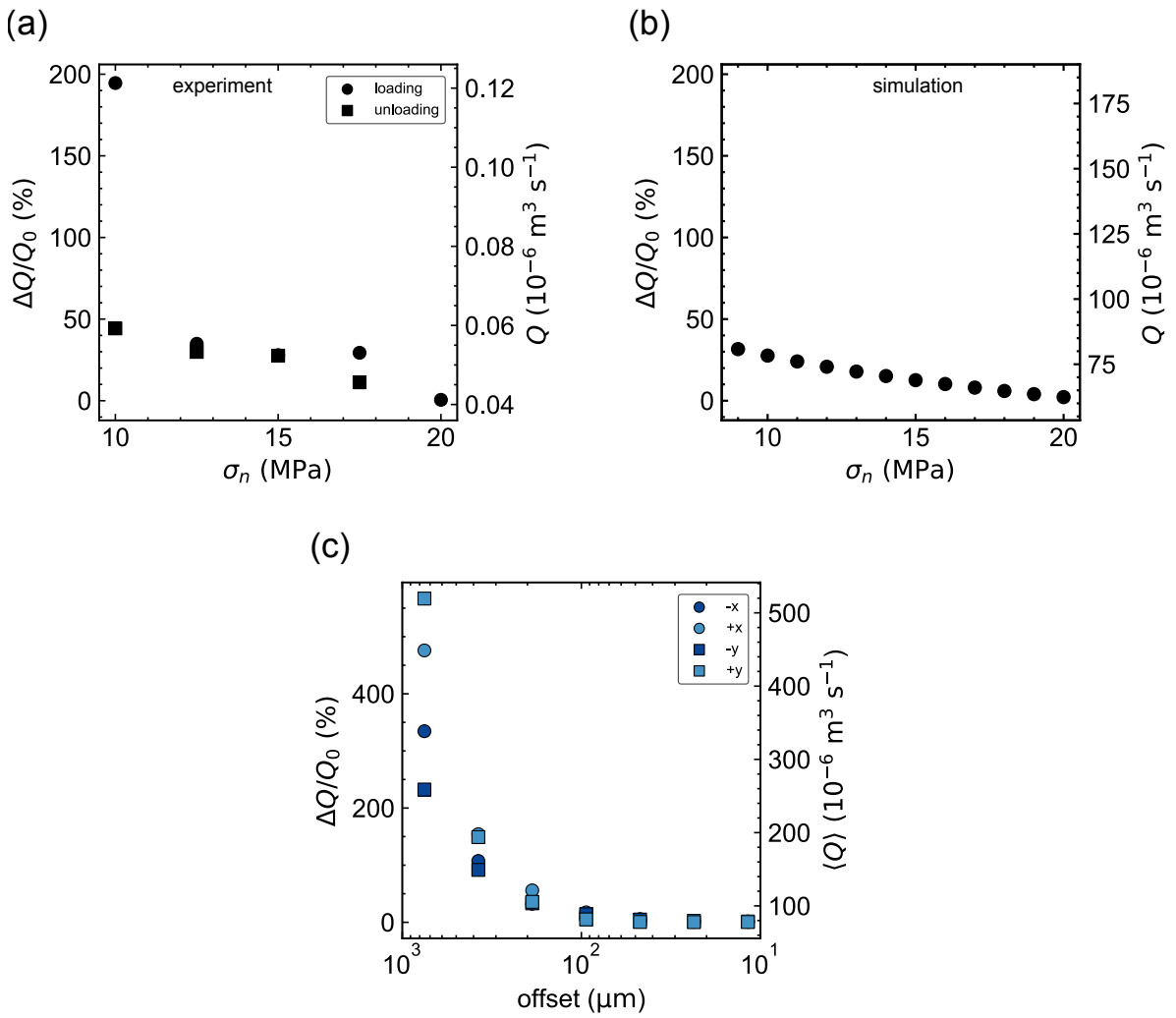



**Figure 4.5.** (a) Relative ($\Delta Q/Q_0$) and nominal flow rate ($Q$) from experiment, where $Q$ is the average of the inlet and outlet flow rates, during loading and unloading as function of applied stress. (b) Relative and average flow rate from numerical simulations nonlinearly decreases with increasing average normal stress, from contact simulations. Relative change in flow rate, $\Delta Q/Q_0$ closely matches experimental observations during the unloading phase of the experiment. (c) Numerical average flow rate as a function of misalignment between the fracture surfaces in the $\pm x, \pm y$ directions. Misalignment of $\sim 10^3$ μm leads to a relative flow rate change on order of that observed in experiments during the loading phase.

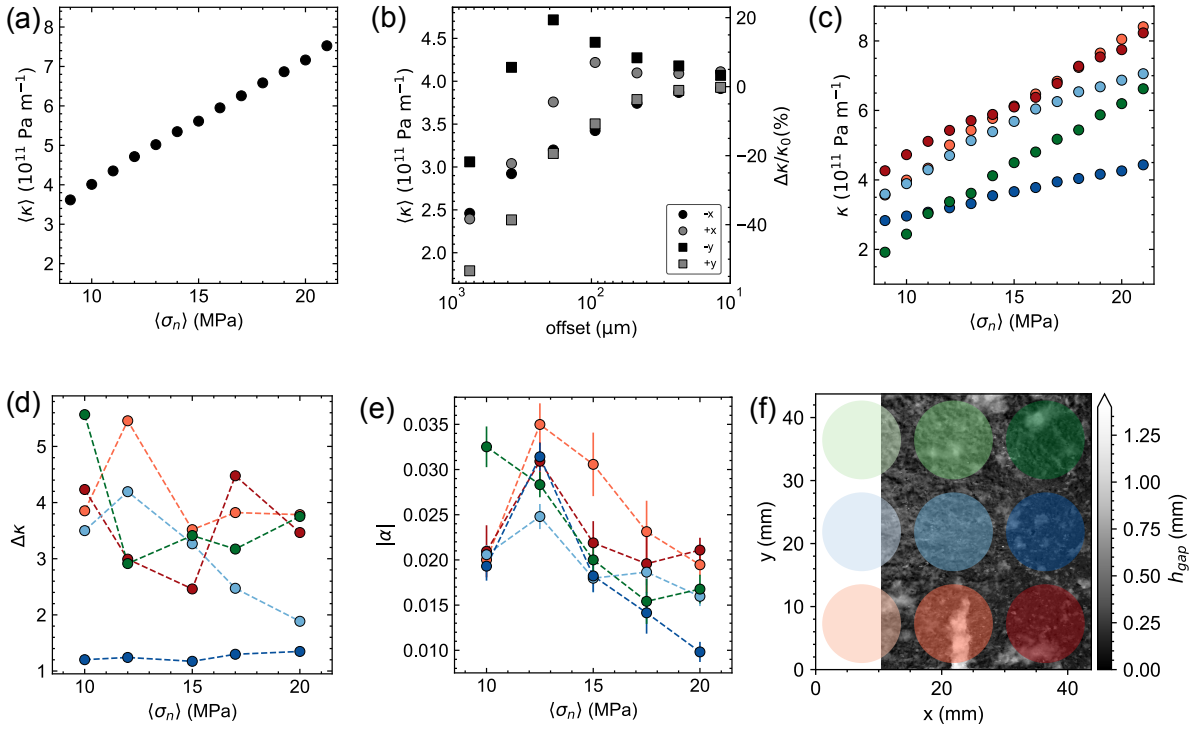



**Figure 4.6.** (a) Average fracture stiffness for a range of applied stresses used in experiment. (b) Average stiffness as a function of fracture offset in $\pm x, y$ directions. (c) Fracture stiffness within transmitter-receiver pair footprints as a function of applied stress. (d) Change in interface stiffness, $\Delta\kappa$, as a function of average stress, $\sigma_n$ within each transmitter-receiver footprint from numerical simulations. (e) Absolute value of nonlinear elasticity parameter, $\alpha$, from experiments which is related to relative change in stiffness. (f) Digital fracture aperture with PZT transmitter-receiver footprints superimposed.

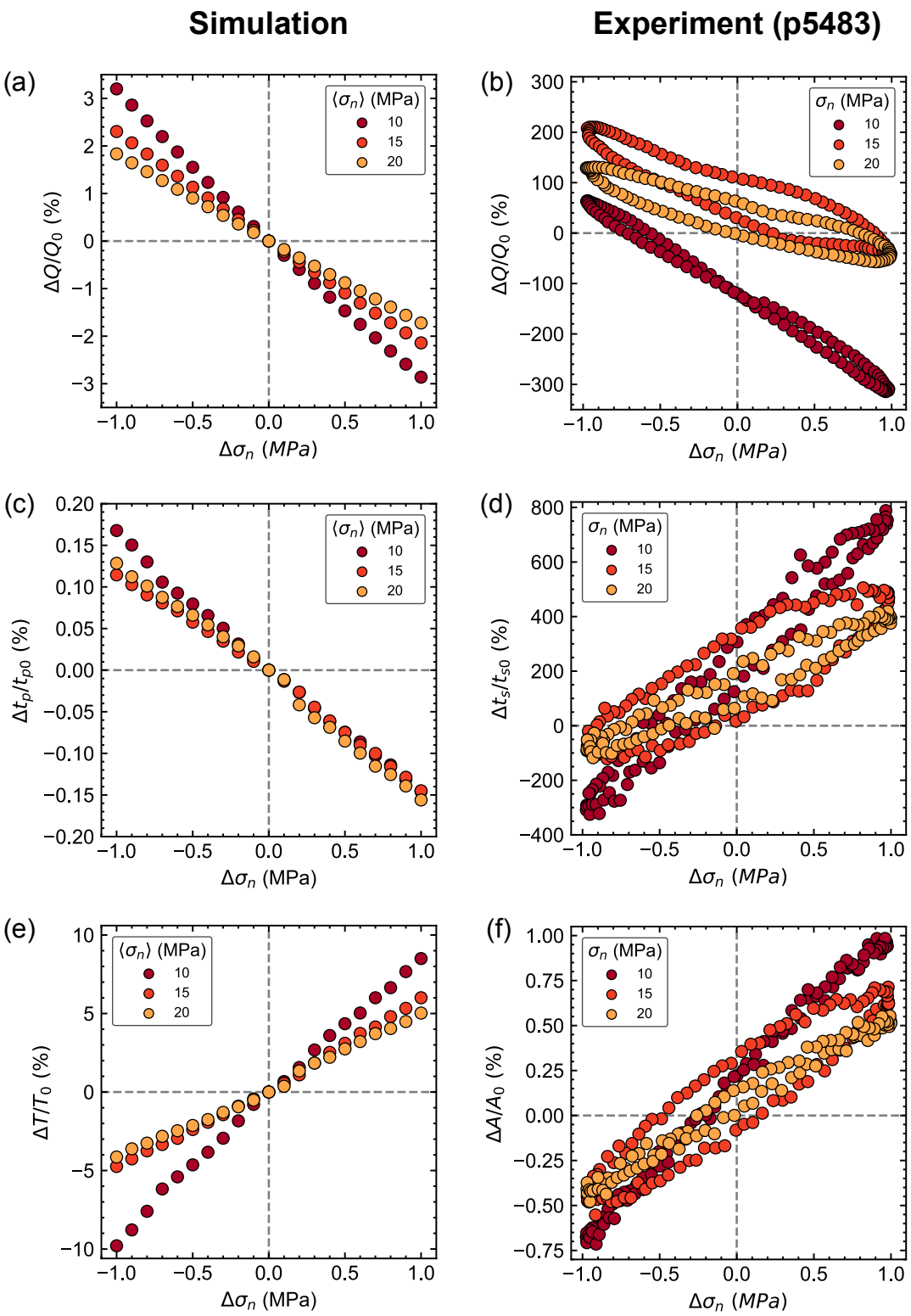



**Figure 4.7.** (a)-(b) Relative change in flow rate $\Delta Q/Q_0$ as a function of normal stress. (c)-(d) Relative change in time shift ($\Delta t/t_0$) as a function of normal stress. (e)-(f) Change in transmission coefficient $\Delta T/T_0$ and RMS Amplitude, $\Delta A/A_0$ with increasing applied stress.

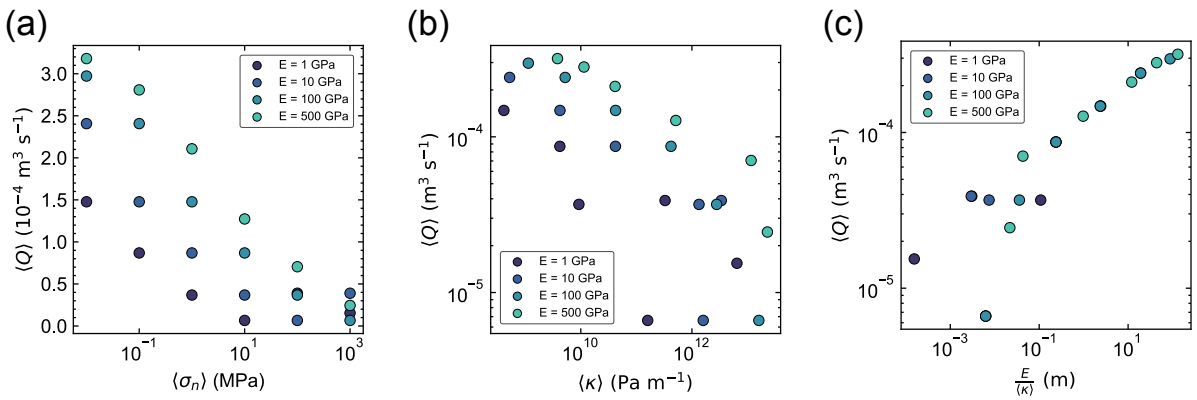



**Figure 4.8.** (a) Average flow rate as a function of applied stress over 5 orders of magnitude, for bulk elastic moduli ranging from 1 GPa to 500 GPa. For nearly all of the parameters, the flow rate $Q$ linearly decreases with the logarithm of normal stress, but diverges when normal stresses exceeding $\sim 10^2$ MPa. (b) Average flow rate as a function of fracture interface stiffness $\kappa$ on a log-log scale. Each elastic modulus, $E$ has a different power law that diverges at large applied stresses, $\kappa \approx 10^{13}$ Pa/m. (c) Average flow rate as a function of compliance, elastic modulus normalized by average fracture interface stiffness.

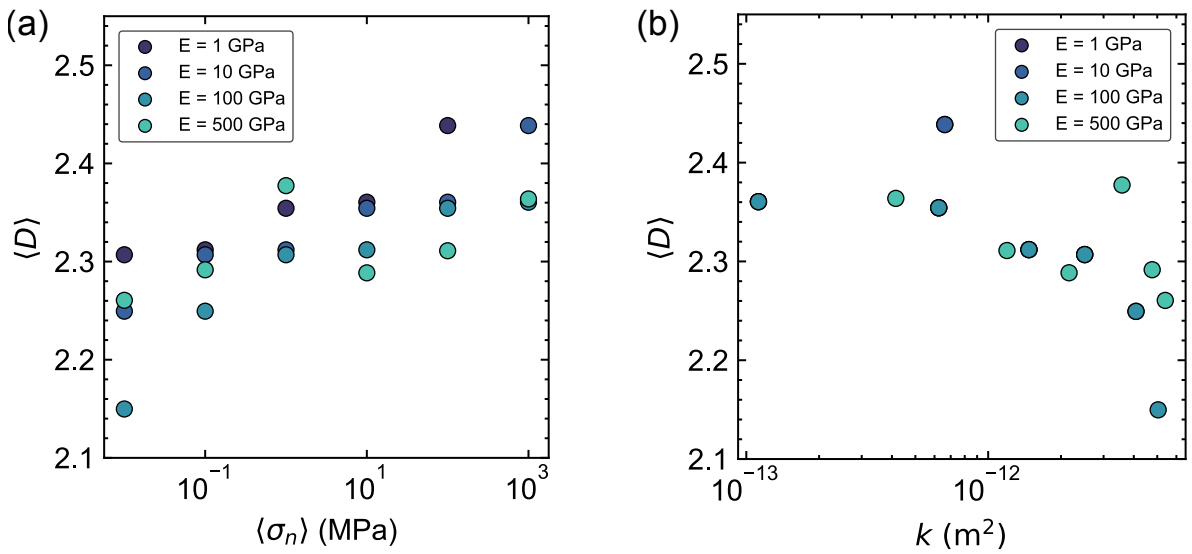



**Figure 4.9.** (a) Fractal dimension, $\langle D \rangle$, averaged over $x-$ and $y-$directions for surface deformation across 5 decades of applied stress. (b) Fractal dimension $\langle D \rangle$ as a function of fracture permeability for the 5 decades of applied normal stress and range of elastic parameters.

# Chapter 5

## Poromechanics of particle remobilization and interface stiffness of dynamically stressed fractured rock

## 5.1 Abstract

A range of natural (teleseismic waves) and industrial sources (hydraulic stimulation) of stress perturbations in the subsurface can alter the poromechanical response of fractured rock which may reactivate faults or otherwise breach reservoir seals. We describe laboratory experiments that seek to decouple the role of fracture interface stiffness and fracture infill (sediment transport) in modulating the hydraulic and elastodyamic properties of fractured rock. Experiments were conducted on a specimen of Westerly granite with uniform roughness (silicon carbide grit-roughened) and loaded under triaxial stresses in a pressure vessel while permeability evolution as measured from the flow-through of deionized water. In these experiments, thin layers of synthetic wear (gouge) material are added to the planar fracture interface with the same roughness to simulate mature, sheared, fractures whose poromechanical response is dominated by clogging and unclogging of pore throats. Oscillations of pore pressure are applied at amplitudes ranging from 0.2 to 1 MPa at 1Hz, simulating subsurface stress perturbations (from seismicity or industrial activities). Before, during, and after the dynamic stressing, a pair of piezoelectric transducers (PZTs) continuously transmits and receives ultrasonic pulses across the fracture to monitor the evolution of fracture stiffness due to the dynamic stressing.

This allows evaluation of stress-induced changes in transmitted ultrasonic wave velocity and amplitude to estimate the nonlinearity elastic of the fracture concurrent with permeability evolution. We compare the results for samples with varying amount synthetic wear (gouge) material to understand the role and evolution of fracture stiffness and clogging-unclogging mechanisms in pore throats of porous and fractured media. We find that increasing gouge layer thickness results enhanced permeability and a greater nonlinear elastic response. Thicker layers, comparable to or larger than the fracture roughness, result in no permeability enhancement and reduced elastodynamic response (more compliant interface).

## 5.2 Introduction

Dynamic stresses from energy production and wastewater injection can contribute to induced seismicity [42, 70, 71, 88, 110, 111, 119] by significantly impacting the local stress field and poromechanical properties of the subsurface. Other perturbation sources such as the dynamic strains of seismic waves can manifest oscillations in pore pressure, leading to permeability changes [15]. Other natural perturbation sources are observed to drive changes in subsurface fluid flow, permeability, such as tidal forcing [26] and [48]. The link between these field observations is that dynamic strain in the fractured subsurface manifests elastic and hydraulic transient changes that are subsequently followed by an evolution to a new steady-state. The degree to which fracture properties such as granular in-fill and roughness modulate these elastodynamic and hydraulic responses is relatively unconstrained.

A range of laboratory studies that impose dynamic stressing on a fractured/porous specimen also report similar observations of transient changes in permeability, followed by a log-time recovery [20, 30, 105, 126]. The proposed mechanism behind these observations (permeability enhancement or reduction) from field and laboratory is mobilization

of gouge particles (grains) through fractures/porous rock, described as unclogging/clogging of pore throats [16, 30, 96]. Other mechanisms that could produce similar transient jumps in permeability in fractures include: orientation of fracture to flow direction [73] and fracture geometry changes (i.e. roughness, contact area) [1, 137].

Stress perturbations in the subsurface from elastic waves propagating from earthquakes [9, 54, 99] are also associated with altering fault stability [15, 117]. The result of these stress perturbations is characterized by elastic softening (co-seismic velocity variation), usually in the shallow crust [12–14, 25, 33, 46, 62, 63, 77, 122, 127], and then followed by a time-logarithmic post-seismic recovery [12, 78]. Several experimental studies have measured "static" elastic properties of and report relations between elastic wave speed and transmission and gouge layer dilation [56, 103], contact area [133], and far-fault bulk changes [108].

Other experimental studies have implemented dynamic acousto-elastic testing (DAET) to study the nonlinear elastic response of fractured rock and granular material, rather than static elastic properties [37, 41, 55, 68, 92, 93, 105, 125, 126]. Typically, these experiments activate a rock's elastodynamic response with dynamic strains on the order of $10^{-6}$ with a pump-probe method [41, 93]. In this framework, grain boundaries, fluid flow, fracture specific stiffness, and apertures, modulate the transmitted wave velocity (decrease) and log-time recoveries. Though these studies report observations qualitatively similar to aforementioned field observations (changes in wave velocity and permeability transients), for example, there exists a need to systematically probe the elastodynamic contribution of gouge, granular material. The contribution of fracture roughness and gouge in-fill on the relation between elastic softening and hydraulic transients in response to dynamic strain is poorly understood.

In this paper we investigate the role of granular layer thickness on fluid flow and elastodynamic properties through a planar fracture and how they are related under tri-

axial stress. Also, we impose dynamic stressing, pore pressure oscillations, at a range of amplitudes to quantify hydraulic dynamic responses and transients and the nonlinear elastodynamic responses and how they are related. A planar roughened fracture specimen with varying in-fill of quartz powder was used to simulate fractures/faults containing wear material (gouge, breccia). Each experiment is performed under the same triaxial stress conditions and simultaneous continuous ultrasonic monitoring and fluid flux measurements allow for characterizing the elastic and hydraulic response to dynamic stressing. Additionally, we characterize the fracture aperture and topology using an optical profilometer and use include measurements of grain size [89]. We then relate both static and dynamic poro-elastic properties to the fracture topography (and in-fill) and posit three regimes with different dominating mechanisms.

## 5.3 Experimental Setup

We conducted a series of laboratory experiments on a saw-cut specimen of Westerly granite roughened with #80 grit Silicon Carbide abrasive compound. In these experiments, varying amounts of Min-U-Sil 40 (fine-grained quartz powder) were applied to a planar fracture interface (45 x 50 mm nominal contact area) to simulate different gouge/wear layer thicknesses. Between successive experiments, the same surface was re-roughened to ensure consistent randomly-rough surfaces. The quartz powder, gouge layer, was lightly dusted to one fracture surface and then the other surface was brought into contact, held together with a thin plastic adhesive membrane only on the sides subject to confining pressure. The sub-mm gouge layer thicknesses were were controlled by weight. Figure 5.1d shows a gallery of the gouge layers used in this experiment series. Next, the sample was placed between steel loading platens and then sealed inside a latex jacket (to separate internal pore fluid from confining fluid), see photo in Figure 5.1c. The steel loading blocks have embedded piezoelectric transducers (PZTs) and internal conduits for fluid

flow at the fracture ends (modified from [30]), Figure 5.1b.

The final sample assembly was loaded into a pressure vessel with independently servo-controlled loading axes and fluid pressures, Figure 5.1a. Mechanical displacements and stresses were measured with direct current displacement transducers (Trans-Tek Series 240 DCDT) as well as custom-built load cells and recorded by a 24-bit analog-to-digital data acquisition system at 1 kHz. The active-source ultrasonic monitoring system (Vantage$^{TM}$ Research Ultrasound) successively pulsed an array of PZTs (p-polarized and 500 kHz central frequency) and the responses were recorded at 25 MHz. The mechanical and ultrasonic data were synchronized via a trigger signal. More details regarding data acquisition from the biaxial deformation apparatus and ultrasonic system can be found in [67, 105, 125, 126].

After sample preparation and installation into the pressure vessel, the experiment commenced with the application of a normal stress of $\sim$ 10 MPa followed by a confining pressure of $\sim$ 5 MPa. Next, the inlet ($P_{pA}$ = 2.5 MPa) and outlet ($P_{pB}$ = 1.5 MPa) pressures were applied to provide a pressure differential across the sample, Figure 5.2a. The large difference in confining and pore fluid pressures prevents fluid from flowing around the outside of the sample. Pore pressure oscillations were applied via servo control by feeding a sinusoidal command signal to the inlet pressure intensifier $P_{pA}$. $P_{pA}$ stress oscillations ranged in amplitude from 0.2 to 1 MPa at 1 Hz while holding $P_{pB}$ constant, Figure 5.2a. A table of experiment numbers and corresponding gouge layer weights are listed in Table 5.1.

| **Experiment** | **Gouge Weight (g)** |
|---|---|
| p5729 | 0 |
| p5823 | $0.05 \pm 0.01$ |
| p5817 | $0.09 \pm 0.01$ |
| p5790 | $0.21 \pm 0.01$ |
| p5816 | $0.37 \pm 0.01$ |
| p5789 | $1.06 \pm 0.01$ |

**Table 5.1.** List of experiments with respective gouge weights used in this study.

### 5.3.1 Permeability Measurements

Independent measurements of volumetric inflow ($Q_A$) and outflow ($Q_B$) rates are made using DCDTs ($\pm$/0.1 µm resolution), attached to the pistons of the pressure intensifiers. The flow rate measurements are made throughout the experiments and permeability is calculated under the following conditions: (1) Darcian steady-state flow using Equation 5.1 and (2) oscillatory upstream flow using Equation 5.2. Darcy's law is used to calculate "steady-state" permeability $k$:

$$k = \frac{\mu L\ Q}{A \Delta P_P} \tag{5.1}$$

where $Q = \frac{1}{2}(Q_A + Q_B)$ is the average flow rate, $\mu$ is the fluid viscosity ($10^{-3}$ Pa·s) at 20° C, $L$ is the length of the flow path along the fracture plane (50 mm) and $A$ is the cross-sectional area perpendicular to the flow path (45 mm × 26 mm), which includes both the fracture and granite wall rock (surrounding rock matrix permeability is several orders of magnitude smaller and considered negligible in this analysis). When inflow and outflow rates are within 5 % ($Q_A - Q_B \leq 5\%$), we assume steady-state flow conditions and all data points outside this range are excluded from our analysis.

The flow-analysis technique as described in [112] is used to calculate the "dynamic" permeability, $\hat{k}$, during pore pressure oscillations:

$$\hat{\delta}_Q = \left| \frac{Q_A(t)}{P_A(t)} \right| = \frac{1}{2} \left| \frac{(1-i)\sqrt{\hat{\eta}\hat{\xi}} \sinh\left[(1+i)\sqrt{\hat{\xi}/\hat{\eta}}\right]}{\cosh\left[(1+i)\sqrt{\hat{\xi}/\hat{\eta}}\right]} \right|, \tag{5.2}$$

where $\hat{\eta} = (AT\hat{k}/\pi\mu L)$ and $\hat{\xi} = AL\hat{s}$. Here, $T$, $\hat{k}$, and $\hat{s}$ are the oscillation period (1 s), dynamic permeability, and hydraulic storage, respectively. Dynamic permeability, $\hat{k}$, and hydraulic storage, $\hat{s}$, are calculated from a least-squares minimization between the experimentally measured hydraulic parameter $\hat{\delta}_{Q\text{exp}}$ and the analytically calculated

$\hat{\delta}_Q(\hat{k}, \hat{s})$:

$$(\hat{\mathbf{k}}, \hat{\mathbf{s}})_{\text{opt}} = \underset{\hat{\mathbf{k}},\hat{\mathbf{s}}}{\text{argmin}} \sqrt{\left|\hat{\delta}^2_{V exp} - \hat{\delta}^2_Q(\hat{\mathbf{k}}, \hat{\mathbf{s}})\right|}. \tag{5.3}$$

In this analysis, only the imposed upstream pore pressure and the fluid flux are used to determine the dynamic permeability.

## 5.4 Active Source Ultrasonic Measurements

Active source ultrasonic data are continuously recorded throughout the pore pressure oscillations. The p-polarized transmitting PZTs are successively excited with 96 V half-sine pulses every 0.2 ms. Using the pairs of PZTs along the center column of the array allows us to capture the spatial variability of the fracture's elastodynamic properties (i.e., wave speed and amplitude). The ultrasonic data are processed as previously documented [67, 92, 125, 126], where all waveforms are cross-correlated with a reference waveform (before set of oscillations) over a pre-selected window encompassing the p-wave arrival to determine time delay and RMS amplitude.

## 5.5 Results

Our data include measurements of bulk deformation, fracture permeability, time delay ($\tau$), and RMS amplitude. The transducer array provides information on the spatial variability of fracture stiffness properties modified by grain migration and their evolution during dynamic stressing. This is combined with fluid flow measurements to develop a detailed understanding of fracture poromechanics.

### 5.5.1 Hydraulic and Nonlinear Elastodynamic Responses

Rocks exhibit nonlinear stress-strain behavior due to their constituent minerals and matrix structure, especially from microcracks and compliant grain boundaries [41, 93]. The nonlinear elastodynamic response of fractured rock also includes the contribution of contact acoustic nonlinearity (CAN) at fracture interfaces. Figure 5.2b shows the characteristic responses to pore fluid pressurization. There is a transient softening, indicated by the relative change in time delay $\Delta\tau/\tau_0$ (or ${R_0}^\tau$) and the modulation of baseline time delay ${R_1}^\tau$ followed by a slow recovery. This is also seen in the RMS Amplitude response. Stress- (or strain-) induced changes in wave speed and amplitude are manifestations of a rock's nonlinear elastic response; if this were a linear elastic material, the wave speed/amplitude would be effectively stress invariant. We measure the nonlinear elastodynamic response as it is rich with information about fracture stiffness, inter-grain contacts, and micro-structure [41,84,85], all of which influence fluid flow. That is to say, acoustic wave propagation and fluid flow characteristics under stress are highly influenced by porosity/fracture apertures. While the connection between elastodynamic and hydraulic properties of fractured rock under static stress is relatively established [84,86] there are only a handful of studies on the coupled elastodynamic-hydraulic response under dynamic stressing [105, 125, 126]. It is essential to study not only "bare" fractures [68, 125], but also fractures filled with grains (from wear processes) or proppant (used in industrial hydraulic stimulation) under dynamic stress conditions. Here, we seek to illuminate the role of granular in-fill on static and dynamic elastic and hydraulic properties of fractures under dynamic stressing. We characterize the nonlinear elastic response with: (1) relative change in time delay, ${R_0}^\tau$ (2) the time delay amplitude modulation ${R_1}^\tau$. Both $R_0$ and $R_1$ are extracted using a projection procedure following [92]. ${R_0}^A$ and ${R_1}^A$ are also calculated from the RMS amplitude of the transmitted waves. In addition to the elastodynamic measures, we quantify the relative stress-induced change

in permeability $\Delta k/k_0$ and the dynamic permeability $\hat{k}$, during the oscillations.

### 5.5.2 Dynamic Stress-induced Changes

Here we report the relation between permeability (steady-state and dynamic) and nonlinear elastic measures and pore pressure oscillations. All experiments were conducted at the same effective normal stress ($\sigma_{\text{eff}}$) of 10 MPa and the pore pressure oscillations were conducted at the same frequency of 1 Hz.

We find that larger pore pressure ($P_{pA}$) oscillation amplitudes produce greater permeability enhancement, $\Delta k/k_0$, see Figure 5.3a (and and Figure 5.3a as well). This is similarly observed in experimental work from [20, 30, 105, 125, 126]. Repeated sequences (denoted by marker color and shape) do not systematically change the observed trend permeability enhancement, but can a minor reduction. Interestingly, the permeability enhancement for the fracture surface with no gouge does not systematically correspond with oscillation amplitude a modest increases in gouge produces greater permeability enhancement. This increase is maximum for 0.21 g of gouge and decreases for the sample with 0.37 g. There is no systematic relationship between oscillation amplitude and relative permeability changes for the sample with 1.06 g of gouge. The dynamic permeability, $\hat{k}$, also monotonically increases with pore pressure amplitude, Figure 5.3b, for all gouge layers. The nominal values of $\hat{k}$ at the lowest oscillation amplitude, 0.2 MPa, are consistent with the nominal steady-state permeabilities and with previous work [30]. The trend of enhancement followed by reduction observed in $\Delta k/k_0$ is also present in the measure of dynamic permeability $\hat{k}$, where the maximum dynamic permeability increase occurs in the 0.21 g gouge sample.

Two measures of elastic nonlinearity, $R_0$ (relative change) and $R_1$ (average modulation during oscillation) for time delay and RMS amplitude are shown in Figure 5.3c-d for the middle column of transmitter-receiver pairs. Though there is some scatter in

the top PZT pair (yellow dots), the overall observation is some spatial variability in the time delay ${R_0}^{\tau}$, Figure 5.3c. For most of the gouge layers, the relative change in time delay decreases with pore pressure oscillation. This is consistent with the findings by [68, 105, 125, 126]. Figure 5.3d shows the relative change in RMS p-wave amplitude (${R_0}^{A}$ for the middle column of transmitter-receiver pairs of PZTs for all gouge layers. Again, there is spatial variability across the different receivers and generally decreases with pore pressure oscillation amplitude. The most distinct change in RMS amplitude is seen in the gouge layer with 0.21 g of quartz powder of Figure 5.2d.

### 5.5.3 Linking Static and Dynamic Poromechanical Measures

The different measurements of permeability and elastodynamic properties in the previous section show consistent trends across different experiments with varying amounts of gouge. These results are summarized in Figure 5.4. Figure 5.4a shows the steady-state permeability before pore pressure oscillations commenced, averaged over 1 s, for each gouge layer. The permeability is constant within 1 standard deviation with increasing gouge weight. Though, this may not hold for much thicker gouge layers at this particular stress (10 MPa). Interestingly, all other measured parameters are not constant across gouge weights. Figure 5.4b and c, the slopes of $\Delta k/k_0$ ($\varphi$) and $\hat{k}$ ($\hat{\varphi}$) with respect to oscillation amplitude, change with the addition of gouge at the fracture interface. Both $\varphi$ and $\hat{\varphi}$ increase and reach a maximum at 0.21 g after which they rapidly decrease.

The measured elasto-dynamic properties are shown in Figures 5.4. The amplitude of transmitted wave $A$ in Figure 5.4d is measured before oscillations commence and increases with gouge weight to 0.21 g and then decreases for all transmitter-receiver pairs although the top transducer's response is distinct from the other two. The lower transmission is most likely due to less amount of gouge present in the wave path of this PZT pair, again indicating the spatial variability of the fracture characteristics and

its strong influence on the elastodynamic response. Figure 5.4e shows the slope (least-squares fit) of ${R_0}^A$ as a function of gouge weight and shows the largest transient change (more negative) at 0.09-0.21 g of gouge at the fracture interface. Though, the slope of RMS amplitude modulation ${R_1}^A$ is less systematic with gouge content, Figure 5.4f. We observe some similar trends in the time delay data. Figure 5.4g shows that normalized time delay $||\tau||$ generally decreases with amount of gouge, equivalent to an increase in the p-wave velocity. Much like the slope of ${R_0}^A$, ${R_0}^\tau$ shows the largest transient change (degree of nonlinearity) with oscillation amplitude between 0.09-0.21 g of gouge, Figure 5.4. The slope of $\tau$ amplitude modulation ${R_1}^\tau$ is relatively large (magnitude) and then fluctuates around 0 for all receivers for increased amount of gouge.

In summary, the measurements of hydraulic ($k$) and elastic ($A_{\text{RMS}}$ and $\tau$) represent steady-state or static properties of a planar fracture with varying amounts of gouge. These observations are not necessarily correlated with the distinct measurements during dynamic stressing. Additionally, we consistently observe the greatest permeability enhancement ($\varphi$ and $\hat{\varphi}$) and nonlinear elastic response (${R_0}^A$ and ${R_0}^\tau$ slopes) at the same range of gouge weight.

## 5.6 Discussion

Our results show a strong relationship between the hydraulic and elastodynamic responses to: (1) dynamic stressing and (2) amount of quartz powder (gouge) in fracture interface. We seek to quantify the role of gouge in modifying the poromechanical response of planar fractures to dynamic stressing. Between experiments and after roughening the planar fracture surface, we used a Keyence VKK-X3100 3D Surface Profiler to measure the surface topographies of both fracture halves. By subtracting these two complementing surface profiles, we create a topography of the fracture aperture, or gap height distribution ($h$gap), shown in Figure 5.5a. This shows that under zero applied

stress, the fracture interface has few contacts and is mostly open. This is illustrated with the probability density distribution in Figure 5.5b, where a significant portion of the randomly rough fracture gap height is between ∼400-600 µm. Next, we estimate the fine quartz powder (Min-U-Sil 40) mean grain size from the work of [89] in order to estimate the gouge layer thicknesses, under zero stress. Assuming a uniform distribution, we estimate the layer thickness with the following: $t = \frac{\rho A}{w}$, where $\rho$ is the quartz powder density of 0.921 g/cm$^3$, $A$ is the nominal surface area of the fracture interface ($1.8 \cdot 10^{-3}$ m$^2$), and $w$ is the weight of gouge. The layer thickness estimations are shown in Figure 5.5c. We believe this estimation is reasonable, as the measured layer thickness with 1.06 g of gouge is $\sim$ 750 µm, compared to the $\sim$ 700 µm estimate. The significant observation is the correspondence between gouge layer thickness and fracture aperture $h_{\text{gap}}$, Figure 5.5b-c, and their effect on the elasto-dynamic observations, which we enumerate below.

We posit three distinct regimes that are responsible for the hydraulic and elastodynamic responses and are dominated by: (1) fracture roughness, (2) particle mobilization through fluid pathways, and (3) thick gouge layers/packs. Refer to Supplemental Figure C.1 for a schematic explanation of these regimes. Another important consideration is the imposed stress level. Though we do not investigate this parameter in this study, [68,125] report reduction in the elastodynamic response and permeability enhancement with increasing stress level. In the first regime, the relative change in permeability, $\Delta k/k_0$, is invariant with oscillation amplitudes, and the dynamic permeability $\hat{k}$ enhances some with oscillation amplitude. The magnitude of nonlinear responses ($R_0{}^{\tau}$ and $R_0{}^{A}$) in this regime are small and comparable to the bare fractures used these studies [68, 125]. Thus, we attribute these responses to bare fracture surfaces and gouge layers $\ll$ than the fracture aperture. In regime 2, acoustic transmission ($A$) is maximal, suggesting that gouge layer thicknesses (less than and approaching the fracture aperture) suffi-

ciently fill void spaces. Also, hydraulic and elastodynamic (especially $\varphi$, ${R_0}^A$, ${R_0}^\tau$) responses are greatest in the second regime. We attribute the hydraulic response to fluid flow mobilizing the quartz particulates and liberating them from narrow/jammed regions along/through existing flow pathways. This clogging/unclogging of constituent grains through a fracture is also the dominating mechanism in laboratory work under similar conditions [20, 30, 132] and laboratory experiments involving in-situ fracture and shear [126]. Additionally, the large nonlinear elastic response likely manifests from the modulation of the integrative contribution of inter-grain contacts [37] and contacting fracture asperities, thus leading to large changes in stiffness [68, 125]. Nonetheless, this strong correlation between fracture interface stiffness and hydraulic properties is consistent with other studies [68, 83, 105, 125, 126]. We distinguish the third regime as gouge layer thicknesses greater than or equal to the fracture aperture. We propose that this regime is characterized by a reduction in acoustic transmission ($A$ in Figure 5.3d) and time delay ($||\tau||$ in Figure 5.3g. Furthermore, the relative change in permeabilities $\varphi$ and $\hat{\varphi}$ are smaller than previous regimes, or there is no enhancement. Though the static permeability $k$ (Figure 5.3a) is nearly invariant with gouge thickness/weight, the pore pressure oscillations are sufficiently large enough in magnitude to produce changes in gouge porosity, leading to the observed small changes permeability enhancement. The elastodynamic response, relative changes in RMS amplitude and time delay, notably ${R_0}^A$ and ${R_0}^\tau$, are also greatly reduced in this regime, indicating small changes in fracture (including gouge layer) stiffness. The spatial variability in this regime, and others, highlights the sensitivity to the fracture (and filled) interface and its geometric/compositional heterogeneities. We argue that this regime may be considered to be an effective medium in which the elastic [58] and nonlinear elastic [37] properties as well as hydraulic properties are modulated by the gouge layer, rather than the fracture (contacting asperities). Furthermore, this qualitatively agrees with the findings in [126], in which a

tensile fracture was progressively sheared in stages and then subject to normal stress and pore pressure oscillations. The nonlinear elastic response and permeability enhancement were enhanced with some shear (gouge generation), compared to immediately after the formation of the tensile fracture. Then, subsequent shear reduced the nonlinear elastic response and permeability enhancement. This suggests that the development of gouge (fracture in-fill) can be a controlling parameter for the elastodynamic and fluid flow responses to stressing in both natural and planar fractures.

In summary, we discriminate our hydraulic and elastic observations into three distinct regimes. We posit these regimes are characterized by (1) changes in fracture stiffness, (2) fracture stiffness and flow augmented by mobilized grains, and (3) development of an effective medium in which the fracture asperities have little to no influence. Overall, these hypotheses are based on optical profilometry of the fracture interface and estimation of layer thickness from gouge weight. It is worth noting that this is based on a set of experiments utilizing a narrow grain size distribution [89] with the mean grain size of about 50 µm (approximately 10 grain diameters fill the mean aperture). Despite these limitations, we report a compelling interplay between fracture roughness and grain size and the hydraulic and elastic properties they manifest. This work could be complemented by other studies that take into consideration: grain size and shape [37], thicker gouge layers, the ratio of grain diameter to fracture aperture, and naturally rough fractures, to name a few.

## 5.7 Conclusion

We seek to elucidate and decouple the role of fracture roughness and grain size on fluid flow and elastic properties. We perform a series of laboratory experiments with a roughened planar fracture specimen with varying amounts of gouge material to consider the influence of granular in-fill (wear material) on the elastodynamic response and perme-

ability enhancement under pore pressure oscillations. Each experiment was performed under the same stress and fluid flow conditions and continuous cross-fault ultrasonic monitoring and fluid flux measurements that allow for the characterization of the elastic and hydraulic response to dynamic stressing. The dynamic stressing protocol was designed to assess repeatability and the effect of pore pressure oscillation amplitude (larger dynamic strain). Our results show qualitative similarity to field observations of permeability enhancement and changes in transmitted wave properties [15, 26, 48].

In addition to experiments, we characterize the fracture topography, using optical profilometry, and use previous measurements of grain size [89] to interpret our observations of dynamic stress-induced changes in the poro-elastic properties with regard to fracture in-fill. We separate these properties into three regimes with different dominating mechanisms. These regimes are dominated by (1) fracture stiffness changes – modest permeability enhancement and elastodynamic changes, (2) fracture stiffness and flow augmented by grains – pore clogging/unclogging and large elastodynamic changes resulting from fracture in-fill, and (3) development of an effective medium – most fracture asperities are not in contact and have little to no influence on fluid flow or elastic properties. Though this study is focused on just the effect of layer thickness for one grain size distribution and one fracture roughness, we observe a interesting interplay between the two and their respective hydraulic and elastic response. Furthermore, we draw similarities between results and those from previous experimental work [126] which progressively sheared a natural, tensile fracture to develop wear material.

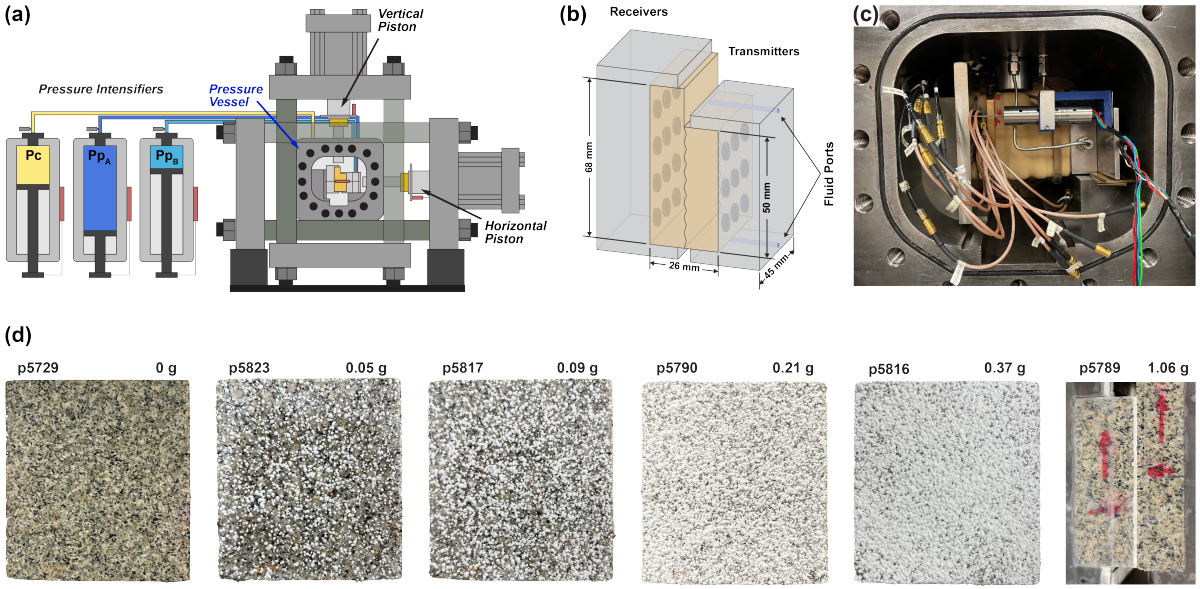



**Figure 5.1.** (a) Biaxial loading apparatus with pressure vessel in Penn State's Rock Mechanics Laboratory. (b) Loading blocks with an embedded array of transmitters and receiver PZTs allow for active source ultrasonic monitoring and fluid inlet/outlet ports allow for fracture-parallel flow. (c) Photo of sample sealed with a latex membrane inside of the pressure vessel. (d) Saw-cut Westerly granite specimen with gouge sprinkled onto #80 grit roughened surface ranging from 0 to 1.06 g.

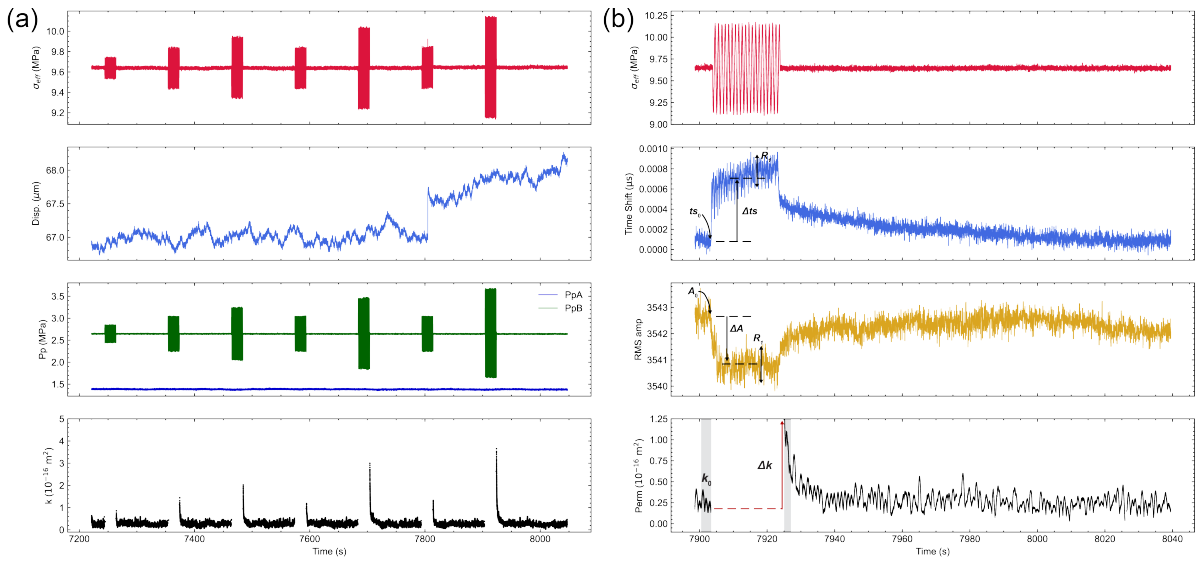



**Figure 5.2.** (a) Overview of the experiment showing pore pressure oscillations in effective normal stress at different amplitudes. (b) Inset of 1 MPa amplitude pore pressure oscillation showing time shift, RMS amplitude, and permeability, respectively arrows and labels indicate how relative changes are calculated.

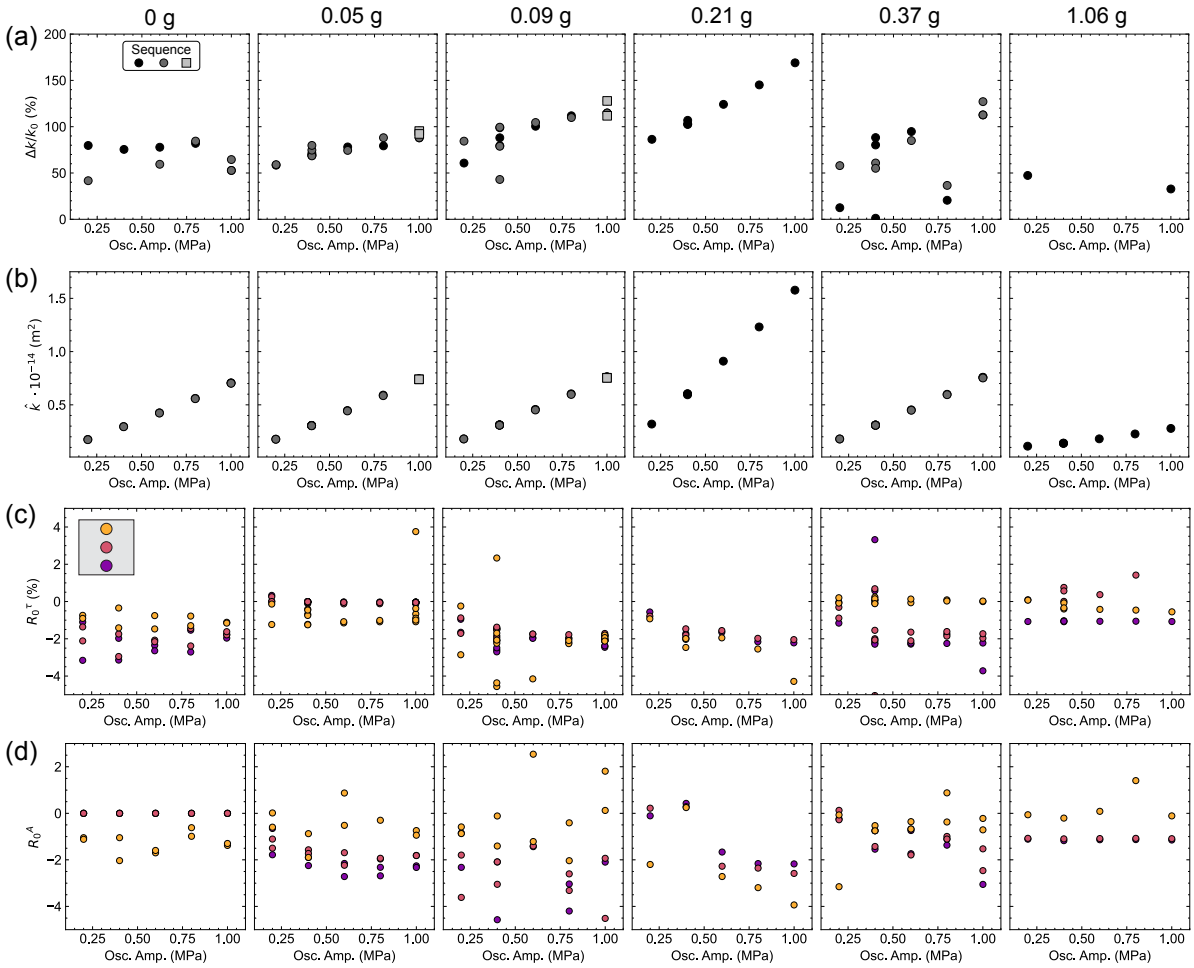



**Figure 5.3.** (a) Steady-state permeability $k$, (b) dynamic permeability $\hat{k}$, (c) relative time shift change ${R_0}^{\tau}$, and (d) relative RMS amplitude change ${R_0}^{A}$ as a function of pore pressure oscillation amplitude for a range of gouge weights at fracture interfaces, respectively.

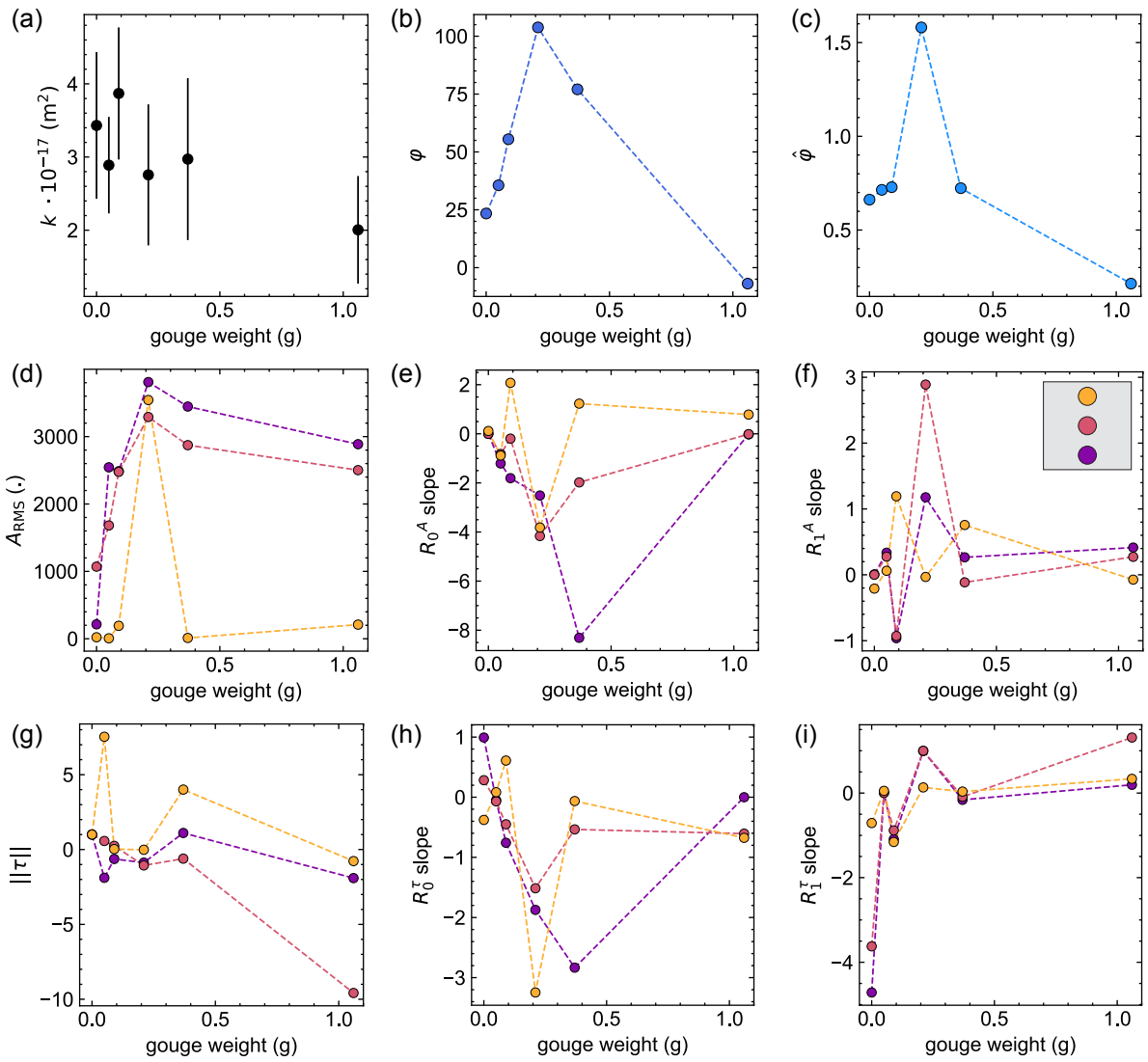



**Figure 5.4.** (a) Steady-state permeability remains nearly with increasing gouge weight. (b) Slope of permeability change $\varphi$ and (c) dynamic permeability change $\hat{\varphi}$ with oscillation amplitude as a function of gouge weight. (d) RMS amplitude $A_{\mathrm{RMS}}$ for each transmitter-receiver pair for increasing gouge weight. (e) Slope of relative change in RMS amplitude ${R_0}^A$ and (f) variation in RMS amplitude during oscillation as function of gouge weight. (g) Normalized time delay $||\tau||$ for each transmitter-receiver pair. (h) Slope of relative change in time delay ${R_0}^\tau$ (i) and variation in time delay amplitude ${R_1}^\tau$ during oscillation as function of gouge weight.

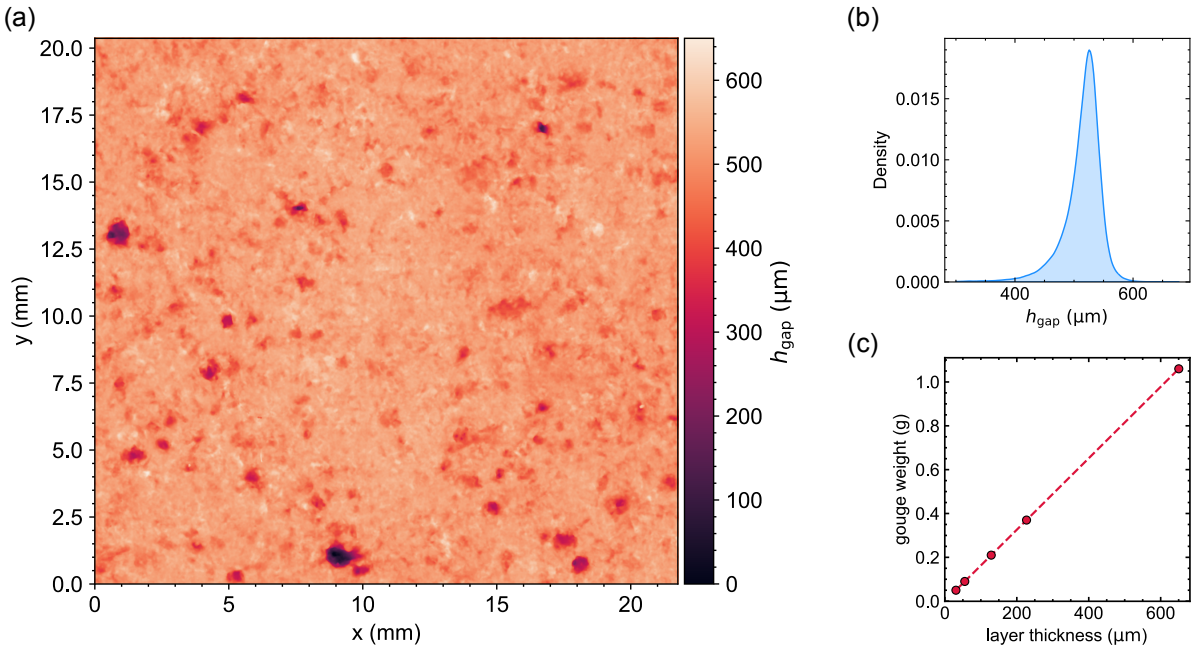



**Figure 5.5.** (a) Gap height distribution from both sides of the randomly rough # 80 grit planar fracture surfaces under 0 stress. (b) Probability density distribution of the fracture gap height (aperture) in (a). (c) Gouge weight as a function of estimated layer thickness.

# Chapter 6

## Conclusions and Future Work

## 6.1 Research Summary

This dissertation addresses fundamental questions surrounding the connection between fracture specific stiffness and fluid transport under a range of loading conditions and dynamic stressing. Moreover, I do so by performing complex experiments under triaxial stresses and use simultaneous continuous active-source ultrasonic monitoring and fluid flux measurements to measure the static and dynamic elastic and hydraulic properties of fractures. These unique experiments are also complemented by post-surface and topography characterization using pressure registering films and profilometry. In the context of dynamic stresses manifesting changes in subsurface fluid flow and elasticity, this dissertations provides insights into the underlying mechanisms observed at much larger scales.

Chapter 2 introduces dynamic acoustoelastic testing (DAET) to probe the elastodynamic and hydraulic properties of fractured rock. This also introduces the complex true-triaxial experiments used throughout this dissertation that simulate subsurface stress and flow conditions. Monitoring in-situ fractures with active source ultrasonic transmission and fluid permeability during dynamic stressing driven by both normal stresses and fluid pressures reveals the complex relation between elastodynamic and hydraulic properties. In response to oscillations of effective normal stress, fractured Westerly

granite samples exhibit characteristic transient softening, acoustic velocity fluctuations, and slow recovery, informing us about microstructure and contact mechanics. As found in [105], large amplitude and high frequency oscillations generally increase permeability, with pore pressure oscillations producing the largest enhancement of permeability. Furthermore, we document spatial variability in elastodynamic properties across the fractured samples, revealing the effect of changes in fracture properties (such as contact asperity stiffness, aperture). We find that shearing generally decreases the relative velocity change ($\Delta c/c_0$) for both normal stress and pore pressure oscillations. We hypothesize that the fracture dilation and compaction (heterogeneous aperture change) dominate during applied normal stress oscillations and clogging/unclogging dominates during pore pressure oscillations and these phenomena are related to the underlying mechanisms responsible for the observed nonlinearity and permeability changes.

Chapter 3 explores the role of the real area of contact and aperture closure (deformation) on fracture stiffness and fluid transport. Conditions are representative of fractures at various depths. Simultaneous measurements of fluid flow and active-source ultrasonic transmission show how these mechanisms are coupled – potentially linking permeabilities with elastodynamic characteristics. Additionally, we quantify the heterogeneity of the fracture contacts at discrete stresses in order to better interpret our observations from multiple transducer pairs probing different parts of the fracture. We add to the work of [67, 105, 126] by documenting a reduction in pore pressure oscillation-induced permeability enhancement with increasing normal stress on the fracture and related fracture closure. Similar trends are observed for the nonlinearity parameters $\alpha$ and $\beta$. We investigate the spatial heterogeneity of nonlinearity parameters with regard to actual estimations of fracture contacts and voids. To that end, pressure sensitive film images are related to ultrasonic measurements; a smaller initial contact area ($S_0$) is associated with higher nonlinearity $\beta$ and a larger $S_0$ with a smaller $\beta$. Finally, we documented the rate

of recovery from post-oscillation state of permeability and wave velocity. These recovery rates are orders of magnitude smaller than those reported in previous studies [105, 126], where gouge present at the fracture interface dominated permeability changes.

Chapter 4 leverages high resolution surface profilometry from a tensile fracture as an input for multiphysics modeling of fracture deformation and fluid flow, constrained by experimental measurements. Rather than generating a synthetic rough surface via fractal geometry, Hurst exponent, or percolation, we scanned a tensile fractured Westerly granite specimen, used in experiments, with a high resolution profilometer to reconstruct a composite aperture digitally. This composite aperture is deformed using an elastic contact model where deformation is influenced by neighboring regions, as opposed to an ensemble, statistical, "asperity-based" approach. Fluid flow is then solved across the deformed fracture aperture based on a hydraulic cubic law. We find that our numerical simulation does not reproduce the fluid flow rate as measured in experiments, but the relative change in flow as a function of a applied stress matches very well. Additionally, we posit that the hysteretic relationship observed in experiment is likely dominated by minute evolution in fracture surface alignment. A parametric study in which bulk properties, elastic modulus and Poisson ratio, were modulated for a range of 5 decades of applied stresses demonstrates that fluid flow is linked to the compliance of the fracture interface. Since this range of data collapse on each other, we consider this to be a proxy for a range of rock types at different stress states or subsurface depths. Finally, we characterize the fractal geometric roughness, show that it remains nearly invariant across the large range of applied stresses and relate it to fracture permeability, with respect to elastic and applied stresses.

Chapter 5 focuses on decoupling two previously investigated parameters, fracture aperture and granular in-fill, from their poro-elastic responses. We perform a series of laboratory experiments with a roughened planar fracture specimen with varying amounts

of gouge material. Each experiment was performed under the same stress and fluid flow conditions and continuous cross-fault ultrasonic monitoring and fluid flux measurements allow for the characterization of the elastic and hydraulic response to dynamic stressing. The dynamic stressing protocol was designed to assess repeatability and the effect of pore pressure oscillation amplitude (larger dynamic strain). Our results show qualitative similarity to field observations of permeability enhancement and changes in transmitted wave properties [15, 26, 48]. Optical profilometry and measurements of grain size [89] provided valuable insights into our observations of dynamic stress-induced changes in the poro-elastic properties. We separate these properties into three regimes with different dominating mechanisms. These regimes are dominated by (1) fracture stiffness changes – modest permeability enhancement and elastodynamic changes, (2) fracture stiffness and flow augmented by grains – pore clogging/unclogging and large elastodynamic changes resulting from fracture in-fill, and (3) development of an effective medium – most fracture asperities are not in contact and have little to no influence on fluid flow or elastic properties.

Ultimately, this dissertation provides a framework to relate fracture geometry to specific stiffness and permeability. Thus, the results presented here have significant implications for better understanding elastodynamic and hydraulic changes manifest from stain-induced and fluid-induced dynamic perturbations in the field. Additionally, new applications of dense seismic arrays could provide unprecedented field-scale monitoring and insights into scalability of these laboratory and numerical observations.

# Appendix A

## Supplementary Information for Chapter 2

### Introduction

This supporting information contains figures that clarify how permeability is calculated and hydraulic and mechanical properties during shearing phases from experiment p4975. Furthermore, we show how velocity and RMS amplitude evolve with outlet flow rate and normal stress oscillations, and how change in RMS amplitude relates to change in permeability.

Though we did not quantify the fracture interface or roughness, we did document the gouge material generated from fracture and shearing the sample. Figure A.1 illustrates the roughness of the fracture interface also annotates different types of gouge material generated from experiment p4975.

In Figure A.3 we measure the effective permeability, $k$, by calculating the flow rate over a 2 s window. For pore pressure oscillations, we start 10 s after the oscillation to ensure that permeability measurement is not affected by the $P_p$ oscillation and/or by storage effects.

Figures A.4 and A.5 show how the flow rates evolve with various shearing rates in experiment p4975. We attribute the smaller flow rates in the second shearing phase ($\approx 1/2$ that of the first shearing phase) to be in response to the comminuted grains clogging the fracture.

The relationship between these parameters in the beginning, middle, and end of the oscillation are presented in Figure A.6. This figure also includes hysteresis plots that show how the wave velocity vary as a function of stress. Throughout this long oscillation the velocity-flow hysteresis loop generally evolves to a lower velocity and lower flow rate and the loop becomes slightly more closed. We also observe this general decrease in wave velocity as a function of applied stress throughout the history of the oscillation.If the oscillation persists long enough, the wave velocity modulations reach a steady-state. These observations demonstrate the magnitude of changes we are characterizing and also reinforce that the fracture is continuously evolving during the dynamic perturbations; contacts undergo compression and tension resulting in changing flow paths across the fracture.

For elastic waves that travel across fractures the transmitted amplitude provides information on contact stiffness and area. Our data show that changes in RMS amplitude, $\Delta A/A_0$, evolve in a similar manner to changes in p-wave velocity for both types of effective dynamic stressing (see Figure A.7). In the post-fracture case p4975 results show that the change in transmitted p-wave amplitude becomes more negative with increasing normal stress amplitude; this relation is less obvious with pore pressure oscillation amplitude. Furthermore, there is little variation in these results with the order in which the oscillations were conducted. The situation is different for experiments p4966 in that the results are very scattered for normal stress oscillations and more coherent for pore pressure oscillations. The order of oscillation is most pronounced for oscillation amplitudes $> 0.25$ MPa, subsequent sets are less nonlinear. Surprisingly, normal stress oscillations in post-shear 1 of experiment p4966 produce positive changes in RMS amplitude, which contradict our findings with respect to $\Delta c/c_0$. Another interesting observation is that progressive shearing creates conditions that produce less nonlinearity. These differences are likely due to the complexity of fracture roughness and changes in contact stiffness

with shear.

The averaged change in RMS as a function of $\Delta k/k_0$ is plotted in Figure A.8. These plots show a complex relationship between the transmitted energy and fracture hydraulic properties. Normal stress oscillations of 40 Hz frequency consistently produce positive nonlinearity values. This and our observation that nonlinearity decreases with shearing are in fact physical rather than artifacts of data analysis. Pore pressure oscillation results are more scattered but show a similar relationship as normal stress oscillations, but the underlying elasto-hydraulic mechanisms require further experimental investigation.

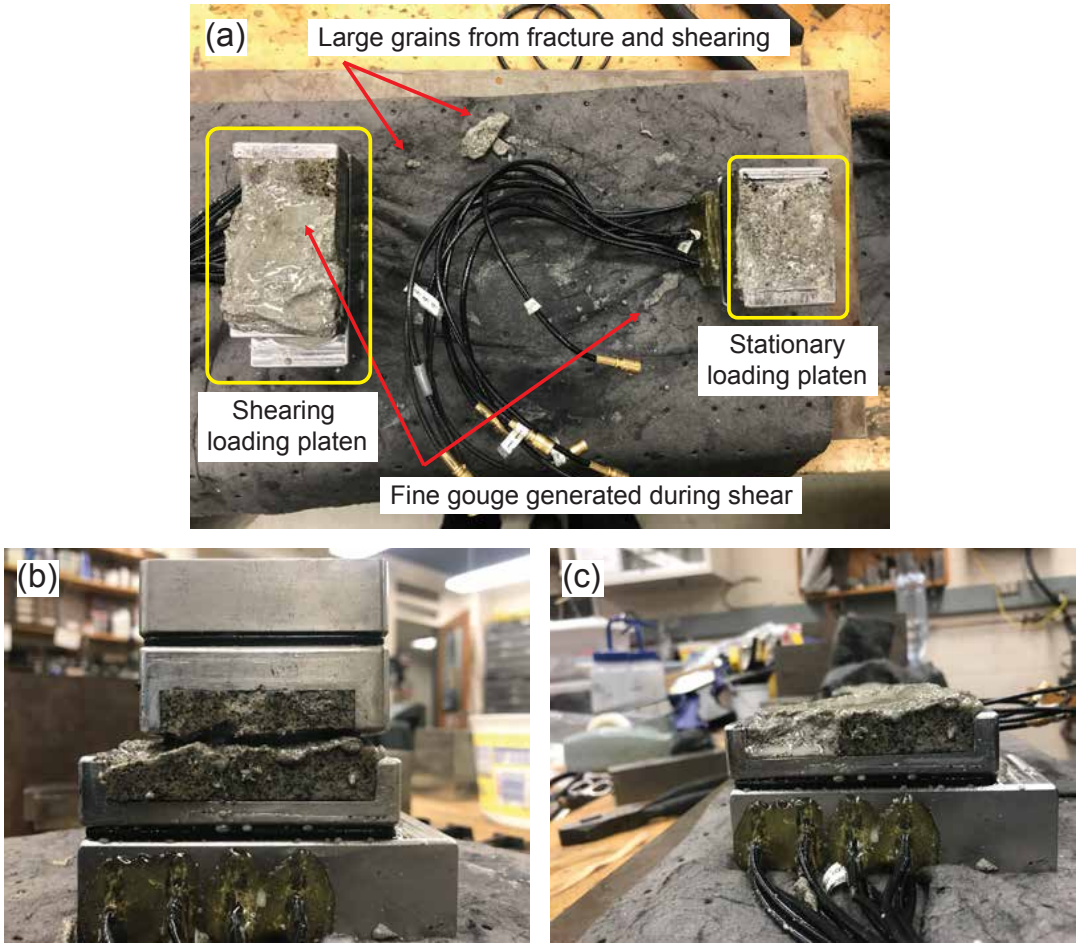



**Figure A.1.** (a) Loading platens containing sample halves sitting on gray absorbent towel. Notice examples of both large grains from fracture and shearing (red arrows at top of image) and fine gouge generated during shear (red arrows at middle of image). During this experiment this material was not collected or quantified. (b) Side view of the post-mortem sample illustrating the roughness of the fracture. (c) Alternate side view of post-mortem sample without the short sideblock further highlighting the rough fracture surface.

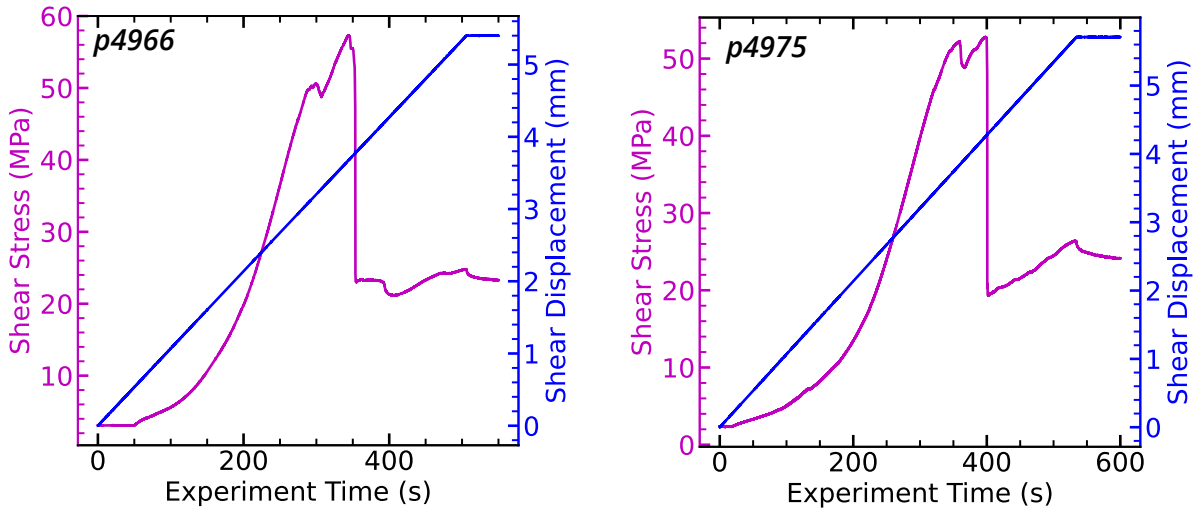



**Figure A.2.** (a) and (b) show the shear stress and displacement during in-situ fracturing in experiments p4966 and p4975, respectively. The amount of slip displacement is approximately 1.5 mm for each experiment.

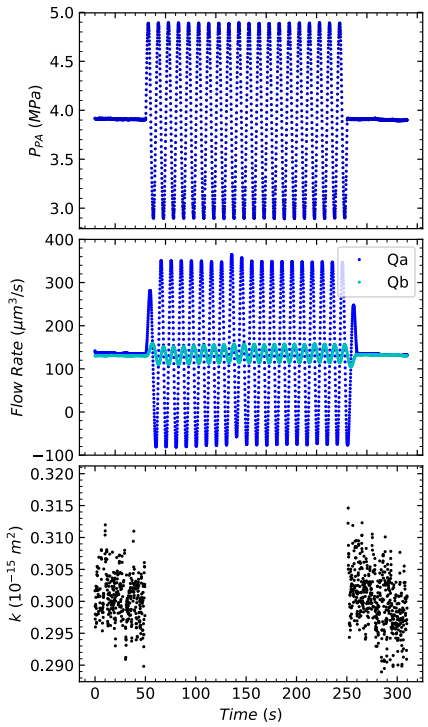



**Figure A.3.** Example of dynamic stressing and the corresponding flow rate measurements for a set of pore pressure oscillations in experiment p4975. Note that the plots (a) and (b) are decimated for clarity. (a) Imposed pore pressure oscillation at inlet and fixed pore pressure at the outlet. Pressure conditions before and after the oscillations are identical. (b) Measured flow rates at the fracture inlet (blue line) and outlet (cyan line). Notice the small time lag ($\leq 2$ s) between the maxima of the inlet and outlet flow rates. (c) Permeability at steady-state and during the pore pressure oscillation. In the calculation of permeability we impose a threshold between the flow rates to ensure steady-state flow ($Q_A - Q_B \leq 5\%$). It is reasonable to assume that even at relatively low frequency oscillations, there is effectively no steady-state flow during the imposed oscillations.

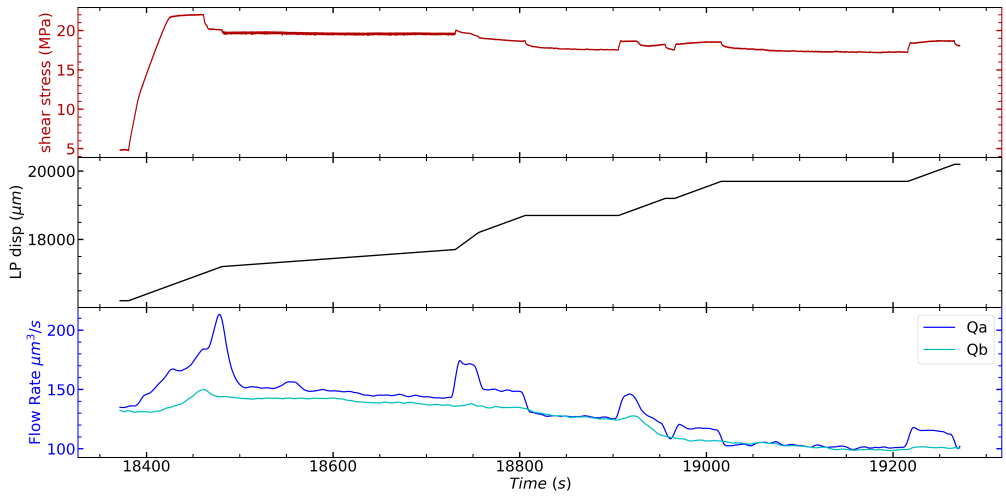



**Figure A.4.** First shear of experiment p4975. There are noticeable spikes in inlet flow rate $Q_A$ in response to shear displacement (LP disp) speed.

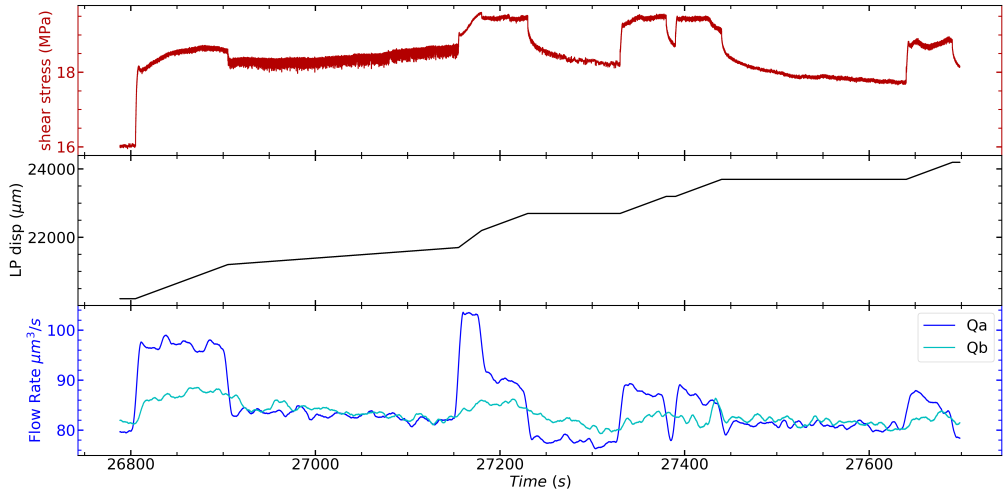



**Figure A.5.** Second shear for experiment p4975. There are spikes in inlet flow rate $Q_A$ and a smaller, delayed increase in outlet flow rate $Q_B$ in response to changing shear displacement (LP disp) speed.

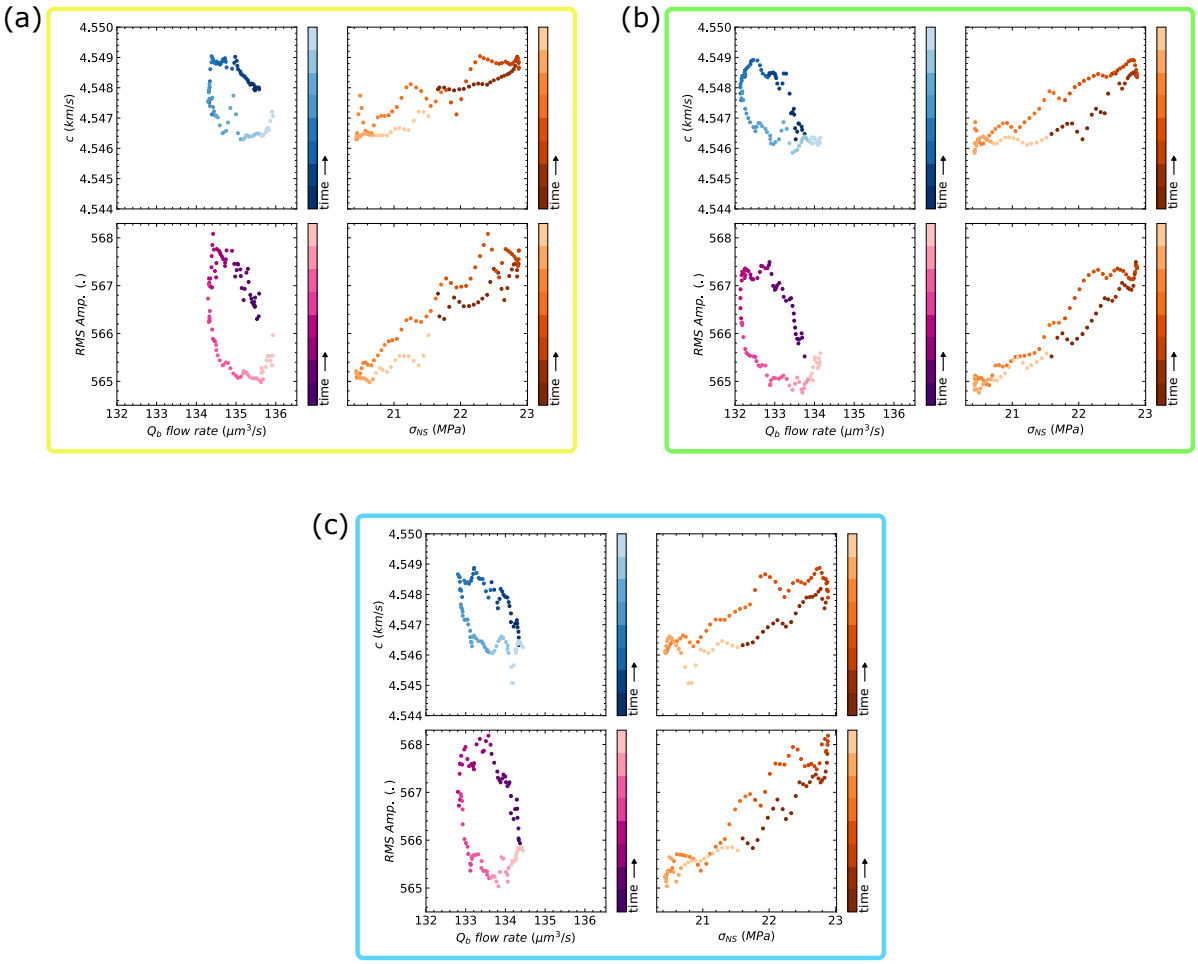



**Figure A.6.** Evolution of the fracture during a 1 MPa, 1 Hz normal stress oscillation during the first cycle (a), middle cycle (b), and last full cycle (c) from Figure 6 in the manuscript. RMS amplitude a velocity are very sensitive to changes in outlet flow rate variations throughout the entire oscillation cycle. At the end of the cycle, there is a small reduction in velocity, the RMS amplitude does not change, and the flow rate lower than the beginning of the cycle.

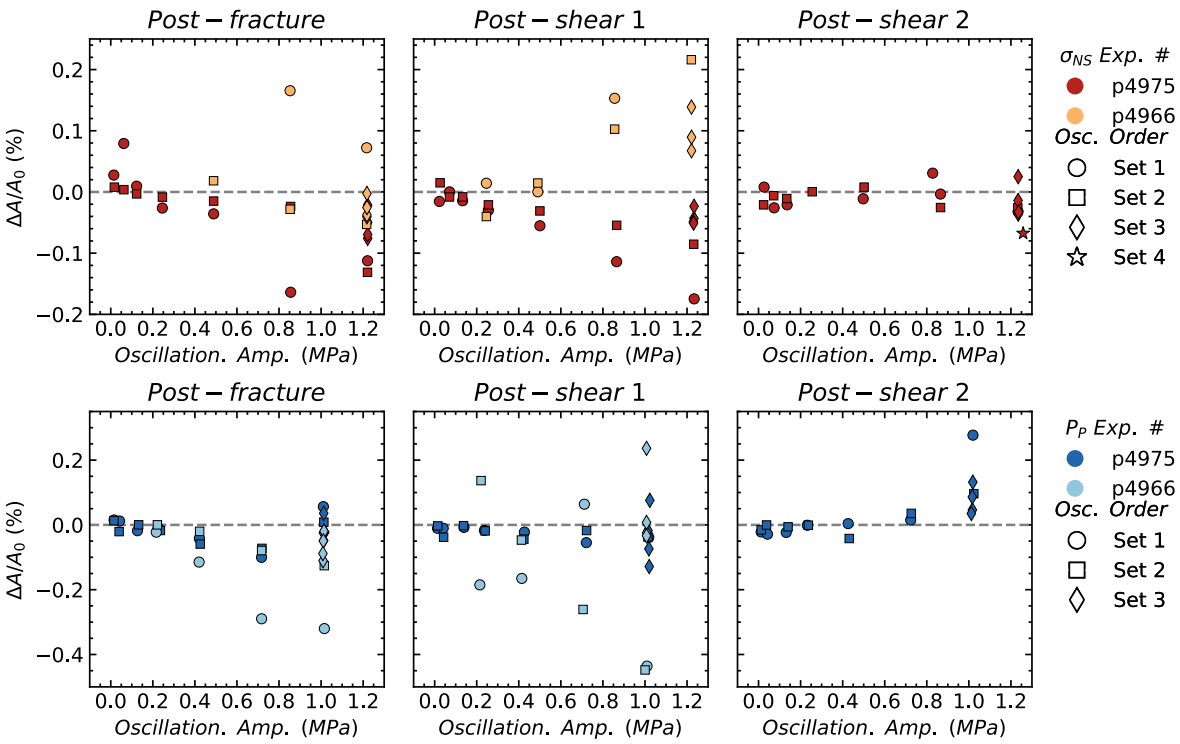



**Figure A.7.** RMS amplitude for direct-path receiver as a function of permeability change for $\sigma_{NS}$ and $P_P$ oscillations. Data point shapes oscillation order. RMS amplitude decreases with oscillation amplitude and show little variation with order for experiment p4975. Order of oscillation is most pronounced for oscillation amplitudes $> 0.25$ MPa, Subsequent oscillation sets are less nonlinear; surprisingly, normal stress oscillations in post-shear 1 in p4966 produce positive changes in RMS amplitude. Furthermore, progressive shearing creates conditions that produce less nonlinearity, likely due to the complexity of fracture aperture and changes in contact stiffness.

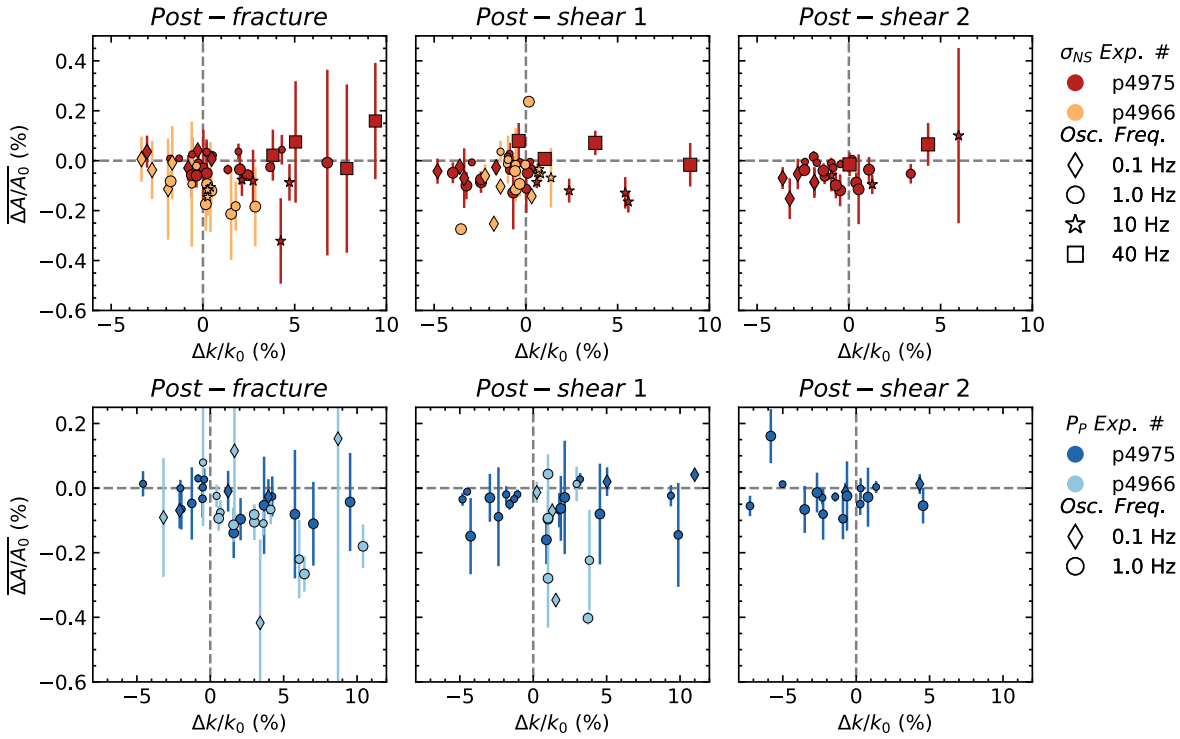



**Figure A.8.** RMS amplitude averaged over all receivers as a function of permeability change for $\sigma_{NS}$ and $P_P$ oscillations. Data point shapes correspond to oscillation frequency and sizes to amplitude. The average RMS amplitude decreases with oscillation amplitude and frequency, except at high frequencies where there is anomalous behavior. Shearing the fracture weakens the relationship with relative permeability change.

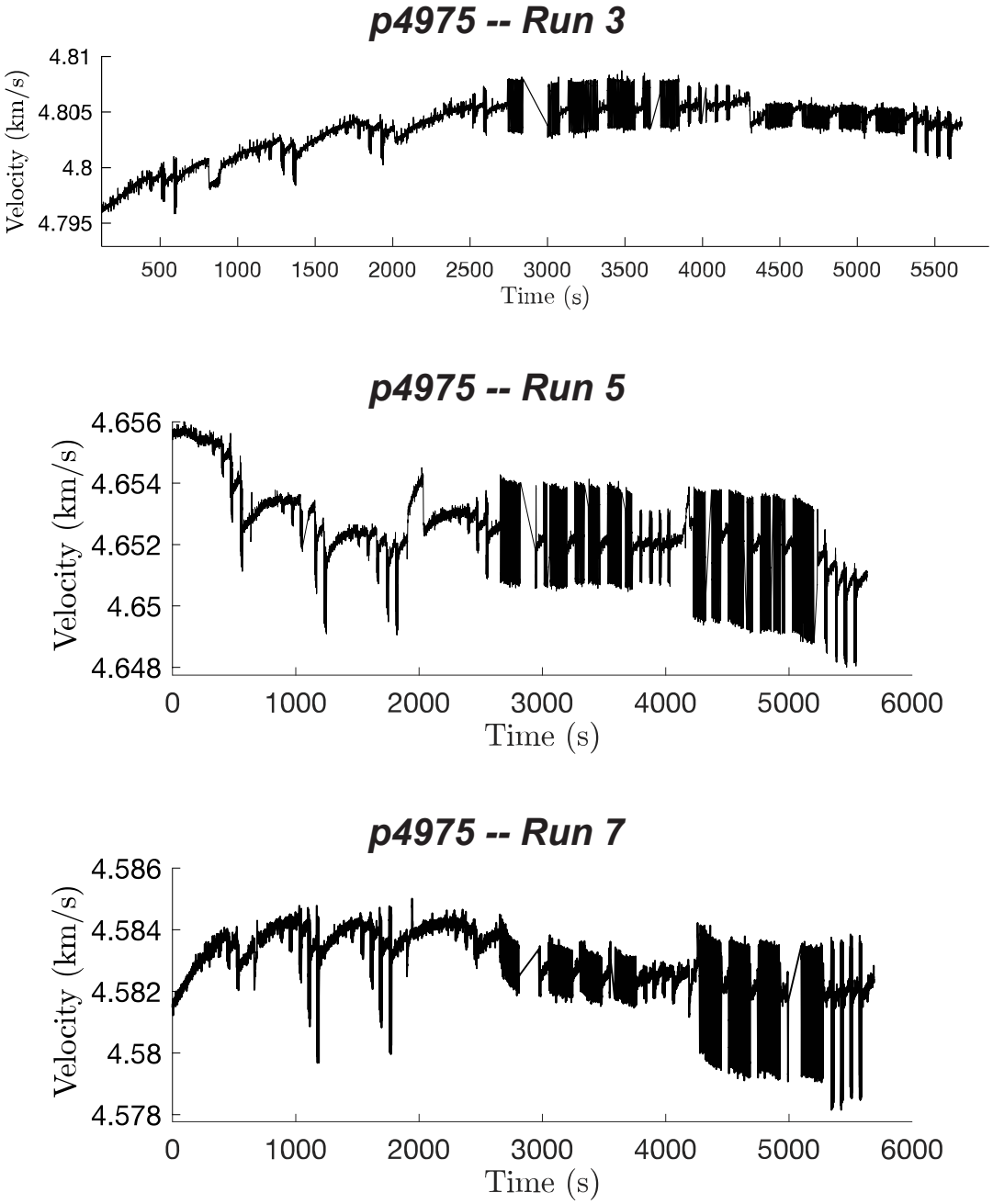



**Figure A.9.** Wave velocity from experiment p4975 during runs 3, 5, and 7. Shearing the fracture reduces the wave velocity for the direct-path transmitter-receiver pair.

# Appendix B

## Supplementary Information for Chapter 3

### Introduction

This supporting information contains figures that highlight the repeatability of our experiments and the effect of loading history on our dynamic stress-induced changes in elasticity and permeability.

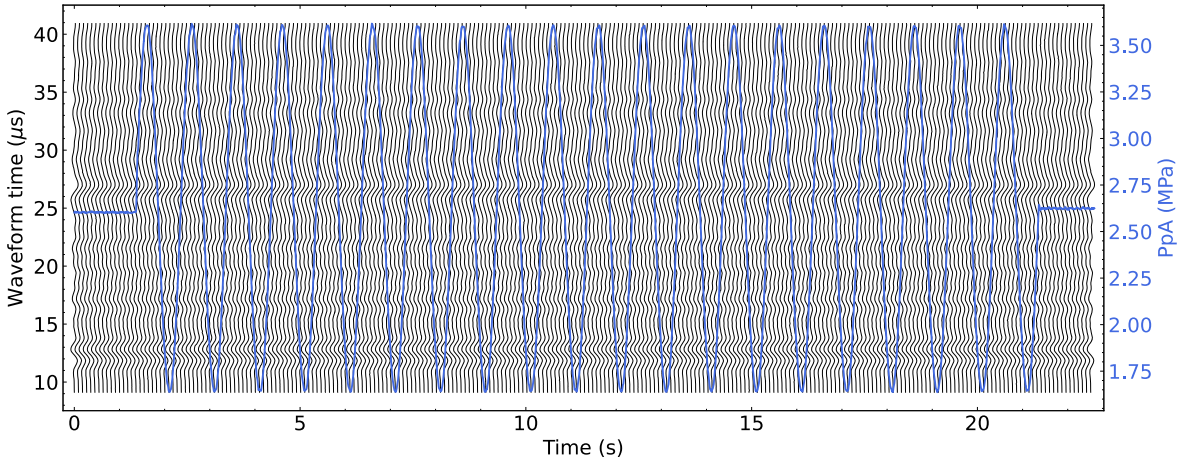



**Figure B.1.** Excerpt from Run 15 of experiment p5483 shows a 1 Hz, 1 MPa pore pressure oscillation (blue) and concurrent raw ultrasonic waveforms (grey). The number of waveforms in the waterfall plot have been decimated for clarity.

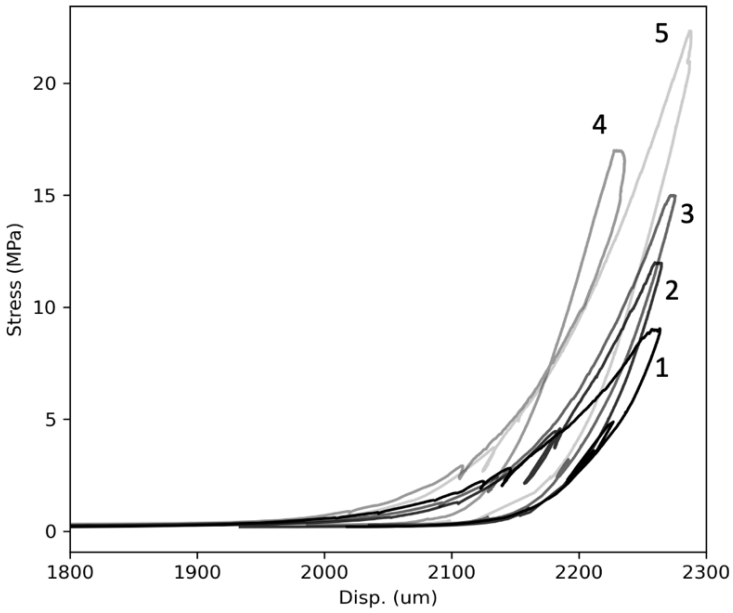



**Figure B.2.** Load/unload curves for 5 experiments using pressure sensitive film to measure fracture contact area. Note the consistency and reproducibility of these data. They all show some hysteresis but the loading/unloading curves are nearly identical even at low stresses.

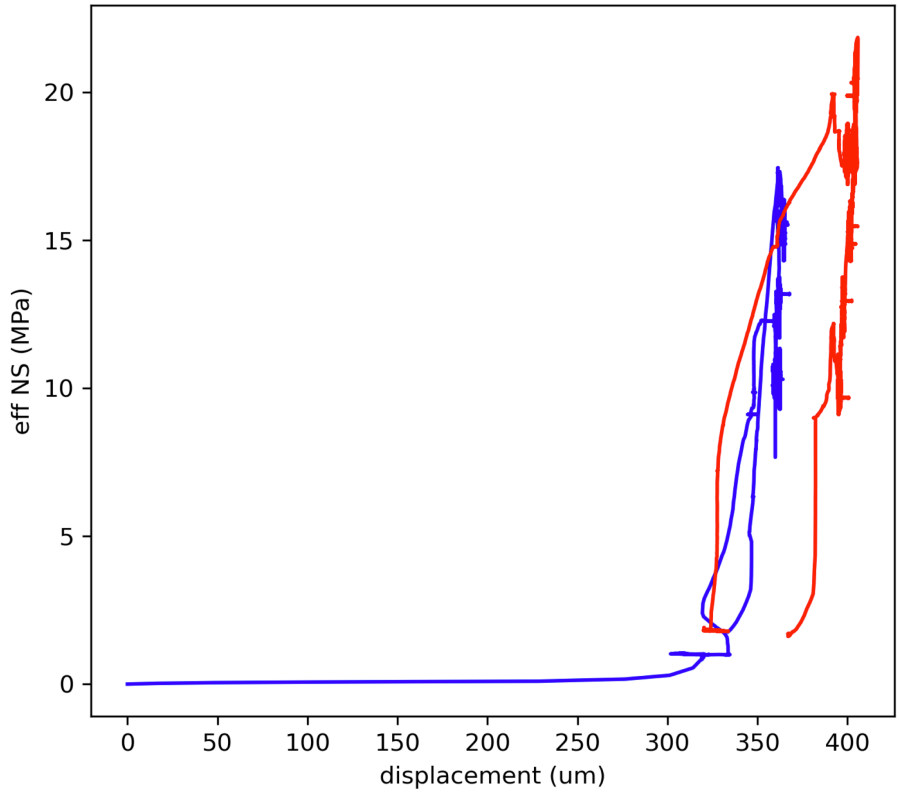



**Figure B.3.** Effective stress as a function of on-fault displacement for experiment p5483. The blue line shows the first load/unload part of the experiment which includes stress levels at 10, 12.5, and 15 MPa. After holding the specimen at ∼2 MPa over several hours, the experiment was resumed and the stress was increased to 17.5, 20 MPa and then step-wise decreased, shown with the red line.

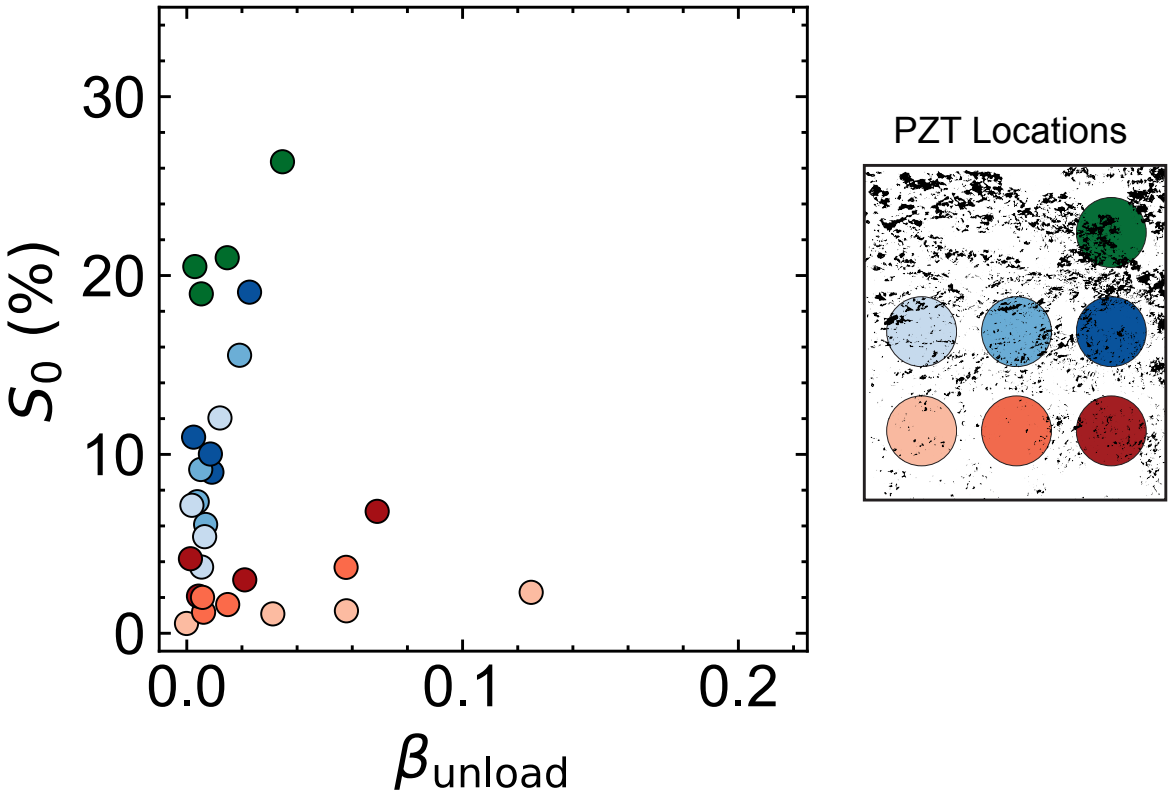



**Figure B.4.** Regions with larger contact area ($S_0$) exhibit smaller measure of nonlinearity during the unloading phase of the experiment, $\beta_{\text{unload}}$, and regions with small $S_0$ exhibit larger nonlinearity.

# Appendix C

## Supplementary Information for Chapter 5

### Introduction

This supporting information contains a figure that illustrates the relation between granular layer thickness and fracture roughness and their impact on the elastodynamic and permeability transients observed in our experiments.

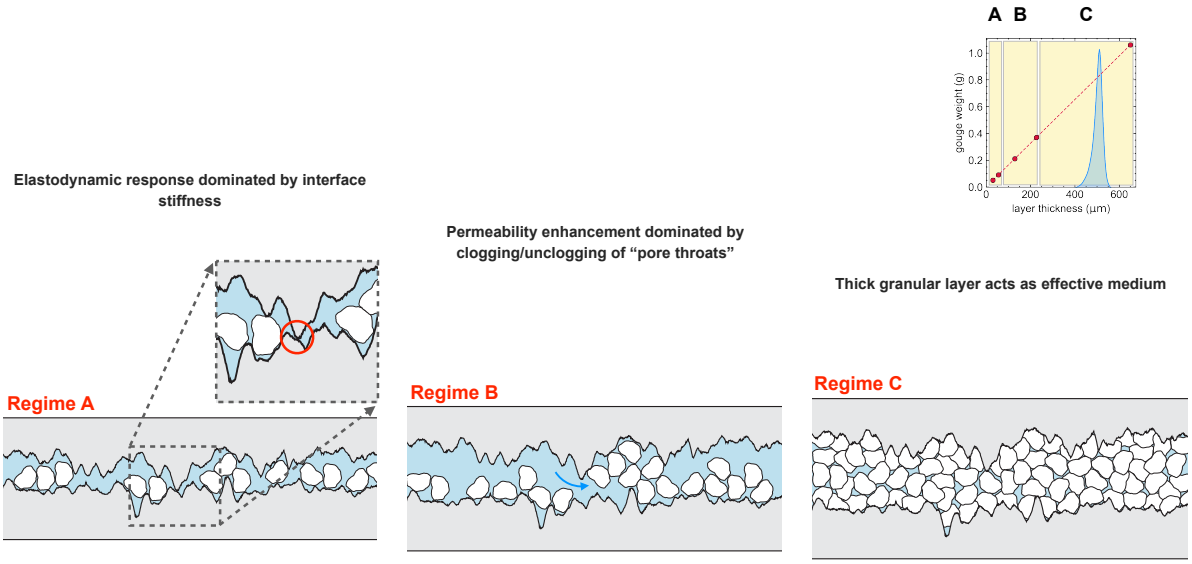



**Figure C.1.** Cartoon schematic illustrating the three proposed regimes. Regime A is characterized by small nonlinear elastic response and nearly zero permeability transients for bare fractures and fractures with gouge layers $\ll$ than fracture roughness. Regime B is dominated by the integrative effect of grains and fracture asperities, resulting in largest nonlinear elastic responses. Gouge layer is thin enough to allow granular clogging/mobilization through pore throats, producing large permeability transients. Regime C is dominated by granular layer and results in small elastodynamic and hydraulic transients. Upper right inset is a plot of fracture gap height distribution overlain with gouge layer thickness.